

Images/LogoUPC-eps-converted-to.pdf

PROGRAMA DE DOCTORAT EN ENGINYERIA BIOMÈDICA  
DEPARTAMENT D'ENGINYERIA DE SISTEMES,  
AUTOMÀTICA I INFORMÀTICA INDUSTRIAL  
CENTRE DE RECERCA EN ENGINYERIA BIOMÈDICA

**Tesis Doctoral por compendio de publicaciones**

**Muscular pattern based on multichannel surface emg  
during voluntary contractions of the upper-limb**

Mislav Jordanic

September 2017

Directores:

Miguel Angel Mañanas Villanueva

Mónica Rojas-Martínez



# Abstract

Magnetoencephalography (MEG) is a noninvasive brain signal acquisition technique that provides excellent temporal resolution and a whole-head coverage allowing the spatial mapping of sources. These characteristics make MEG an appropriate technique to localize the epileptogenic zone (EZ) in the preoperative evaluation of refractory epilepsy.

Presurgical evaluation with MEG can guide the placement of intracranial EEG (iEEG), the current gold standard in the clinical practice, and even supply sufficient information for a surgical intervention without invasive recordings, reducing invasiveness, discomfort, and cost of the presurgical epilepsy diagnosis. However, MEG signals have low signal-to-noise ratio compared with iEEG and can sometimes be affected by noise that masks or distorts the brain activity. This may prevent the detection of interictal epileptiform discharges (IEDs) and high-frequency oscillations (HFOs), two important biomarkers used in the preoperative evaluation of epilepsy.

In this thesis, the reduction of two kinds of interference is aimed to improve the signal-to-noise ratio of MEG signals: metallic artifacts mask the activity of IEDs; and the high-frequency noise, that masks HFO activity. Considering the large number of MEG channels and the long duration of the recordings, reducing noise and marking events manually is a time-consuming task. The algorithms presented in this thesis provide automatic solutions aimed at the reduction of interferences and the detection of HFOs.

Firstly, a novel automatic BSS-based algorithm to reduce metallic interference is presented and validated using simulated and real MEG signals. Three methods are tested: AMUSE, a second-order BSS technique; and INFOMAX and FastICA, based on high-order statistics. The automatic detection algorithm exploits the known characteristics of metallic-related interferences. Results indicate that AMUSE performs better when recovering brain activity and allows an effective removal of artifactual components.

Secondly, the influence of metallic artifact filtering using the developed algorithm is evaluated in the source localization of IEDs in patients with refractory focal epilepsy. A comparison between the resulting positions of equivalent current dipoles (ECDs) produced by IEDs is performed: without removing metallic interference, rejecting only channels with large metallic artifacts, and after BSS-based reduction. The results show that a significant reduction on dispersion is achieved using the BSS-based reduction procedure, yielding feasible locations of ECDs in contrast to the other approaches.

Finally, an algorithm for the automatic detection of epileptic ripples in MEG using beamformer-based virtual sensors is developed. The automatic detection of ripples is performed using a two-stage approach. In the first step, beamforming is applied to the whole head to determine a region of interest. In the second step, the automatic detection of ripples is performed using the time-frequency characteristics of these oscillations. The performance of the algorithm is evaluated using simultaneous intracranial EEG recordings as gold standard.

The novel approaches developed in this thesis allow an improved noninvasive detection and localization of interictal epileptic biomarkers, which can help in the delimitation of the epileptogenic zone and guide the placement of intracranial electrodes, or even to determine these areas without additional invasive recordings. As a consequence of this improved detection, and given that interictal biomarkers are much more frequent and easy to record than ictal episodes, the presurgical evaluation process can be more comfortable for the patient and in a more economic way.

# Resumen

La magnetoencefalografía (MEG) es una técnica no invasiva de adquisición de señales cerebrales que proporciona una excelente resolución temporal y una cobertura total de la cabeza, permitiendo el mapeo espacial de las fuentes cerebrales. Estas características hacen del MEG una técnica apropiada para localizar la zona epileptogénica (EZ) en la evaluación preoperatoria de la epilepsia refractaria.

La evaluación prequirúrgica con MEG puede orientar la colocación del EEG intracraneal (iEEG), el actual modelo de referencia en la práctica clínica, e incluso suministrar información suficiente para una intervención quirúrgica sin registros invasivos; reduciendo la invasividad, la incomodidad y el costo del diagnóstico de la epilepsia prequirúrgica. Sin embargo, las señales MEG tienen baja relación señal ruido en comparación con el iEEG pudiendo imposibilitar la detección de descargas epileptiformes interictales (IEDs) y oscilaciones de alta frecuencia (HFOs), dos importantes biomarcadores utilizados en la evaluación preoperatoria de la epilepsia.

En esta tesis, la reducción de dos tipos de interferencia está dirigida a mejorar la relación señal-ruido de la señal MEG: los artefactos metálicos que enmascaran la actividad de las IEDs; y el ruido de alta frecuencia, que enmascara la actividad de las HFOs. Debido al gran número de canales MEG y la larga duración de los registros, tanto reducir el ruido como seleccionar los biomarcadores manualmente es una tarea que consume mucho tiempo. Los algoritmos presentados en esta tesis aportan soluciones automáticas dirigidas a la reducción de interferencias y la detección de HFOs.

En primer lugar, se presenta y valida un nuevo algoritmo automático basado en BSS para reducir interferencias metálicas mediante señales simuladas y reales. Se prueban tres métodos: AMUSE, una técnica BSS de segundo orden; y INFOMAX y FastICA, basados en estadísticos de orden superior. El algoritmo de detección automático utiliza las características conocidas de la señal producida por la interferencia metálica. Los resultados indican que AMUSE recupera mejor la actividad cerebral y permite una eliminación efectiva de componentes artefactuales.

Posteriormente, se evalúa la influencia del filtrado de artefactos metálicos en la localización de IEDs en pacientes con epilepsia focal refractaria. Se realiza una comparación entre las posiciones resultantes de dipolos de corriente equivalentes (ECDs) producidos por IEDs: sin eliminar interferencias metálicas, rechazando solamente canales con elevados artefactos metálicos y, por último, después de una reducción utilizando el algoritmo BSS desarrollado. Los resultados

muestran que se logra una reducción significativa en la dispersión utilizando el procedimiento de reducción basado en BSS, lo que produce ubicaciones factibles de los dipolos en contraste con los otros enfoques.

En segundo lugar, se desarrolla un algoritmo para la detección automática ripples epilépticos en MEG utilizando sensores virtuales basados en la técnica de beamformer. La detección de ripples se realiza mediante un enfoque en dos etapas. Primero, se determina el área de interés usando beamformer. Posteriormente, se realiza la detección automática de ripples utilizando las características en tiempo-frecuencia. El rendimiento del algoritmo se evalúa utilizando registros iEEG simultáneos.

Los nuevos enfoques desarrollados en esta tesis permiten una detección no invasiva mejor de los biomarcadores interictales, que pueden ayudar a delimitar la zona epileptogénica y guiar la colocación de electrodos intracraneales, o incluso determinar estas áreas sin este tipo de registros. Como consecuencia de esta mejora en la detección, y dado que los biomarcadores interictales son mucho más frecuentes y fáciles de registrar que los episodios ictales, la evaluación prequirúrgica puede ser más cómoda y menos costosa para el paciente.

# Contents

<b>Abstract</b>	<b>i</b>
<b>Resumen</b>	<b>iii</b>
<b>List of Tables</b>	<b>xi</b>
<b>List of Figures</b>	<b>xiii</b>
<b>1 Introduction</b>	<b>1</b>
1.1 Fundamentals and neurophysiology of the brain . . . . .	1
1.1.1 Brain anatomy and functions . . . . .	2
1.1.2 The neuronal activity . . . . .	3
1.2 Acquisition systems . . . . .	8
1.2.1 Bioelectric and biomagnetic signals . . . . .	8
1.2.2 Electroencephalography . . . . .	9
1.2.3 Magnetoencephalography . . . . .	11
1.2.4 Comparison between MEG and other noninvasive neuroimaging methods	13
1.2.5 Invasive EEG and MEG . . . . .	16

1.3	Source localization of epileptic focus in pharmacoresistant epilepsies . . . . .	17
1.3.1	Epilepsy . . . . .	18
1.3.2	The presurgical evaluation of epilepsy . . . . .	19
1.3.3	Interictal biomarkers for localization of the epileptic focus . . . . .	21
	Interictal epileptiform discharges . . . . .	21
	High-frequency oscillations . . . . .	23
1.3.4	Methods for noninvasive localization of the epileptic focus in MEG . . . .	25
	Equivalent current dipole . . . . .	26
	Beamforming . . . . .	28
1.4	Artifacts and rejection techniques in MEG . . . . .	30
1.4.1	Physiological artifacts . . . . .	31
1.4.2	Non-physiological artifacts . . . . .	32
1.4.3	Rejection techniques . . . . .	33
	Blind source separation methods . . . . .	33
	Signal space separation methods . . . . .	34
	Beamformer spatial filtering . . . . .	35
<b>2</b>	<b>Problem statement</b>	<b>37</b>
2.1	Introduction . . . . .	37
2.2	Noninvasive detection of focal epileptic activity in MEG . . . . .	38
2.3	Objectives . . . . .	39
2.4	Thesis framework . . . . .	40



<b>3</b>	<b>Automatic BSS-based filtering of metallic interference in MEG recordings</b>	<b>41</b>
3.1	Introduction . . . . .	42
3.2	Materials and Methods . . . . .	45
3.2.1	Simulated data . . . . .	45
3.2.2	Blind source separation approaches to artifact reduction . . . . .	48
3.2.3	Performance assessment . . . . .	51
3.3	Results . . . . .	52
3.3.1	Simulated data . . . . .	52
3.3.2	Blind source separation and automatic detection . . . . .	52
3.3.3	Performance assessment . . . . .	54
3.3.4	Real data . . . . .	57
3.4	Discussion . . . . .	57
3.5	Acknowledgments . . . . .	62
<b>4</b>	<b>Influence of metallic artifacts during interictal epileptiform activity</b>	<b>63</b>
4.1	Introduction . . . . .	64
4.2	Materials and methods . . . . .	67
4.2.1	Patients, acquisition settings and previous preprocessing . . . . .	67
4.2.2	Volume conduction model . . . . .	68
4.2.3	IED identification . . . . .	68
4.2.4	Artifact removal . . . . .	69
4.2.5	Estimation of the ECD . . . . .	71
4.2.6	Evaluation of estimated sources . . . . .	72

4.3	Results . . . . .	73
4.3.1	Artifact removal . . . . .	73
4.3.2	ECD estimation . . . . .	74
4.3.3	Influence of the ASR on dipole localization. . . . .	77
4.4	Discussion . . . . .	78
4.5	Acknowledgments . . . . .	83
<b>5</b>	<b>Automated detection of Epileptic ripples</b>	<b>84</b>
5.1	Introduction . . . . .	85
5.2	Materials and Methods . . . . .	87
5.2.1	Patients, signal acquisition settings and previous preprocessing. . . . .	87
5.2.2	Volume conduction model . . . . .	89
5.2.3	MEG automatic detection of ripples . . . . .	89
5.2.4	Threshold selection: Precision/recall curves. . . . .	94
5.2.5	Detection and localization of ripples inside and outside the ROI . . . . .	95
5.3	Results . . . . .	96
5.3.1	Detection of the region of interest . . . . .	96
5.3.2	Threshold selection inside the ROI . . . . .	96
5.3.3	Automatic detection . . . . .	97
5.3.4	Detection and Localization of ripples inside and outside the ROI . . . . .	99
5.4	Discussion . . . . .	100
5.4.1	Main contribution of the study . . . . .	100
5.4.2	Threshold selection and performance analysis . . . . .	103

5.4.3	Evaluation of ripples inside and outside the ROI . . . . .	105
5.4.4	Limitations of the study and further work . . . . .	106
5.5	Conclusion . . . . .	108
5.6	Acknowledgments . . . . .	108
<b>6</b>	<b>Conclusion</b>	<b>109</b>
6.1	Summary . . . . .	109
6.2	Main conclusions . . . . .	111
6.3	Main contributions . . . . .	114
6.4	Future Work . . . . .	115
	<b>Bibliography</b>	<b>118</b>



# List of Tables

3.1	Error percentage for nMSE, delta power and alpha power (average of all channels) for non-corrected signals, AMUSE-corrected signals and INFOMAX-corrected signals. . . . .	56
4.1	Summary of all patients. Age, type of epilepsy, type of metallic artifacts. . . . .	68
4.2	Results for all patients . . . . .	74
5.1	Clinical information of the Patients . . . . .	88
5.2	Brodmann Areas and lobes of the ROI and detection of ripples in MEG-VS compared to iEEG (R: right, L: left) . . . . .	98
5.3	Optimum SD and Energy for each LOO iteration . . . . .	98
5.4	Number of ripples, mean number of MEG-VS in each ripple for all the subjects and percentage of detected ripples inside the most active region. The evaluation outside the ROI was performed placing a grid of the same size and number of channels in the contralateral hemisphere where the ROI was placed. . . . .	99
5.5	Average values of performance (Precision, Recall and F1 score) and number of Co-detected Events, Detected Events only in iEEG, and detected events only in MEG when iEEG SD threshold was lowered. The duration of the EOI was set to $0.5 \cdot (mean + 3 \cdot SD)$ for the three evaluated thresholds . . . . .	104



# List of Figures

1.1	a) Diagrammatic representation of the major parts of the brain. b) Main structures of the limbic system. Image adapted from Bear et al. (2016) . . . . .	2
1.2	Morphology of the neuron. Image from Carpenter and Reddi (2012) . . . . .	4
1.3	Communication at a chemical synapse. Image from Reece et al. (2013) . . . . .	5
1.4	Generation of an action potential. Image from Reece et al. (2013) . . . . .	6
1.5	Generation of electrical and magnetic fields by synaptic currents in pyramidal cells. Image adapted from Bear et al. (2016) . . . . .	7
1.6	The international 10-20 system seen from (A) left and (B) above the head. A = Ear lobe, C = central, Pg = nasopharyngeal, P = parietal, F = frontal, Fp = frontal polar, O = occipital. Image adapted from Ame (1991) . . . . .	11
1.7	Block diagram of a typical MEG system. Adapted from Sternickel and Braginski (2006) . . . . .	13
1.8	(Left) MEG setup measuring the tangential components of neuroelectrical activity, using an axial gradiometer. (Right) MEG setup measuring the tangential components of neuroelectric activity, using a planar gradiometer. Image from (Wendel et al., 2009) . . . . .	14
1.9	Spatial response patterns from fMRI and MEG/EEG in focally-stimulated visual cortex. Image from Sharon et al. (2007) . . . . .	15

1.10	Schematic representation of the overlapping cortical zones in epilepsy. Different cortical zones are estimated during the pre-surgical evaluation of a patient with epilepsy. These zones can often overlap, providing the epileptologist with concordant findings for the delineation of the epileptogenic zone (EZ). The high-frequency oscillation (HFO) zone is another potentially epileptogenic area that has been recently added to this picture as a further piece of information to circumscribe the EZ. Image from (Tamilia et al., 2017) . . . . .	20
1.11	Interictal epileptic discharge (IED) patterns recorded in human partial epilepsies with intracranial electrodes. <i>a</i> Interictal spike; <i>b</i> group of interictal spikes, <i>c</i> sharp wave; <i>d</i> fast activity (brushes); <i>e</i> paroxysmal slow activity superimposed to slow spikes. Image from (de Curtis et al., 2012) . . . . .	22
1.12	HFO classification. (A) HFO visible in spike; (B) HFO not visible in spike; (C) HFO visible, independently of a spike. Top: non-filtered spike; middle: signal filtered with high-pass filter of 80Hz; bottom: signal filtered with high-pass filter of 250Hz. Image adapted from (Urrestarazu et al., 2007) . . . . .	24
1.13	Example of computation of a head model with a) a single sphere, b) with overlapping spheres (one sphere is computed for each channel) and c) BEM method. Head shapes and images generated with Brainstorm (Tadel et al., 2011) . . . . .	26
1.14	Visualization of a dipolar distribution in a) Most relevant scalp signals, b) Topographic disc c) Whole-sensor 2D image d), e) and f) 3D helmet activation map. Images generated with Brainstorm (Tadel et al., 2011) . . . . .	27
1.15	Schematic representation of beamforming analysis. The neuronal signal at a location of interest is estimated as the weighted sum of the MEG channels ( $m_1...m_n$ ) resulting into a Virtual Sensor (VS). . . . .	29



- 1.16 General scheme of the idea behind spatial filtering. The ideal spatial filtering is only sensitive to the source of interest and non-sensitive to other interference sources. In reality, it exists some spatial leakage. A general filter, such as dipole fitting procedure, do not actively suppress the interfering source. The LCMV-Beamforming is an optimized spatial filter that is not only sensitive to the source of interest but is also actively suppressing the interfering sources. . . . . 36
- 3.1 Scheme for generation of a simulated artifactual MEG recording: (a) five-second epoch of raw MEG with metallic artifacts (only 16 selected channels are drawn). Orange traces correspond to the highly artifactual channels selected by the experts; (b) low-pass filtered artifactual channels (cutoff frequency automatically calculated from reverse-cumulative spectra); (c) selected morphologies (orange traces) after correlation among channels in (b), and their corresponding linear regression coefficients (whole head maps); (d) propagation of artifacts corresponding to coefficients obtained in (c); (e) five-second epochs of raw artifact-free MEG channels; and (f) simulated signals obtained by summation of (d) and (e). . . . . 47
- 3.2 Automatic artifact-related component selection: (a) frequency and entropy estimation (for all extracted ICs) and thresholds (blue dashed lines). (b) Artifactual area selected by the union of the regions of interest of the selected ICs. (c) As an example, evaluation of the projection of ICs 3 and 4 is shown. Regions of interest are indicated with dark blue shading. IC 3 is outside the artifactual area and therefore would not be selected by the automatic algorithm, whereas IC 4 would, as its region of interest is inside the artifactual area and the weak criteria concerning frequency and entropy are met. . . . . 50
- 3.3 Sum of the linear regression coefficients normalized with respect to its maximum for all of the selected artifactual patterns for the 10 simulated MEG sets. Coefficients were obtained for the whole head after morphology selection and linear regression of each channel with the selected morphologies. Note that metallic artifacts behave differently depending on their nature and therefore they can appear in different areas of the head for each simulated MEG set. . . . . 53

3.4	MEG channels (16 distributed evenly on the scalp) for: (a) control subject, that is, clean recording, free of metallic artifacts; (b) simulated subject. Orange traces indicate channels originally selected as artifacts by the experts. . . . .	54
3.5	Artifact-reduction for a simulated subject: (a), (b) and (c) show the first 20 extracted ICs corresponding to AMUSE, INFOMAX and FastICA algorithms, respectively. Note that the first 2 ICs (orange traces) obtained by AMUSE and INFOMAX were automatically selected and removed to perform signal reconstruction, whose results are shown in (d) and (e), respectively. FastICA was not able to extract useful artifact-related components and the reconstruction shown in (f) does not remove any amount of artifact (and, consequently, the reconstructed signals equal those of figure 3.4(b)). . . . .	55
3.6	Error percentage for normalized MSE, delta power and alpha power, shown for three different simulated subjects as examples. Errors are shown for non-corrected, AMUSE-corrected and INFOMAX-corrected signals. Due to the frequency content of metallic artifacts, errors are expected to be lower in the alpha band and higher in the delta band, focusing especially on the areas where the artifact is located. Note that AMUSE-based reconstruction shows the lowest errors for the three measures. . . . .	56
3.7	(a) Five-second epoch of raw MEG signals containing prominent metallic interference. Posterior channels are shown as an example. (b) Corrected MEG signals obtained after applying automatic AMUSE-based metallic removal procedure. . .	58
3.8	(a) Topographic distribution of the average alpha power of the 10 artifactual subjects. (b) Average of alpha power obtained after applying automatic AMUSE-based metallic removal procedure. . . . .	59
4.1	(a) Example of IED identification for subject 1 by in EEG simultaneous data. Green line denotes the spike onset and orange line the spike peaks. (b) Topographical map at spike onset where a dipolar distribution between T4 and P4 is observed. . . . .	70

4.2	5 s epoch corresponding to 37 MEG channels for subject 1 selected for dipole fitting. Vertical lines show the onset of at the same well-defined IED shown in figure 4.1. (a) RAW signal before applying automatic reduction procedure. Red channels were selected by experts as highly artifacted channels and removed in the channel rejection procedure. (b) Corrected MEG signals obtained after applying automatic AMUSE-based metallic removal procedure. . . . .	75
4.3	Topographic distribution of normalized energy corresponding to the removed metallic activity for the 14 subjects. Artifact distribution of energy mainly depended on the type of metallic interference, to its position and size. . . . .	76
4.4	Magnetic isofields computed for the 37 selected channels corresponding to the same IED onset shown in figure 4.1. For the three approaches: (a) before applying any filtering procedure (no correction), (b) after channel rejection, (red channels were removed, green channels were included); and (c) after applying the metallic reduction procedure. The central channel is shown in blue. . . . .	77
4.5	Dipoles obtained for the ten IEDs of Patient 1 (a) <i>XY</i> plane, (b) <i>XZ</i> plane and (c) <i>YZ</i> plane. Blue, green and red dipoles belong to no-correction, channel rejection and automatic filter procedures. Dipole 4, located outside the brain in the no-correction procedure, was discarded for the subsequent measurements of dispersion and distance. . . . .	78
4.6	Positions obtained for the consecutive fitted dipoles during the rising phase of an IED. (a) <i>XY</i> plane, (b) <i>XZ</i> plane and (c) <i>YZ</i> plane. Blue, green and red dipoles belong to no-correction, channel rejection and automatic filter procedures. The dipole measured at the onset of the IED is displayed as 'o'. . . . .	79
4.7	Dispersion values versus ASR for the 14 subjects. Linear regression showed a value of $r = 0.80$ ( $p\text{-value} = 0.0005$ ). . . . .	79

4.8	(a) Difference between central source position before and after applying automatic filtering procedure versus ASR. Regression line showed a value of $r = 0.75$ ( $p\text{-value} = 0.002$ ). (b) Difference between dispersions versus ASR. Regression line showed a value of $r = 0.89$ ( $p\text{-value} < 0.001$ ). . . . .	80
5.1	Scheme of the two stages HFO detection algorithm. . . . .	89
5.2	Schematic example of the overlapping conditions. If two events had common samples and if the length of the common samples, LOV, was higher to the half of the length of the first event L1 and the second event L2, then the both events were considered as overlapping events. . . . .	92
5.3	Example of a ripple with a clear and distinguishable peak in high frequency and the selection of HiFP, Trough, LoFP in the PSD estimation at the maximum point of the envelope. . . . .	93
5.4	Example of localization of the middle virtual sensor (in red) in the warped anatomy and the posterior MNI transformation. . . . .	97
5.5	Averaged performance curves. a) Precision-Recall curves for all the tested factorSD thresholds. Each value correspond to a pair of $factor_{SD}$ and $thres_{Er}$ . b) F1score – Energy for all the tested thresholds. c) and d) show the recall and precision curves with respect to the energy threshold. The optimum $factor_{SD}$ and $thres_{Er}$ values were 2.25 and 17.75% respectively. . . . .	100
5.6	Simultaneous detection of TP, FP and FN in MEG, iEEG and MEG-VS signals. MEG VS channels shown are placed on a tridimensional star-shaped configuration. MEG channels shown belong to the nearest closest scalp area where the ROI was found. Green events correspond to a detected HFO in iEEG and MEG-VS (TP). Red events correspond to a detected HFO in MEG-VS but not visible in iEEG (FP). Pink events correspond to a detected HFO in iEEG but not visible in MEG-VS (FN). Non-labeled visible events did not meet the first conditions (EOI detection). . . . .	101

5.7	Localization maps for the number of detected ripples a) inside the ROI and b) outside the ROI, on the contralateral hemisphere for Patient 1. . . . .	102
5.8	Localization maps in slices of the number of detected ripples for all subjects for a) inside the ROI and b) outside the ROI. The colormap measures the number of times that a VS appeared in a ripple. . . . .	103



# Chapter 1

## Introduction

### 1.1 Fundamentals and neurophysiology of the brain

The central nervous system (CNS) is responsible for processing information received from all parts of the body. The two main organs of the CNS are the brain and the spinal cord and are entirely composed of two kinds of specialized cells: neurons and glia. The brain is the most complex part of the human body and exerts a centralized control over the other organs. Neurons, the basic working units of the brain, are designed to transmit information within the brain to other nerve cells and to communicate with muscles and gland cells. The complex architecture of the brain is built on the extensive number of interconnected neurons sharing information through specialized connections called synapses. This connection allows neurons to communicate through an electrical or chemical signals, producing ionic currents that generate electric and magnetic fields.

The CNS is organized in multiple levels, from simple connections between cells to coordinated cell populations, building a complex architecture of interconnected brain regions. The neural processes at this last level are produced by the dynamic coordination of smaller elements. In the cerebral cortex, all this brain activity is summated and its electric and magnetic fields can be measured on the scalp surface.

### 1.1.1 Brain anatomy and functions

From an anatomical point of view, the brain can be divided into three parts: the cerebrum, cerebellum and brainstem (Figure 1.1 a). The cerebrum is the most developed part of the human brain and is divided into the left and right hemispheres. The cerebral cortex consists of the outer layers of the cerebrum and is commonly divided into three parts: the archicortex and the paleocortex, which are the cortical parts of the limbic system; and the outermost layer called neocortex, which is part of the mammalian brain and is involved in higher-order functions. Most of the actual information processing in the brain takes place in the cerebral cortex. In humans, as in mammalian and primates, this structure is folded and results into a much greater surface area in the confined volume of the skull. Folds or ridges in the cortex are referred as gyri, and grooves or fissures are called sulci. The main sulci define four lobes in each hemisphere: the frontal, temporal, parietal and occipital lobes.

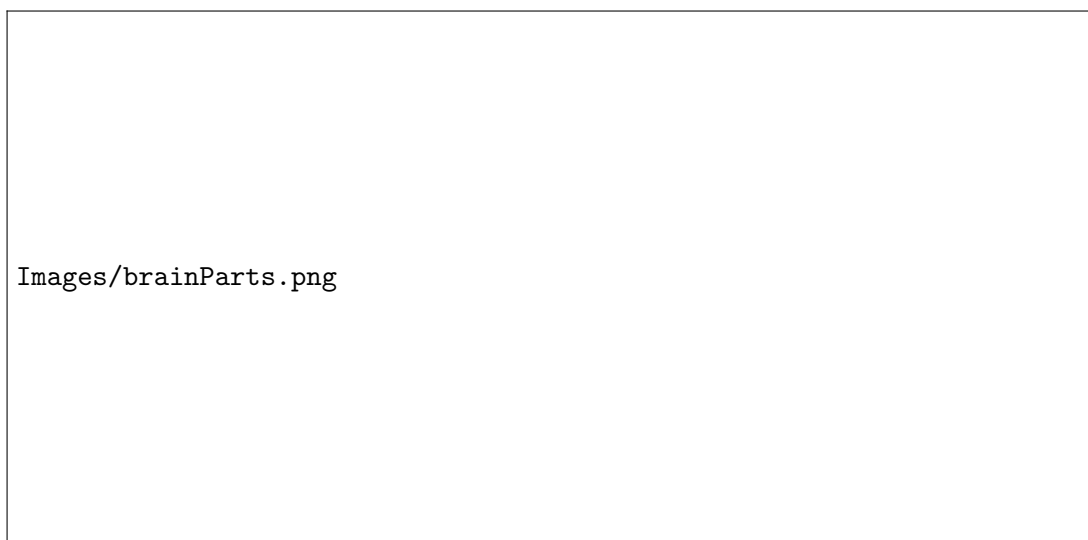


Figure 1.1: a) Diagrammatic representation of the major parts of the brain. b) Main structures of the limbic system. Image adapted from Bear et al. (2016)

The largest brain lobes, the frontal lobes, are located at the front of each cerebral hemisphere. They are involved in several functions of the body: motor functions, planning, reasoning, impulse control, memory, and language. Behind these, the parietal lobe are located. Their main functions are the processing of sensory information, understanding spatial orientation and body awareness. The temporal lobes play an important role in organizing sensory input, auditory perception, language and speech production, facial recognition, and memory association and



formation. The occipital lobes are located at the posterior region of the cerebral cortex. Their main function include visual perception, color recognition, reading comprehension, depth perception and recognition of object movement.

Below the cortex and on top of the brainstem, a set of structures known as the limbic system (Figure 1.1 b) are found. These are one of the most primitive parts of the human brain and are involved in the emotions and motivations related to survival. The hippocampus consists of two "horns" that are associated to various processes of cognition related to spatial memory and learning. At its lower end, the amygdalas are located. These are two almond-shaped structures that work as an integrative center for emotions, emotional behavior, and motivation. The thalamus has the important role of relaying sensory input to the cerebral cortex, and also regulates consciousness, and alertness. The hypothalamus, located below the thalamus, is involved in homeostasis processes, controls body temperature, hunger, fatigue, sleep, and circadian rhythms (Purves and Williams, 2001).

The concept of limbic system has survived to modern times. However, the idea of a unified limbic system is outdated, and the structures and processes related to memory and emotions are more complex, involving also non-limbic areas of the brain (Rolls, 2015). In addition, functions associated with cognition and reasoning require the action of the hippocampus, highly linked to memory processes.

### **1.1.2 The neuronal activity**

Neurons are the basic units of information processing of the nervous system. The brain contains between 50 and 100 billion ( $10^{11}$ ) of neurons (Andreassi, 2007), specialized cells whose main function is to receive stimuli and send responses through impulses. Although there are various type of neurons, all of them contain four distinct regions: the cell body or soma, the dendrites, the axon and the axon terminals (Figure 1.2).

The nucleus is found inside of the soma and is responsible for the synthesis of most of the neuronal proteins and membranes. Axons are specialized in the conduction of action potentials, a particular type of electric impulses, outward from the soma towards the axon terminals. These are small branches of the axon that form the synapses, which are the connections with other

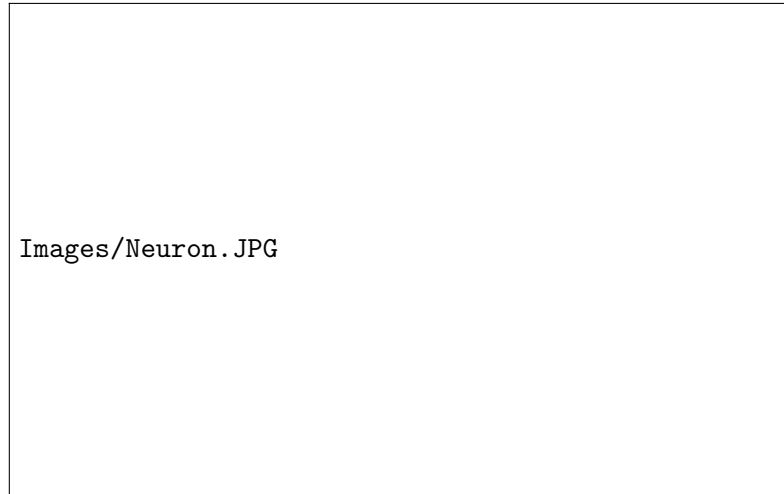
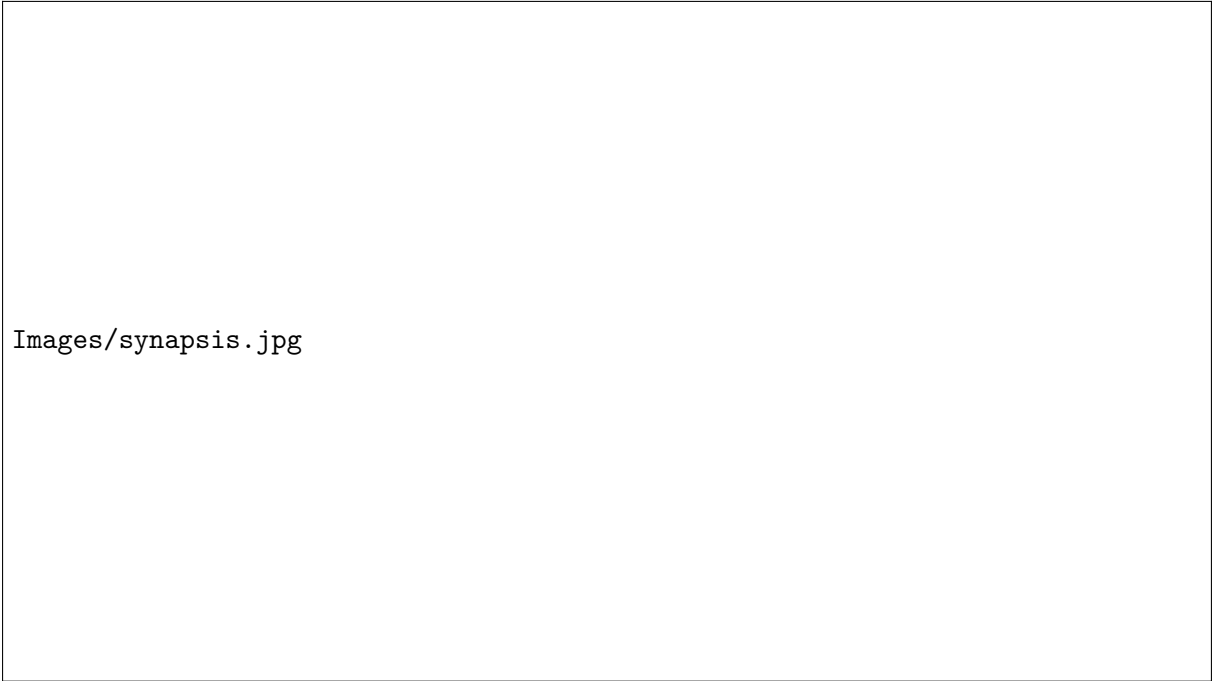


Figure 1.2: Morphology of the neuron. Image from Carpenter and Reddi (2012)

neurons, glial cells or muscle fibers. Dendrites are responsible of receiving chemical signals from the axon terminals of other neurons, converting these into electric impulses and transmitting them to the soma. The neurons of the brain have extremely long dendrites with complex branches allowing them to form synapses from a large number of neurons, up to a thousand (Lodish et al., 2000).

To achieve a long-distance and rapid communication, neurons have special abilities for sending electrical signals along axons. Generally, the information is transmitted in one direction: a presynaptic cell (or sending cell) sends a signal that is picked by the postsynaptic cell (or receiving cell), which can be a dendrite of another neuron, a muscle or a gland cell. The axon terminal of the presynaptic cell contain vesicles filled with neurotransmitters. When a synapsis occurs, these are released to a space called synaptic cleft and they bind with specific receptors located at the plasma membrane of the postynaptic cell (Figure 1.3)

In its resting state, neurons have a negative concentration gradient. This state is called resting membrane potential and is produced by a difference between the number of positive ions outside and inside the neuron. During the resting membrane potential, there are more sodium ions ( $Na^+$ ) outside than inside the neuron and more potassium ions ( $K^+$ ) inside than outside. The number of positive charges outside the neuron is higher than inside, resulting in a negative charge with respect to the exterior of the cell with a typical value of around -70mV. The ions try to balance their concentrations through the flow of ions in and out the cell, but the cell maintains



Images/synapsis.jpg

Figure 1.3: Communication at a chemical synapse. Image from Reece et al. (2013)

this potential stable through the sodium-potassium pump, forcing potassium back into the cell and pushing sodium out of the cell at the same time.

The neurons feature different kinds of sodium and potassium channels: the voltage-gated channels that open and close when the membrane potential changes, the ligand-gated channels that open when a neurotransmitter latches onto its receptor, and mechanically-gated channels that open in response to the physical stretching of the membrane. When stimulus occur or neurotransmitters arrive at the neuron dendrites, the mechanically-gated or ligand-gated sodium channels open and sodium starts diffusing inside the cell, producing a positive increment on the membrane potential. If this potential exceeds the threshold potential, around  $-55$  mV, the large number of voltage-gated sodium channels open rapidly increasing the number of sodium ions inside and depolarizing the cell, triggering the start of the action potential. When the membrane potential reaches around  $+40$  mV, the sodium channels close and the potassium voltage-gated channels open, allowing the diffusion of this substance outside the cell and repolarizing the neuron. In this stage, the diffusion of potassium produces a higher negative membrane potential than in the resting state. This effect is known as hyperpolarization or undershoot, where the membrane potential reaches  $-75$  mV. At this point, potassium gates close and the sodium-potassium pump restores the membrane into the resting potential. Before a new action potential

can produced, a refractory period caused by the inactivation of the sodium channels preventing the cell to fire during a period of time. Figure 1.4 describe the different phases of the generation of an action potential in a neuron.



Figure 1.4: Generation of an action potential. Image from Reece et al. (2013)

An action potential only occurs in a limited area of the cell membrane, but the changes in membrane potentials are enough to initiate another action potential in a neighboring space, giving rise to another action potential further down the axon. The refractory period ensures that the information travels only in one direction. When the electric impulse arrive to the axon terminal, neurotransmitters are released, starting the process again in a new neuron.

Synaptic activity is often the most important source of extracellular current flow (Buzsáki et al., 2012) but currents in the brain can also emerge from other non-synaptic sources that do play significant roles in the nervous system (Jefferys, 1995). Neuronal activity in the brain gives rise to transmembrane currents that can be measured in the extracellular medium. All neuron

types contribute to these currents, but their contribution depends on the shape of the cell (Jefferys, 1995). Pyramidal neurons are the most populous kind of excitatory neurons (2/3 of the mammalian brain). Most of them are radially oriented in the cortex and orthogonal to the brain surface. Its long dendrites can generate strong dipoles along its axis (see figure 1.5).



Figure 1.5: Generation of electrical and magnetic fields by synaptic currents in pyramidal cells. Image adapted from Bear et al. (2016)

The orientation of this type of cells give rise to an open field, as the dendrites face one direction and the soma another and there is considerable spatial separation between them (Buzsáki et al., 2012). When a group of cells is excited simultaneously, the tiny synchronized signals sum up to generate one larger signal that can be measured on the surface of the head (Bear et al., 2016). The different modalities for measuring the neural activity will be discussed in section 1.2. By contrast, spherically symmetric neurons that whose equal-sized dendrites emerge in all directions, may generate a closed electrical field when several dendrites are simultaneously activated and their potential cancel between each other. In practice, this is rarely the case and the depolarization of a single dendrite generates a small dipole. For this reason, some deep structures can generate dipoles that contribute to the global signal measurable at the extracellular medium (Attal et al., 2007).

## 1.2 Acquisition systems

The summation of the spontaneous brain activity can be measured using different techniques that can be classified into invasive or noninvasive procedures. Noninvasive techniques measure the activity from the scalp. Electroencephalography (EEG) measures the electrical activity using electrodes in contact with the skin and magnetoencephalography (MEG) measures the magnetic activity using gradiometers and magnetometers. Invasive techniques, on the other hand, can measure the activity directly from the cerebral cortex (electrocorticography) or even in deep structures (intracranial electroencephalography). Several biomedical signal processing methods have been used to evaluate and diagnose brain disorders in the time and frequency domains (Sörnmo et al., 2005) using the information provided by invasive and noninvasive techniques. Due to their small signal-to-noise ratio, specially in noninvasive recordings, the preprocessing of the signals in order to remove artifacts and interferences is essential. This section describes, firstly, the fundamentals of MEG and EEG; and secondly, the differences between the different acquisition modalities.

### 1.2.1 Bioelectric and biomagnetic signals

As explained before, a group of synchronized neurons can generate an electrical and magnetic field that, depending on the number of involved neurons and the distance between them and the sensors, can provide information about the mechanisms of the brain function.

Brain spontaneous signals are commonly subdivided into different frequency bands, with different properties and functional significance (Huang, 2016). These bands are delta (1 to 4 Hz), theta (4 to 8 Hz), alpha (8 to 12 Hz), beta (12 to 30 Hz) and gamma (greater than 30 Hz). Apart from the normal resting-state brain rhythms, these techniques can also record other type of time-locked physiological and pathological activity. Event-related potentials (ERPs) are significant voltage fluctuations resulting from evoked neural activity initiated by an external or internal stimulus (Coles and Rugg, 1996). They are commonly used to analyze sensory and cognitive tasks.

Moreover, some neurological pathologies present electrical characteristics that are observable

in the signals. Epileptic seizures present themselves as brief episodes of abnormal synchronous neural activity of the brain (Fisher et al., 2005) that can be recorded using EEG and MEG techniques. The epileptic brain also shows other type of time-locked activity during the non-seizure state, called interictal state (Smith, 2005). These types of fluctuations are also useful to diagnose, classify and characterize epileptic disorders. Other neurological diseases such as dementias, psychiatric disorders, neurological infections, or encephalopathies also present characteristic features in the measurable brain signals (Smith, 2005).

Traditionally, the spectral study of brain signals has been limited to the standard frequency bands (typically up to 50 Hz). However, during the last decades, higher frequency bands of activity have been studied in the normal mammal brain (Buzsaki et al., 1992) and also in the pathological brain (Fisher et al., 1992). This was possible due to the technological improvement of the acquisition systems and the computers used for analysis. Among the higher frequency activity, the oscillations commonly known as high frequency oscillations (HFOs) have become an important field of study in epilepsy. HFOs are subdivided into two bands: the ripple band (80 to 200 Hz) and the fast ripple band (200 to 500 Hz) (Gotman, 2010), and are considered a promising biomarker of epilepsy, useful to localize the epileptic focus (Jacobs et al., 2012).

### 1.2.2 Electroencephalography

EEG signals (usually called simply EEG) were recorded on the human scalp for the first time in 1924 in by Hans Berger (Sörnmo et al., 2005). The EEG evolved during the second part of the 20<sup>th</sup> century and became a tool used to study several neurological diseases. However, with the appearance of computed tomography (CT) and magnetic resonance imaging (MRI), the technique lost strength in the neurologists' community, mainly because its poor spatial resolution (Zifkin and Avanzini, 2009). The technological advances of the last decades allowed to record and save larger amounts of EEG data, enhancing the spatial resolution of the technique by adding more electrodes and increasing the signal-to-noise ratio of the signals. Moreover, the improvement of the processing capabilities of computers fastened the development of new signal analysis techniques useful to evaluate and diagnose the normal and pathological brain.

To measure electrical signals outside the head, neural activity must travel from the brain through

the meninges, the skull, and the scalp layers before reaching the electrodes. All these layers are electrically insulating layers with poor conductivity and equivalent to capacitors. In order to improve the conductivity between the scalp and electrodes, conductive gel is commonly used. Even after proper enhancement of the skin-electrode contact, the potentials are very small and must be boosted. For this reason, other important part of the EEG systems, and in general any biomedical signal acquisition system, is the amplifier. Its main function is to maximize the signal-to-noise ratio on the measured voltage and to increase the signal above the noise level that may be introduced in the latter elements (Jackson and Bolger, 2014).

As any electric other signal, the voltage is measured by the electrodes with respect to a reference point. The most common electrode montages include the bipolar, where the potential difference between a pair of electrodes is measured, and the unipolar, where the potential of an electrode is compared to a neutral electrode or to the average of all electrodes.

The EEG is commonly recorded using the international 10/20 system (Klem et al., 1999). This montage employs 21 electrodes attached to the surface of the scalp. The positions are determined using two reference points: *nasion*, which is the delve at the top of the nose; and *inion*, which is the bony lump in the mid-line at the back of the head (see Figure 1.6). From these points, the skull perimeters are measured in the transverse and medial planes. The electrode locations are determined dividing this perimeters into 10% and 20% intervals. The 10/20 electrode system is still used with clinical and research purposes, but if EEG is to be used for brain imaging, several studies claim that at least 64 electrodes should be used (Gotman, 1982). In denser electrode montages, the most common procedure is to extend the standard 10/20 system placing the electrodes every 10% along the medial-lateral contour and introducing new contours between the existing ones.

EEG is a popular tool mainly because its low-cost and portability. For this reasons it is used in many clinical applications: to diagnose epilepsy, to assess sleep, to study other neurological disorders, to develop brain computer interface (BCI) applications, or to test the brain response under different conditions and stimuli. The main advantages and disadvantages of EEG will be discussed in the next sections.



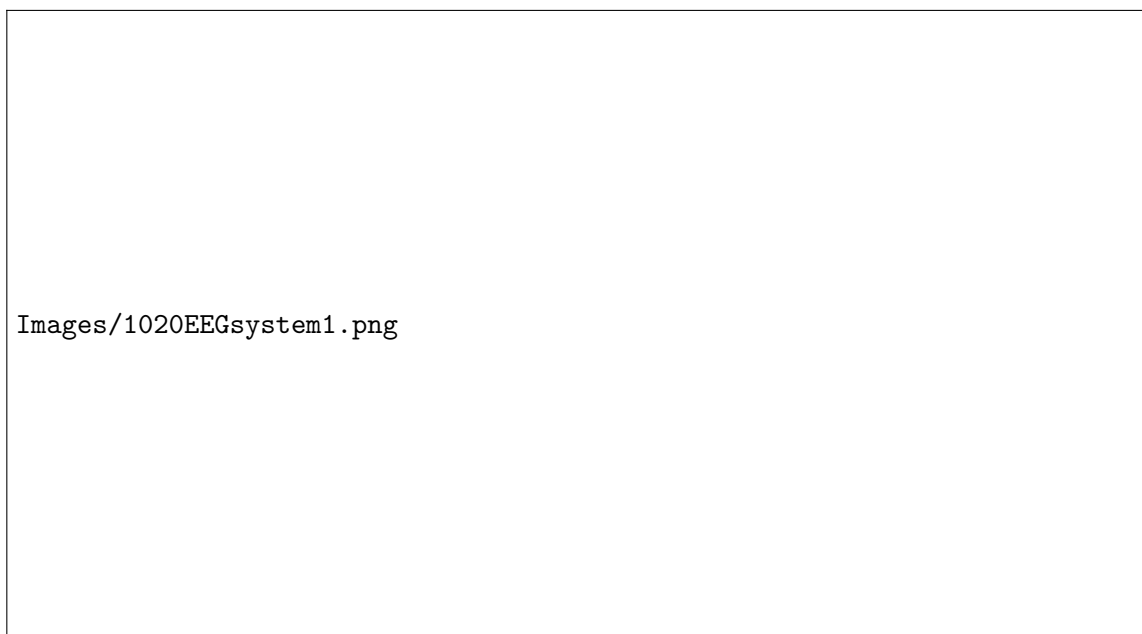


Figure 1.6: The international 10-20 system seen from (A) left and (B) above the head. A = Ear lobe, C = central, Pg = nasopharyngeal, P = parietal, F = frontal, Fp = frontal polar, O = occipital. Image adapted from Ame (1991)

### 1.2.3 Magnetoencephalography

Electric currents measured by EEG are necessarily accompanied by electromagnetic fields. The possibility to record the cerebral magnetic field aroused great interest: as conductivity varies essentially only along the head radius from skull to scalp, the magnetic field outside of the head should be unaffected by these tissues above the cortex (Hari and Salmelin, 2012). This characteristic of MEG is essential: MEG is a much more expensive technique than EEG. However, the high number of sensors and the non-distortion of the acquired signals greatly improve the spatial resolution, maintaining the millisecond time resolution of EEG. For these reasons, MEG allows real-time tracking of brain activation sequences in the source space.

The first magnetoencephalographic recording was performed by David Cohen in 1968 (Cohen, 1968) using copper coils to register the activity. Magnetic fields are considerably lower than electric fields, typical amplitudes of MEG signals are less than 1 pT (Lee and Kim, 2014). For this reason, these first recordings contained low SNR signals. In 1972, Cohen used SQUID sensors (Superconducting Quantum Interference Device) obtaining recordings with increased SNR, comparable to EEG. To preserve its super-conductive properties, these type of sensors have

to be maintained at very low temperatures ( $-269^{\circ}$ ), immersed in liquid helium (Hari and Salmelin, 2012). Currently, MEG systems are composed of 140 to 300 sensors distributed throughout the head. The recordings are performed using a thermally insulated container, known as dewar, where the sensor coils are kept in a helmet that does not touch the patient's head during recordings.

Figure 1.7 shows a diagram of the typical parts of a MEG system. To reduce the strong magnetic environmental noise, MEG recordings have to be carried out inside a magnetically shielded room. The participant can be sitting or lying down, as close as possible to the MEG sensors. Typically, the patient's head shape is digitalized to allow an improved coregistration with an individual or standard anatomical MRI (Gross et al., 2013). As the helmet does not touch the patient's head, the position of the head must be known during the recording. To do so, a Head Position Indicator is used which provides information about the position of the MEG system with respect to the head with an accuracy of about 2mm (Hari, 2004). During MEG recordings, it is possible to record supplementary signals: the electrooculogram (EOG) and the electrocardiogram (ECG) are highly recommendable to posterior preprocessing of artifacts (Gross et al., 2013). Furthermore, EEG and electromyogram (EMG) can also be recorded simultaneously.

A SQUID is a converter from magnetic flux to voltage. Furthermore, to increase the detection efficiency, pickup coils are needed. Among various types of pickup coils, the most common are magnetometers and gradiometers. While magnetometers have better sensitivity to deep and cortical sources, they are more vulnerable to external noises than gradiometers, which in turn are capable of measuring the tangential components of neuroelectric activity. Gradiometers can be axial or planar (see Figure 1.8). Axial gradiometers have higher baseline (distance between the centers of pick-up coils) than planar gradiometers, this provide better sensitivity to deeper sources. For cortical sources, planar gradiometers have better sensitivity to perpendicularly-oriented dipoles. Depending on the thickness of the MSR, the combination of the different type of sensors is selected (Lee and Kim, 2014).

Due to the complexity of the measure system, MEG is an expensive technique only available in few laboratories and clinical centers. However, during the recent years, this neuroimaging tool

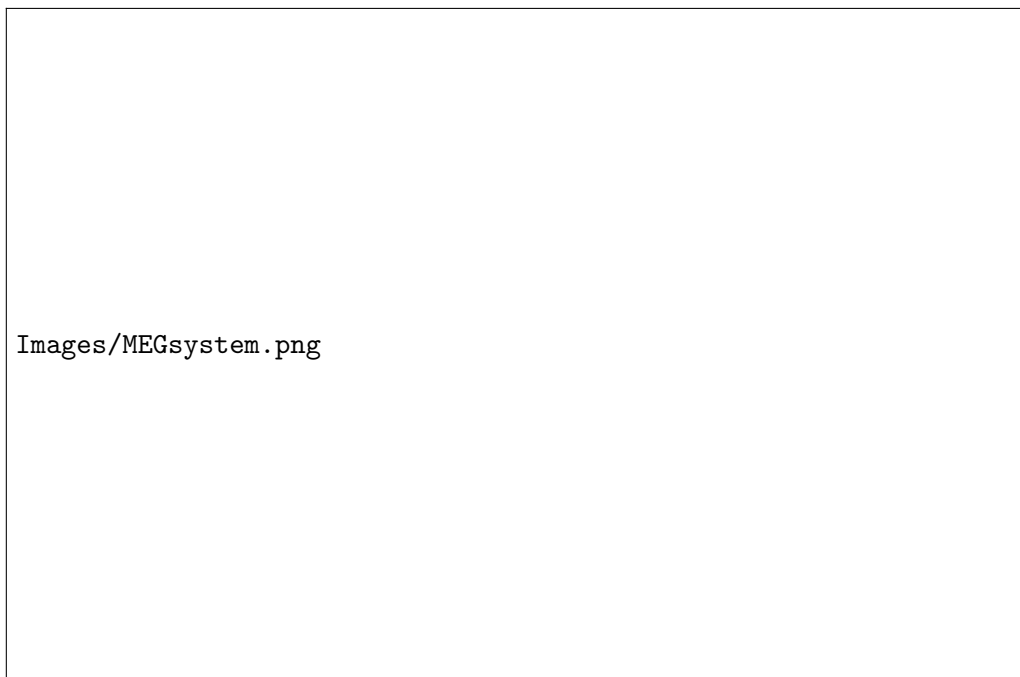


Figure 1.7: Block diagram of a typical MEG system. Adapted from Sternickel and Braginski (2006)

has become more and more important to evaluate brain localized activity at the millisecond scale, providing good spatial resolution. It is important to remark that the spatial resolution in the source space depends on several factors including number of channels, noise, source depth, source strength, the source model and the inverse modeling method that is used to localize the activity (Hari et al., 1988). Under optimal conditions, in superficial sources the resolution that can be obtained is of few milliliters but this number increases when the sources are deeper.

#### 1.2.4 Comparison between MEG and other noninvasive neuroimaging methods

MEG noninvasively evaluates the temporal dynamics of neurological processes with a millisecond resolution and with higher spatial resolution than standard EEG. Other techniques, like functional MRI (fMRI) are capable of analyzing the brain function with a spatial resolution of millimeters (Liu et al., 2006). Recently, there is increasing interest in using techniques that combine excellent temporal resolution with those that provide a superior spatial resolution (Liu et al., 2015a). For this reason it is important to understand which are the advantages and disadvantages of these techniques and the role of MEG recordings in noninvasive neuroimaging

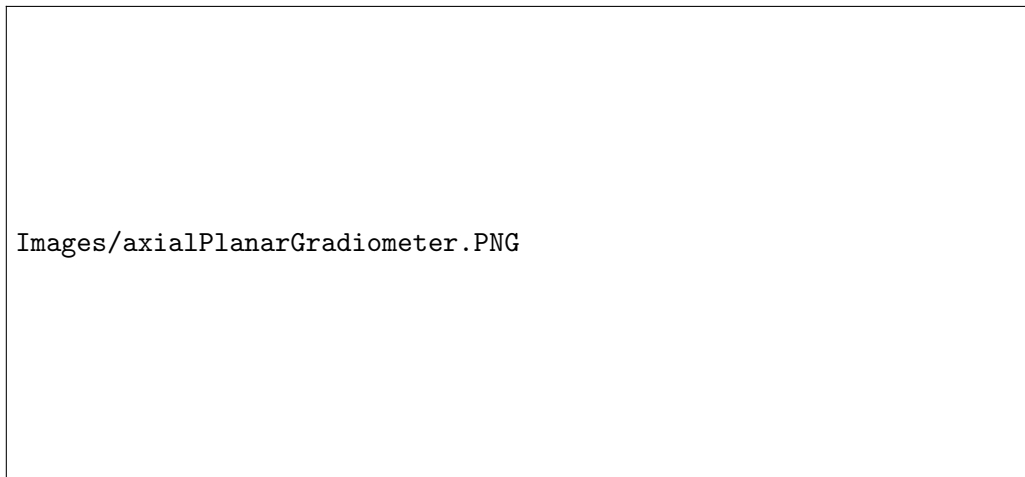


Figure 1.8: (Left) MEG setup measuring the tangential components of neuroelectrical activity, using an axial gradiometer. (Right) MEG setup measuring the tangential components of neuroelectric activity, using a planar gradiometer. Image from (Wendel et al., 2009)

systems.

## MEG vs EEG

EEG and MEG waveforms are similar, as both techniques record the electromagnetic activity generated by the same primary currents in the brain (Niedermeyer et al., 2010). The magnetic field generated by a current dipole in a spherical volume is also dipolar, but the electric and magnetic dipole appear rotated 90 degrees (Hari, 2004). Consequently, the sensitivities of both techniques depend on the orientation of the dipoles. MEG gradiometers are more sensitive to tangential sources, while EEG electrodes are more sensitive to deep and radial sources (Hari, 2004). Thus, both techniques are considered to provide complementary information (Sharon et al., 2007). Several studies have reported the added value of combining MEG and EEG data when performing brain source localization (Aydin et al., 2015; Sharon et al., 2007).

The biggest disadvantage of scalp EEG is its low spatial resolution. The involvement of large areas of brain tissue is required to record EEG (Falco-Walter et al., 2017). Spatial resolution of EEG can be enhanced by increasing the number of sensors. High density EEG (hdEEG) is a recent technique that can record almost 300 channels (Klamer et al., 2015), remarkably enhancing the spatial resolution of the technique. However, the high resistivity of the skull and the more conductive scalp distort and attenuate the electric signals (Cuffin and Cohen,

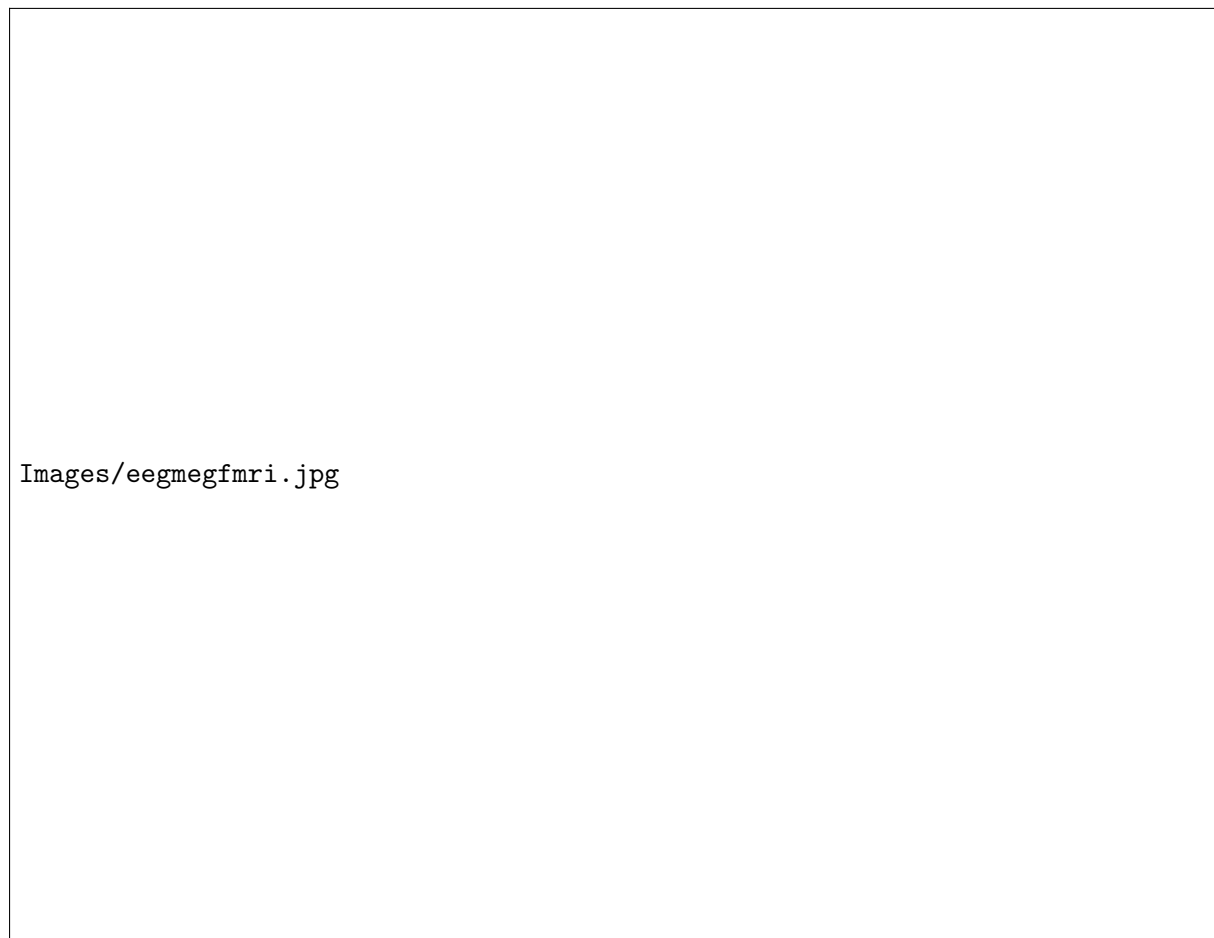


Figure 1.9: Spatial response patterns from fMRI and MEG/EEG in focally-stimulated visual cortex. Image from Sharon et al. (2007)

1979), whereas they do not affect the magnetic fields, conferring a localization advantage of MEG over EEG. Furthermore, the distortion produces the need of more sophisticated forward models (Klamer et al., 2015), and for this reason, MEG recordings are more frequently used in the source space analysis. Other disadvantages of EEG over MEG rely on the sensitivity to movement artifacts, the time of preparation of the subjects, and the need of a reference sensor (Sharon et al., 2007) given that MEG provide absolute measures of the magnetic fields.

The advantages of EEG with respect to MEG are associated with the complexity of MEG systems. The SQUIDS and the magnetically shielded room require a costly set up that has prevented the widespread use of this technique in hospitals and research centers. (Sternickel and Braginski, 2006). However, during the last years, the number of MEG systems has increased notably and new types of MEG sensors, not based in supeconductive materials, are being developed (Boto et al., 2016).

## MRI and fMRI with MEG

Magnetic resonance imaging is the structural imaging modality of choice to screen neurological patients (Asaad and Cosgrove, 2015). This noninvasive technique uses non-ionizing radiation to create useful diagnostic images. The most common MRI procedures include 1.5 or 3 Tesla (T) axial whole brain images with thin slices. The high resolution (sub-millimetric) of this technique allows the identification of differences and abnormalities in brain studies. MRI can also be used to create volumetric data of the brain, providing data for accurate surface models of an individual patient's brain (Xu et al., 1999). Volumetric data is commonly used in MEG studies to obtain the regions and extent of the observed scalp data at the source level in cortical and subcortical locations.

The electrodynamic of the brain is accompanied by a series of neurochemical processes that ultimately result in a measurable change in the MR signal. These processes cause combined effects in cerebral blood flow, blood volume, oxygen extraction and metabolism that are local to the site of cerebral activity (Belliveau et al., 1991). This is the basis of fMRI. The transient increase in the MR signal is usually termed the BOLD haemodynamic response function (HRF). When a stimulus is produced, it takes several seconds for the HRF to peak and return to baseline (Hall et al., 2014). The latency and longevity of the HRF limit temporal resolution to approximately 5 seconds, much inferior to the millisecond resolution of MEG. Multimodal imaging using MEG and fMRI in parallel offers the possibility of measurement of neurophysiological processes with excellent spatial and temporal resolution. Several recent studies have successfully evaluated different pathological and physiological processes combining both techniques (McWhinney et al., 2016; Tewarie et al., 2016; Garcés et al., 2016; Cetin et al., 2016).

### 1.2.5 Invasive EEG and MEG

Brain activity can also be recorded directly on the brain cortex using grid electrodes, or in deep regions using strip electrodes. The first give rise to the so-called Electrocorticography (ECoG), while the second is known as intracranial EEG (iEEG), and both techniques require a surgical procedure to be placed in the head. Due to the high invasiveness of these techniques, electrodes are only implanted in subjects with a pathology that requires precise evaluation at millimetric

spatial resolution of target brain regions (Grova et al., 2016), such as refractory epilepsy.

Invasive EEG provides excellent time and spatial resolution within the implanted region. The spatial resolution is improved not only by the proximity of the electrode to the source but also due to the higher signal-to-noise ratio and because signals are not affected by the tissue distortion. Consequently, these techniques are considered the “gold standard” for the evaluation of localized brain activity (Santiuste et al., 2008).

However, invasive recordings have some significant drawbacks: risks of morbidity because of invasiveness, high cost, limited availability, limited spatial sampling and the possibility of inaccurate localization (Santiuste et al., 2008). High invasiveness is the main disadvantage of these techniques, preventing the studies in large populations of subjects and consequently limiting the research to specific kinds of patients. Another important disadvantage of iEEG and ECoG is that the spatial sampling is limited to the area of implantation, making impossible the visualization of the whole-head activity.

Surgical intervention is one of the most common treatments for pharmacoresistant focal epilepsy (Ramey et al., 2013). MEG, EEG and MRI are the first noninvasive tests in any pre-surgical work-up (Grova et al., 2016), and their role is to help delimitate the area of resection. However, this is not always possible and the implantation of electrodes is needed. In this scenario, noninvasive techniques also play a major role: they are used to delimitate the area where the electrodes should be implanted. Furthermore, there is increasing interest in the simultaneous evaluation of noninvasive MEG and EEG with invasive EEG recordings. While the first can provide a global evaluation of the brain, the second can describe in detail what is happening in deep localized regions (Grova et al., 2016)

### **1.3 Source localization of epileptic focus in pharmacoresistant epilepsies**

The most important diagnostic tool in epileptic disorders is performed using invasive and noninvasive electrophysiology. There is a strong historical link between epilepsy and neurophysiology research that has fostered the advance in both fields (Schomer and Lopes da Silva, 2010). In

this section, the basic clinical characteristics of epileptic disorders are described, especially for refractory epilepsies, which are resistant to pharmacological treatment. After that, the existing signal analysis methods to localize the area generating the seizures are explained.

### 1.3.1 Epilepsy

Epilepsy is a chronic pathology that affects about 1% of the world population (Ramey et al., 2013). It is defined by atypical electrical activity in the brain, which often leads to neurobiological, cognitive and psychological consequences. Epilepsy consists of recurrent paroxysmal events called seizures, defined as hyper-synchronized or excessive abnormal activity of the brain (Fröhlich and Fröhlich, 2016).

When a patient suffers more than one seizure, EEG is commonly used to diagnose epilepsy. The purpose of EEG is to look for epileptiform abnormalities, but EEG recordings are rarely performed during an epileptic seizure. Instead, neurologists look into the resting state recordings, also called as interictal recordings. About 50% of patient show anomalous and distinctive patterns called interictal epileptiform discharges (IEDs) in its first EEG recording (Smith, 2005). IEDs are not only used to diagnose epilepsy, but also as biomarkers of epileptic foci.

Epileptic seizures can be classified using several different schemes. They can be either *idiopathic* (cause unknown) or *symptomatic* (consequence of another disorder of the brain); *partial* (one focal onset zone) or *generalized* (no clear foci); *simple* (no loss of consciousness) and *complex* (loss of consciousness) (Fröhlich and Fröhlich, 2016). Moreover, their classification can be based on the observation of specific neuroelectrical activity and clinical features that enable the definition of *epilepsy syndromes* (Childhood absence epilepsy, Lennox-Gastaut syndrome, benign rolandic epilepsy, etc.) . Finally, the seizures originated at the same areas of the brain usually share some clinical features (semiology) and EEG patterns (Kass et al., 2017). In this sense, seizures can be grouped into *frontal*, *mesial temporal*, *lateral temporal*, *parietal* and *occipital*.

The primary therapy for epilepsy is anti-epileptic drugs (AEDs). Currently, there are more than 20 different AEDs that reduce or eliminate seizures for most patients (Franco et al., 2014). However, around 20 to 40% of patients with idiopathic generalized epilepsies and up to 60% of patients with focal epilepsy may manifest resistance to medication (Alexopoulos, 2013), experi-



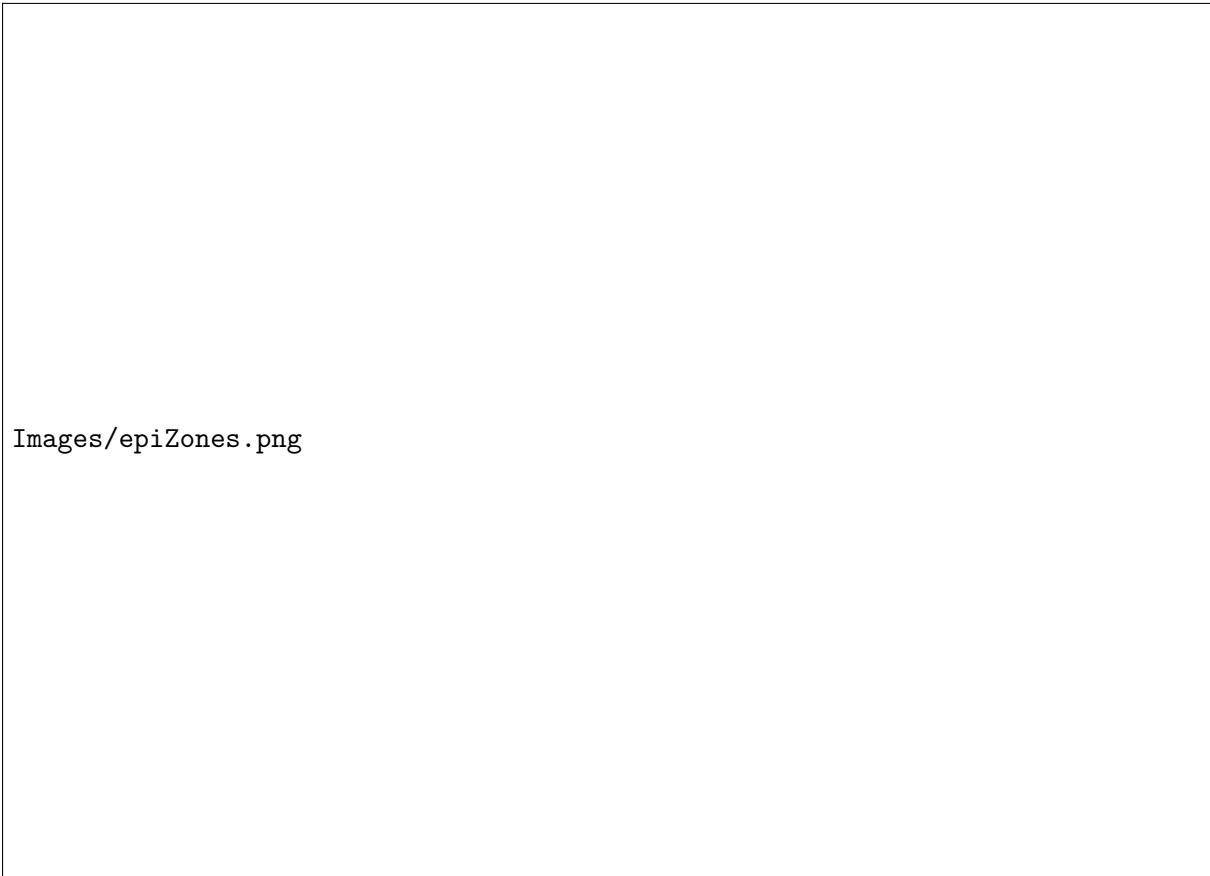
encing disabling seizures after being treated with three or more different drugs. If the epilepsy is partial, the most promising treatment for these patients is the surgical removal of the epileptogenic zone (EZ), defined as the *the minimum amount of cortex that must be resected (inactivated or completely disconnected) to produce seizure freedom* (Lüders et al., 2006; Jacobs et al., 2012). To obtain a successful surgical outcome, neurosurgeons have to previously delimit the EZ with accurately and precisely. Invasive and noninvasive electromagnetic recordings play a decisive role in the presurgical evaluation of epileptic refractory epilepsy.

### 1.3.2 The presurgical evaluation of epilepsy

Surgery is the only treatment that can possibly cure epilepsy in pharmaco-resistant patients. The aim of epilepsy surgery is to remove the EZ with the preservation of the eloquent areas (Rosenow and Lüders, 2001). During the last years, noninvasive functional neuroimaging techniques have proved to be suitable in the presurgical assessment of epilepsy in the majority of cases. Nevertheless, in some patients (25 to 50%) the noninvasive localization is not possible and the use of intracranial EEG is required (Pittau et al., 2014). In preoperative evaluation, the site and extent of the epileptic focus is determined in a multimodal assessment. The pre-evaluation often consists of dedicated structural MRI, functional MRI, and interictal and ictal EEG and MEG recordings.

As previously explained, the EZ is a theoretical zone that cannot be spatially defined. However, there are several cortical zones highly linked with the epileptic brain that can be delimited (see Figure 1.10). Using structural MRI, the epileptogenic lesion can be determined, if exists. The *functional deficit zone* is the region of the cortex with an abnormal function. It can be determined with neuropsychological testing or fMRI. The *seizure-onset zone (SOZ)* is the area where the clinical seizures originate. To determine the SOZ, EEG, MEG, or iEEG recordings during the ictal period are required. The *irritative zone* is the area that generates interictal epileptiform discharges (IEDs) in MEG and EEG. During the last few years, the role and the extent of the *HFO zone*, an area that is considered a further piece of information to better circumscribe the EZ (Tamilia et al., 2017).

The SOZ is generally considered the best estimate of the EZ and is the region removed in most



Images/epiZones.png

Figure 1.10: Schematic representation of the overlapping cortical zones in epilepsy. Different cortical zones are estimated during the pre-surgical evaluation of a patient with epilepsy. These zones can often overlap, providing the epileptologist with concordant findings for the delineation of the epileptogenic zone (EZ). The high-frequency oscillation (HFO) zone is another potentially epileptogenic area that has been recently added to this picture as a further piece of information to circumscribe the EZ. Image from (Tamilia et al., 2017)

epilepsy surgeries (Lüders et al., 2006). Talairach and Bancaud (1973) were the first to assume that the EZ could be defined by placing invasive electrodes in the SOZ and in the regions where the seizure spread (Talairach and Bancaud, 1966). This procedure is commonly known as stereoelectroencephalography (SEEG). In addition to the invasiveness of the technique, ictal recordings are needed to determine the SOZ by these means. Clinical seizures are unpredictable and difficult to be captured by EEG. This procedure is costly and requires very long recording times and discomfort for the patient. Sometimes, neurosurgeons use anesthetic drugs that can activate the seizure foci within 30 seconds, such as etomidate (Ebrahim et al., 1986).

Even when the monitoring of the SOZ is possible, the entire removal of this region does not always lead to a successful outcome (Rummel et al., 2015). Studies have shown positive outcomes that

can vary between 40% to 80% of patients, depending on the type of epilepsy (Schulze-Bonhage and Zentner, 2014). Furthermore, due to the spatial limitation of iEEG, the exact boundaries of the SOZ and the extent of overlap with the EZ remain unknown.

The inability to localize the SOZ limits the decision making for epilepsy surgery (Berg et al., 2003; Uijl et al., 2005). For these reasons, the evaluation of interictal recordings using noninvasive techniques can help in the delimitation of the EZ. Interictal epileptiform events appear more often than seizures and reduce patient discomfort (Staba et al., 2014).


### 1.3.3 Interictal biomarkers for localization of the epileptic focus

Epileptic seizures are a specific biomarker of epilepsy and the localization of the epileptic focus. However, their unpredictable nature and irregular rate of occurrence, ictal recordings are not ideal in terms of time, cost, or risk for this purpose (Staba et al., 2014). Other useful transient pathological disturbances can be recorded between the ictal seizures being the most important the interictal epileptiform discharges (IEDs) and the pathological high-frequency oscillations (HFOs) between 80Hz and 600 Hz.

#### Interictal epileptiform discharges

The neurobiological mechanisms generating IEDs are diverse because focal IEDs show a high variability patterns: spikes, sharp waves, bursts of fast spikes, sequences of fast oscillations, etc., even in the same patient (see Figure 1.11). In spite of these high differences, IEDs of pharmacoresistant epilepsy have been well defined (de Curtis et al., 2012). Interictal spikes related to this type of epilepsies are initiated by large post-synaptic depolarizations. It has been demonstrated that spikes that appear near the SOZ are different from the ones produced in remote regions by synchronized activity, suggesting that these events represent an interplay of multiple neuronal types within complex neuronal networks (Keller et al., 2010).

Interictal spikes are characterized by a large-amplitude rapid component lasting from 50 ms to 100 ms and usually followed by a slow wave of 200 ms to 500 ms in duration (Nowak et al., 2009). IEDs can be detected in MEG and EEG recordings. Its sensitivity highly depends on



Images/decurtisf1.jpg

Figure 1.11: Interictal epileptic discharge (IED) patterns recorded in human partial epilepsies with intracranial electrodes. *a* Interictal spike; *b* group of interictal spikes, *c* sharp wave; *d* fast activity (brushes); *e* paroxysmal slow activity superimposed to slow spikes. Image from (de Curtis et al., 2012)

the orientation and deepness of the sources. While several studies have found higher sensitivity in MEG than EEG (Ramantani et al., 2006; Zijlmans et al., 2002; Iwasaki et al., 2003), other studies claim that the two techniques perform almost the same, achieving higher sensitivity when both are used simultaneously (Baumgartner, 2004).

The main disadvantage of using IEDs as a biomarker for the delimitation of the EZ lies in the fact that these are generated in the irritative zone (IZ), an area that only partially overlaps the EZ (see Figure 1.10), and can appear distant to the lesional site (Penfield and Jasper, 1954). The relationship between the SOZ (generally more linked with the EZ) and the IZ is still an unresolved issue and an important research topic. For some patients, areas generating high spike rates are highly correlated ( $\sim 75\%$ ) with the areas where the seizure initiated. However, in other subjects these areas appear dissociated (Bartolomei et al., 2016). Due to the lack of concordance between these two areas, there is increasing interest in finding other interictal biomarkers to delimitate the EZ. During the last decade, HFOs have emerged as a promising biomarker for epileptogenicity (Jacobs et al., 2012).

### High-frequency oscillations

HFOs are defined as spontaneous patterns above the baseline, clearly distinguished from noise and with at least four oscillations (Worrell et al., 2012). They appear in the frequency range of 80 Hz to 500 Hz and are commonly classified into ripples (80 Hz to 200 Hz) and fast ripples (200 Hz to 500 Hz). Several recent studies have evaluated high-frequency oscillations as a specific biomarker for epileptogenicity (Jacobs et al., 2012; Fujiwara et al., 2012; Sun et al., 2015b).

High-frequency oscillations appear also in the normal mammalian brain, and are then called physiological high-frequency oscillations. However, several studies have pointed out that there could be important differences between the neuronal processes of the pathological and physiological HFOs (Staba et al., 2014). Although the generation of pathological HFOs is still an open question, several observations have shown that these oscillations are generated by the neurons near the epileptogenic focus (Jefferys et al., 2012). There are studies that even suggest that HFOs could have a causal role in the ictogenesis, which would have an impact in improving the epilepsy treatment (Jiruska et al., 2010).

The relation between epileptic spikes and HFOs is still an open discussion. Early studies reported that most of the observed fast ripples appeared at the same time as spikes (Engel Jr et al., 2009). Urrestarazu et al. (2007) defined three different cases in which an HFO can occur: (i) completely independent of IEDs, (ii) together with spike and visible in the unfiltered data and (iii), together with the spike but invisible in the unfiltered spike (Figure 1.12). Subsequent studies provided evidence that HFOs and spikes have different neurophysiological mechanisms. On the one hand, HFOs seem to be more specific to the SOZ (Jacobs et al., 2008; Crepon et al., 2010). On the other hand, when the epileptic medication is reduced, HFOs tend to increase in number while IEDs do not exhibit this trend (Zijlmans and Dubeau, 2009). This indicates that both biomarkers behave differently under changing conditions. Furthermore, spikes co-occurring with HFOs have shown to be more closely related to the SOZ (Jacobs et al., 2008) than those occurring alone. This differentiation can be helpful to distinguish between *good* and *bad* spikes, originating or not inside the EZ (Tamilia et al., 2017).

Due to the low signal-to-noise ratio of noninvasive electromagnetic signals at high frequencies (Muthukumaraswamy, 2013), HFOs are commonly detected in intracranial recordings. Visual

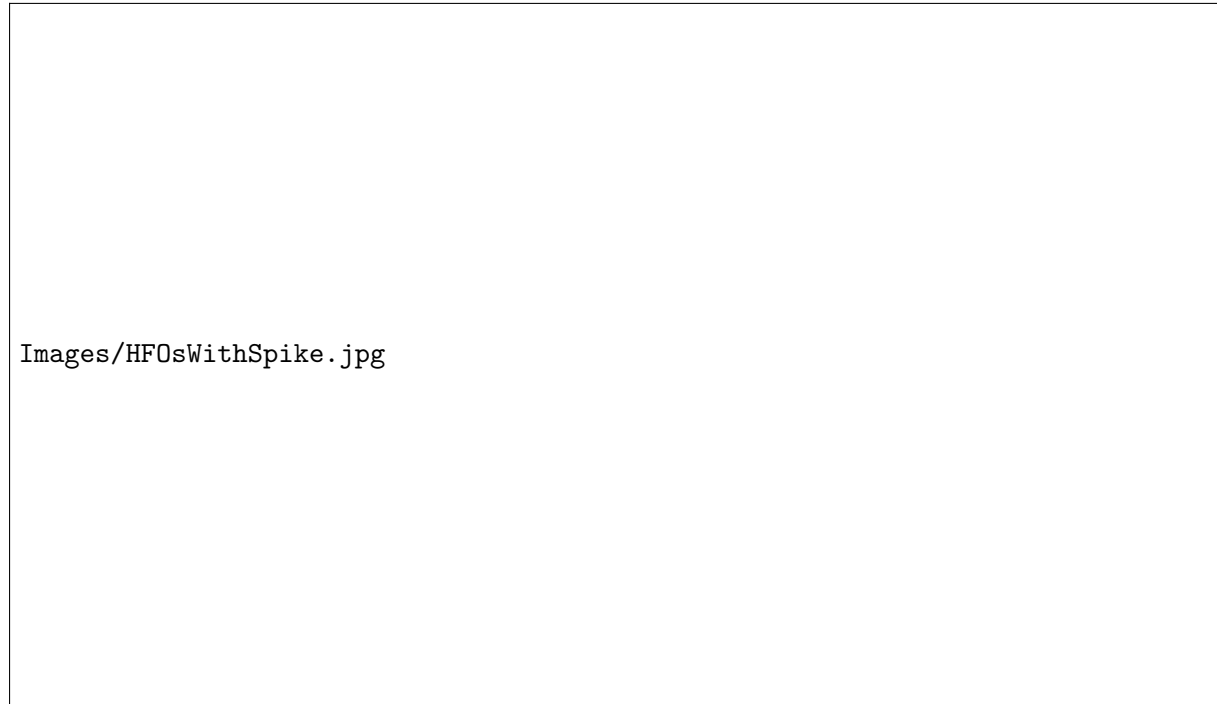


Figure 1.12: HFO classification. (A) HFO visible in spike; (B) HFO not visible in spike; (C) HFO visible, independently of a spike. Top: non-filtered spike; middle: signal filtered with high-pass filter of 80Hz; bottom: signal filtered with high-pass filter of 250Hz. Image adapted from (Urrestarazu et al., 2007)

marking of HFOs is highly time-consuming, but several automatic algorithms have been proposed both in the time and in the time-frequency domains (Liu et al., 2016; Burnos et al., 2014; von Ellenrieder et al., 2012; Zelman et al., 2012). Time-frequency detectors are useful to reduce false positives because they exploit the assumption that an HFO should be a short-lived event with an isolated spectral peak at a distinct frequency (Cho et al., 2012; Crepon et al., 2010).

The detection of HFOs in noninvasive signals is a field of increasing interest. Some recent studies have shown that HFOs can be detected in EEG (Papadelis et al., 2016; Andrade-Valenca et al., 2011; Kobayashi et al., 2010; Zelman et al., 2014) and in MEG (van Klink et al., 2016; von Ellenrieder et al., 2016; Nissen et al., 2016b). However, due to the high number of channels, the low signal-to-noise ratio of noninvasive techniques, and the lack of a well-established definition of HFOs, the automatic detection of these oscillations and the determination of the area generating them is still a challenging task. The noninvasive detection and localization of HFOs with MEG would significantly expand the clinical utility of these biomarkers that, to date, are only detected with patients with implanted intracranial electrodes.

### 1.3.4 Methods for noninvasive localization of the epileptic focus in MEG

In the so-called inverse problem, source reconstruction methods are used to estimate where the activity recorded from the scalp was originated. Before such an estimate can be computed, a set of *a priori* assumptions have to be computed to solve the forward problem, in which the scalp potentials and external fields for a specific set of neural current sources are computed (Baillet et al., 2001).

The estimation of the induced magnetic fields is given by a *Head Model*. The most common models used in most clinical and research applications are two: the *spherical head models*, where the geometry of the head is fitted into spheres and the *realistic head models*, that use the anatomical information obtained by MRI images. Two popular *spherical head models* are the single sphere model (Cuffin and Cohen, 1977) that consist of a set of nested concentric homogeneous spherical shells representing brain, skull, and scalp (Mosher et al., 1999; Zhang, 1995); and the overlapping spheres model (Huang et al., 1999), where a sphere is fit separately for each sensor according to a local region of the surface closest to that sensor. To compute the volume conductor using a *realistic head model*, two approaches can be used: the boundary element method (BEM) assumes isotropic and homogeneous tissues (brain, skull, scalp) obtaining simplified field equations that only depend on the surface (or boundary) of the or the compartments (Nolte, 2003); and the finite element method (FEM) (Ermer et al., 2001), where the solution of the forward problem is solved for arbitrary, neither homogeneous nor isotropic, distributions resulting in equations that depend on the whole volume of the tissues. In order to solve the problem, the volume is divided into smaller pieces where an approximation of the solution is obtained. MEG measurements are less sensitive to the effects of volume currents than EEG, consequently, the simpler spherical head models work well for MEG but in the case of EEG, realistic head models have to be considered (Baillet et al., 2001).

Regarding MEG source estimation, several methods are available for that purpose: Equivalent current dipole (ECD), linear constrained minimum variance beamformer (LCMV-Beamformer), synthetic aperture magnetometry (SAM), dynamic imaging of coherent sources (DICS), partial canonical correlation/coherence (PCC), minimum norm estimation (MNE), multiple signal classification (MUSIC), and low-resolution electromagnetic tomography (LORETA), among

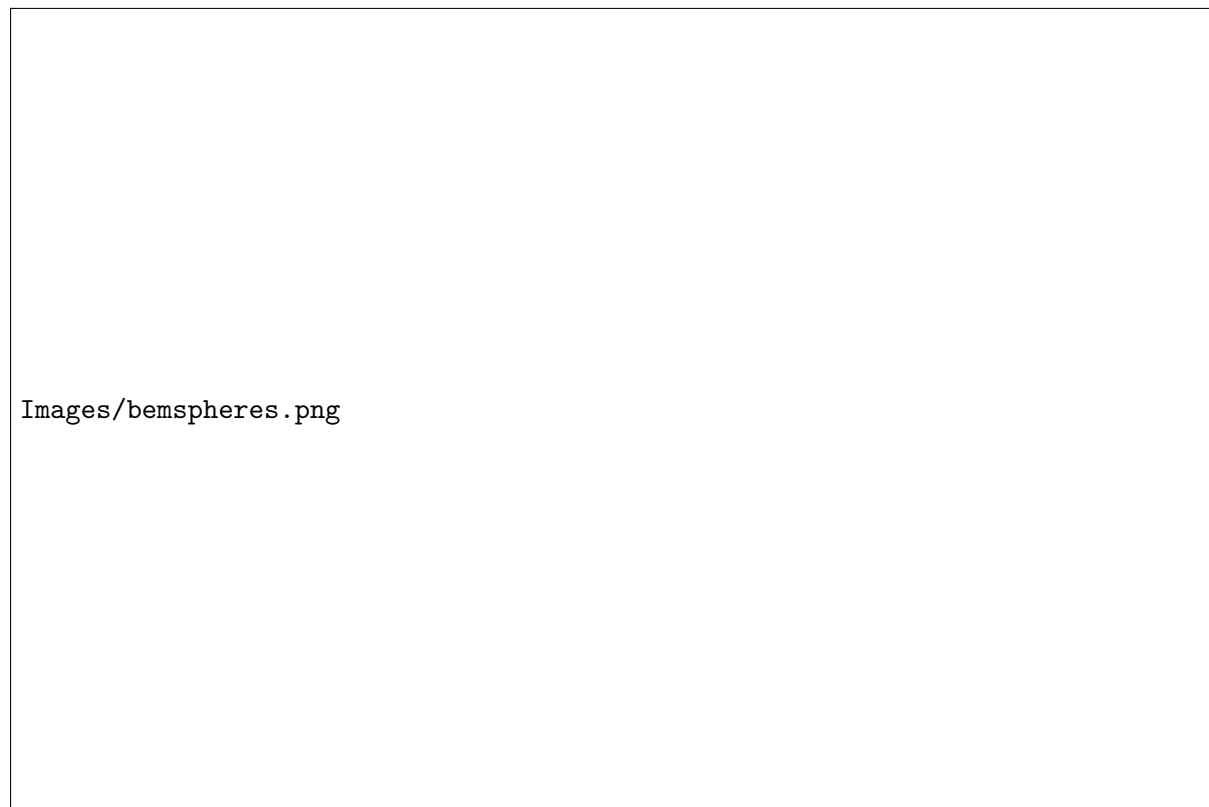


Figure 1.13: Example of computation of a head model with a) a single sphere, b) with overlapping spheres (one sphere is computed for each channel) and c) BEM method. Head shapes and images generated with Brainstorm (Tadel et al., 2011)

others. The following paragraphs focus on the first two: ECD and the LCMV-Beamformer techniques. ECD is commonly used to estimate the sources generating IEDs (Stefan et al., 2003; Fischer et al., 2005; Oishi et al., 2006); LCMV-Beamformer is a novel approach that, due to its performance as a spatial noise filter, has proven to be useful in reducing the high-frequency noise and to detect HFOs that were not visible at the scalp level (van Klink et al., 2016; Nissen et al., 2016b).

### Equivalent current dipole

Once the forward problem is solved, that is, the estimation of how the sources distribute through the volume is available, the ECD method uses this information and the data from scalp sensors to evaluate a set of parameter values that minimizes the difference between observations and predictions from the model. The minimization procedure is an iterative optimization problem that requires the specification of an initial guess of what the solution may be, that means, to



specify the initial position and the number of dipoles. The risk of overfitting the data increases when the number of parameters with respect to the number of channels also increase (Heller and Volegov, 2014). For this reason, no more than a few number of dipoles are set. To avoid local minima, the localization procedure is typically repeated several number of times using different starting points and selecting the solution that gives the best fit in each case.

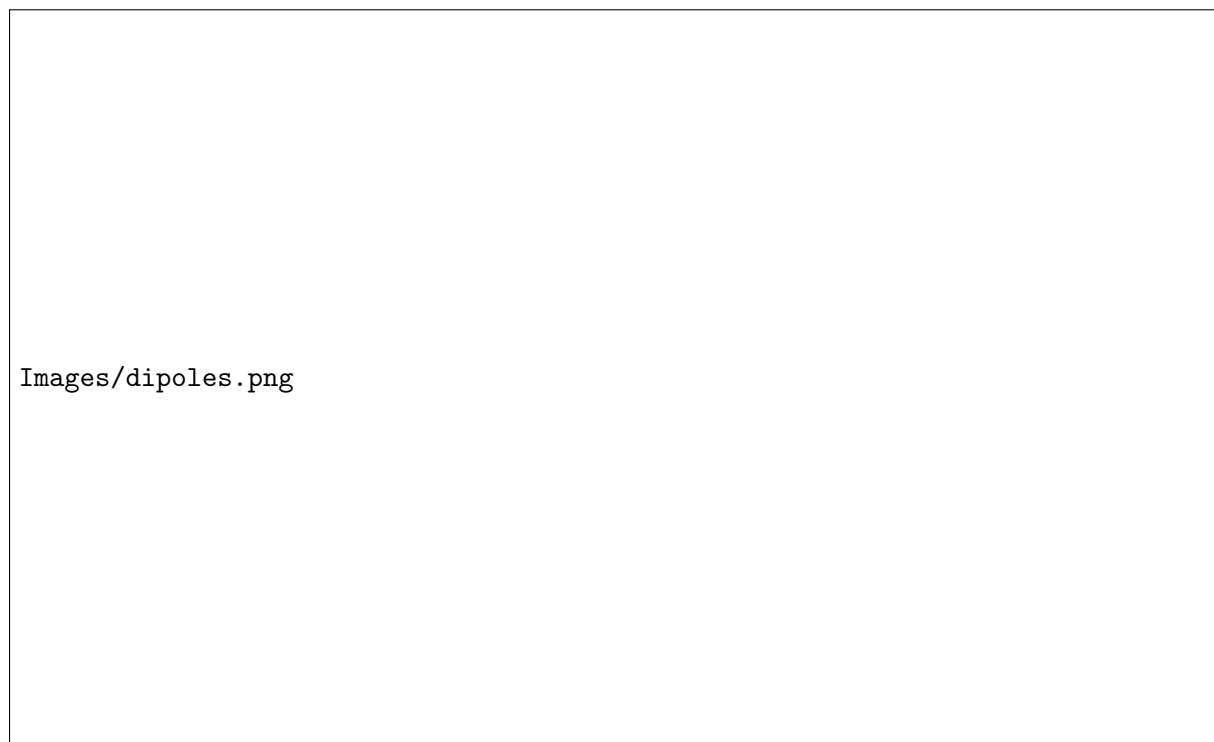


Figure 1.14: Visualization of a dipolar distribution in a) Most relevant scalp signals, b) Topographic disc c) Whole-sensor 2D image d), e) and f) 3D helmet activation map. Images generated with Brainstorm (Tadel et al., 2011)

Whenever it is reasonable to assume that an electromagnetic potential arises from a single or a few sources, dipole source localization is the simplest method to determine the center of the sources (Lütkenhöner, 1998). The dipolar nature of the electromagnetic signals was first observed in the fields obtained by evoked somatosensory responses (Barnard et al., 1967). The common practice to obtain the ECD from MEG data is to observe the scalp signals using different visualization approaches (see Figure 1.14) and look for dipolar patterns in the signals, such as the ones produced by IEDs. To evaluate the performance of the fitting algorithm, the *goodness of fit* can be computed as the difference between the original scalp signals and the ones computed by the ECD model. The *confidence volume* measure the intervals where the solution is plausible (Heller and Volegov, 2014). The most common approach is to employ a Monte-Carlo

technique generating a dipolar model with added noise and compute the ECD several times to see how the obtained dipole spread throughout the volume. In order to validate a dipole, high *goodness of fit* values with low *confidence volume* are expected.

## Beamforming

Beamforming techniques were first developed for radar applications to amplify the sensitivity of specific sources of interest and to attenuate signals coming from other locations (Van Veen and Buckley, 1988). This concept can be exploited using MEG and EEG signals under the main assumption that two distinct cortical areas are not linearly correlated in their activation (Van Veen et al., 1997). If signals are correlated, the beamforming analysis will return low power sources.

Beamforming is a scanning technique that address the activation of a desired number of dipoles inside the head. The position and the number of the sources can be decided *a priori*. The purpose of this technique is to enhance the signals coming from a particular position, while reducing the signals coming from other directions (Zhang and Liu, 2015). For this reason, is considered as an spatial filtering technique that passes the activity at the target location with unit gain while suppressing the contribution of other sources (Van Veen et al., 1997).

The relationship between the scalp MEG signal  $B$  and the neuronal sources is given by the following equation (Hämäläinen et al., 1993):

$$B = LQ \tag{1.1}$$

where the  $(N \times 1)$  matrix  $Q$  is the strength of the neuronal activity and  $L$  is the leadfield matrix  $(M \times N)$ , with  $M$  sensors and  $N$  number of elements in the pre-defined source space. The leadfield is completely defined by the sensor configuration, the head model and the source model. The simplest source is the ECD explained in the previous section.

With the observations from the scalp signals in time,  $B(t)$ , the strength for each neuronal source

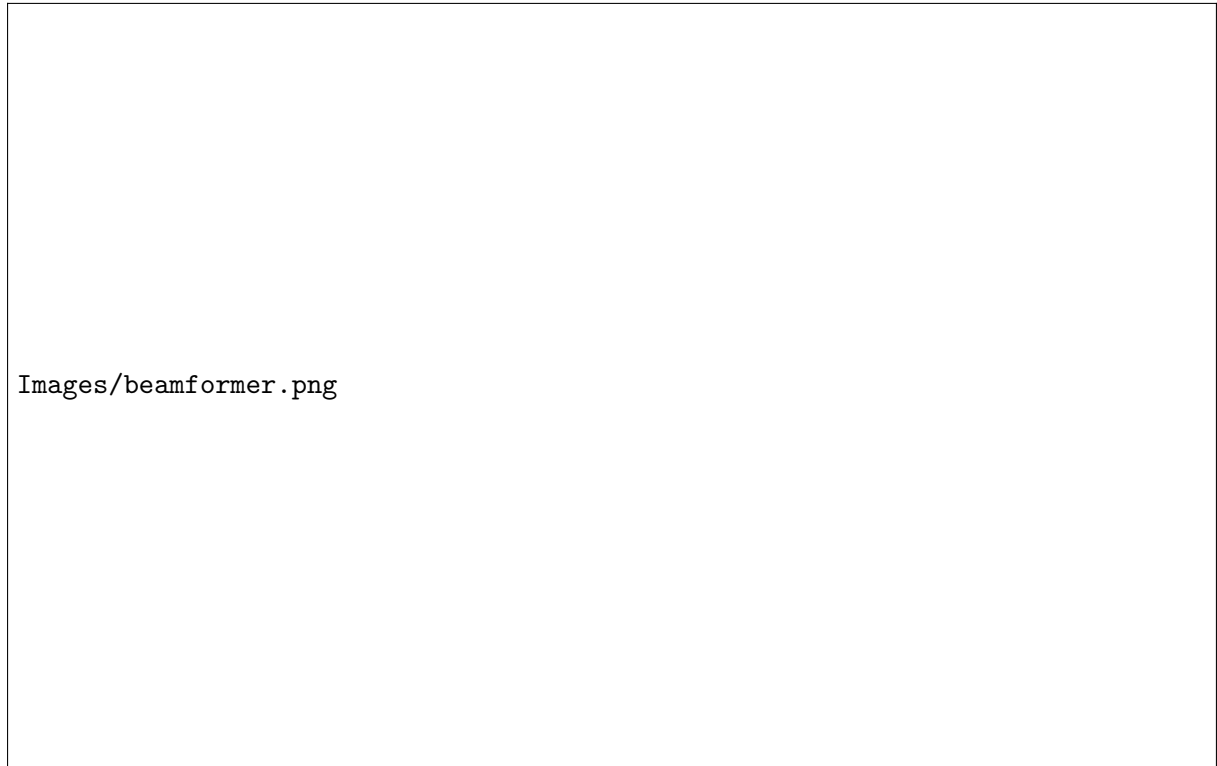


Figure 1.15: Schematic representation of beamforming analysis. The neuronal signal at a location of interest is estimated as the weighted sum of the MEG channels ( $m_1 \dots m_n$ ) resulting into a Virtual Sensor (VS).

can be expressed as:

$$Q = C_j L^T C_b^{-1} B \quad (1.2)$$

where  $C_j$  and  $C_b$  are the source current and data covariance matrices. The differences among Beamforming and other source reconstruction techniques rely on the assumption that is made about the source current covariance matrix (Hillebrand and Barnes, 2005). Beamforming assumes that all sources are uncorrelated, i.e.,  $C_j$  is a diagonal matrix where each diagonal element, corresponding to a location  $\theta$ , can be related to the measured data as follows (Mosher et al., 2003):

$$\sigma_\theta = (L_\theta^T C_b^{-1} L_\theta)^{-1} \quad (1.3)$$

Combining equations 1.2 and 1.3 gives:

$$Q_\theta = (L_\theta^T C_b^{-1} L_\theta)^{-1} L_\theta^T C_b^{-1} B = W_\theta^T B \quad (1.4)$$

The value of the diagonal element  $C_j$  (Equation 1.3) determines the eventual power of any source

at a certain location  $\theta$ . If all the data covariance  $C_b$  correspond to a single source, a maximum will be obtained in equation 1.3 but if this source shares variance with another, the estimated power  $Q_\theta$  will decline. The effect of correlated activity depends on the distance between sources: for high correlated activity between two closely spaced sources the reconstruction might be erroneous and if the sources are well-separated those can be completely canceled (Van Veen et al., 1997). Still, beamforming have proven to be robust when dealing to partially correlated sources.

The Beamforming can be computed by dividing the source space into a tridimensional grid (or voxel space). In order to avoid false detection caused by noise, the resulting 3D image must be normalized with respect to an estimation of the noise power (Hillebrand and Barnes, 2005; Van Veen et al., 1997).

Once the normalization is applied, the peaks of the beamforming 3D image can be obtained. An estimate of the time course of the neuronal activation of interest (or any point of the grid) can be achieved (see Figure 1.15). The positions where the time course of the neuronal sources are computed are commonly known as *Virtual Sensors* (VS). Each virtual sensor time course signal is obtained as the weighted sum of each of the MEG sensor data, suppressing the signal from noise. In section 1.4.3 the ability of LCMV-Beamformer to act as a spatial filter will be explained.

## 1.4 Artifacts and rejection techniques in MEG

Brain signal recordings can be easily contaminated both by external noises and by interferences coming from inside the body, such as muscular or cardiac activities. The reduction of artifacts is a crucial step in signal analysis because meaningful physiological data can stay masked behind the artifactual activity, or even leading to inaccurate or wrong interpretation of the source of the signals. Thus, signal pre-processing is an imperative step to successfully localize epileptic focal activity. Many acquisition systems are able to reduce some artifacts related with external magnetic noise, stimulation, etc. However, there are other sources of artifacts present in the electromagnetic signals that cannot be reduced *a priori*. In the following section, the most frequent artifacts in MEG data are described, as well as the most important techniques for its

reduction.

### 1.4.1 Physiological artifacts

Physiological artifacts are generated by the patient itself and include cardiac, muscular, ocular, respiratory activity among many others. In this section, a brief description of the most common physiological artifacts is given, with special attention to muscular artifacts, which overlap the HFOs frequency band.

#### Ocular artifact

The eye can be represented as a small electrical dipole oriented from the negatively charged retina to the positively charged cornea (Croft and Barry, 2000). When the eye moves, the orientation of the dipole changes, altering the associated electromagnetic fields in the frontal region, near the eyes. For example, blinks also generate artifacts due to the change in the intensity of the dipole created by the movement of the eyelid over the eyeball (Hämäläinen and Hari, 2004).

#### Cardiac artifact

The magnetic field of the heart is significantly larger than the normal or pathological brain activity. Its amplitude reaches a few hundred pT over the chest (around 100 times the amplitude of an epileptic spike). The magnitude of the cardiac artifact in MEG depends on the position of the head with respect to the heart (Hämäläinen and Hari, 2004), and varies from subject to subject. Furthermore, in children recordings this interference may be stronger due to the shorter heart-to-brain distance.

#### Muscular artifact

The power spectrum of a contracting muscle typically shows a bandwidth activity between 20 Hz to 300 Hz (Criswell and Cram, 2011). While most muscles near the jaw have peak frequencies around 20 Hz to 80 Hz, posterior head muscles (sternocleidomastoid, splenius capitis and trapezius) have higher peak frequencies (around 100 Hz) (Muthukumaraswamy, 2013). Studies in EEG blocking the neuromuscular activity with *cistaracurium* (Whitham et al., 2007, 2008) showed that even in the electrodes in the center of the head the muscular activity produced a frequency spectrum around 10 times higher in the 80 Hz band. In MEG, there are currently no studies evaluating this effect, but is expected less muscular artifact since the magnetic fields

falls off rapidly as distance increases to the primary dipole generators and secondary volume currents contribute little to the external MEG field (Hämäläinen et al., 1993). This effect has been described in simultaneous MEG/EEG recordings (Claus et al., 2012). The main difference between muscular noise and high frequency oscillations is that the latter exhibit a more sinusoidal behaviour (grouped in a narrow frequency range) than former, which have a more spiky nature (contribution of a wider frequency range)

### 1.4.2 Non-physiological artifacts

The recordings can be contaminated by numerous non-physiological artifacts generated from the immediate subject surroundings. Common non-physiological artifacts include those generated by monitoring and electrical devices, and the power line (50 Hz or 60 Hz). In MEG recordings, most of these interferences are properly attenuated thanks to the Magnetically shielded room. Furthermore, MEG systems are highly sensitive to metallic interference. If the patient possess non-removable metallic devices, they considerably affect the recorded signal as the source of interference is inside the shielded room.

#### **Metallic interference**

MEG systems are sensitive to metallic ferromagnetic materials. Metallic interference may come from inside the head, such as implanted intracranial electrodes, dental ferromagnetic prosthesis or brackets, or from outside, such as pacemakers and vagal stimulators (Vrba, 2002). To try to minimize the effect of these interferences, an extremely magnetic hygiene inside the shielded room is required (Hillebrand et al., 2013). Recordings have to be performed with subjects trying to avoid any kind of movement, and even a demagnetization of the subject can be carried out. For this reason, MEG signal recording requires very careful preparation that can only be performed by highly trained specialists. Despite all precautions, sometimes it is not possible to eliminate all sources of metallic artifacts and highly distorted recordings are obtained.

Typically, these artifacts appear modulated by breathing and cardiac rhythms (Hillebrand et al., 2013) due to the great sensitivity to movement. The amplitude of metallic artifacts is typically much higher than the amplitude of cerebral signals and can even reach values larger than 100 fT (Cheyne et al., 2007). Metallic artifacts affect the whole record, overlapping brain activity,

and may alter all head channels with varying amplitudes. Usually, there are a certain number of channels whose high level of contamination masks cerebral activity almost completely

### 1.4.3 Rejection techniques

There are several useful methods to reduce interferences in electromagnetic multichannel signals. These can be simple methods such as band-pass or notch filtering to more advanced methods. In this section some of the most common and efficient methods to reduce MEG artifacts will be explained.

#### Blind source separation methods

Blind source separation (BSS) can be used to decompose complex EEG or MEG data into simpler components based on statistical assumptions without using a physical forward model. The term *source* here refers to an original signal while *blind* indicates that no information is known about the mixing process of the sources (Hyvärinen et al., 2001). The first assumption that is made in BSS methods is that the recorded signals in the scalp are a mixture of the original signals (source). This problem can be mathematically described as:

$$x = As \tag{1.5}$$

where  $x$  is the recorded signal with  $n$  channels and  $s$  is the original signal with  $m$  components.  $A$  is the  $n \times m$  mixing matrix. The second assumption is that the mixture is linear and the third is that some type of independence should exist between the original components.

The BSS algorithms that exist differ on the statistical independence that is assumed. In general, the classification is divided into two main groups: the algorithms that use second order statistics (SOS) and those that exploit the high-order statistics of the signals (HOS).

The SOS methods only consider the correlation information to evaluate the independence between sources. The assumption implies that the components have no spatiotemporal or spatial time-frequency correlations between them (James and Hesse, 2005). The mixing matrix is ob-

tained taking into account a set of lagged covariances (Hyvärinen et al., 2001). One example of this kind of algorithms is the Algorithm for Multiple Unknown Signal Extraction (AMUSE), in which only two lags are considered (Tong et al., 1991). First of all, AMUSE decorrelates the signals at  $\tau_0 = 0$ , or in other words, applies a PCA to the input data. Secondly, the signals are decorrelated again but adding a time delay  $\tau_1$  (usually equal to 1 sample). The main advantage of AMUSE lies on its low computational complexity (Cichocki et al., 2005). Although simple, SOS algorithms can deal with gaussian sources and are robust in presence of white noise (James and Hesse, 2005).

The algorithms that employ the HOS to solve the BSS problem are commonly known as Independent Component Analysis (ICA) techniques. The probability distribution of the sources must be non-gaussian in order to be considered independent (Hyvärinen et al., 2001). Two of the most popular approaches are FastICA and Infomax algorithms. FastICA (Hyvärinen and Oja, 2000) is a fast, fixed-point iterative algorithm which searches projections that maximize the non-gaussianity of the components by computing their kurtosis. Infomax relies on the information maximization principle (Bell and Sejnowski, 1995). This algorithm maximizes the output entropy of a neural network with nonlinear outputs. The original Infomax is able to deal only with super-gaussian sources, however, the extended Infomax (Lee et al., 1999) is able to estimate sub-gaussian sources.

The performance of SOS and HOS algorithms in reducing artifacts from MEG and EEG signals has been tested in several studies (Fatima et al., 2013; Breuer et al., 2014; Mantini et al., 2008; Escudero et al., 2011; Romero et al., 2008, 2009). The algorithms listed above have shown different performances depending on the application or on the type of artifacts. For this reason, all of them are still used in the current applications, practice and research.

### **Signal space separation methods**

Signal space separation (SSS) is a method which takes into account the Maxwell equations for electromagnetism and is able to separate magnetic sources inside and outside the brain (Taulu et al., 2004). One of its main limitations is that artifacts from sources near the sensor array, such as metallic or dental implants, project into both subspaces and are not properly



removed. For this reason, the method has been extended and termed as temporal Signal Space Separation (tSSS) (Taulu and Simola, 2006). These techniques have proven to be effective metallic interference (Hillebrand et al., 2013). However, they are only applicable to Elekta-Neuromag systems and their algorithms are not published and not freely available.

### Beamformer spatial filtering

The beamformer algorithm act as a filter for activity in a target location of interest. This is known as *spatial filtering* (Figure 1.16). The beamformer weights explained in the 1.3.4 section determine the spatial filtering characteristics of beamformer increasing the sensitivity in a region of interest and therefore attenuating the noise as well as the activity from other (remote) active brain regions (Mosher et al., 2003). While temporal filtering involves operating on times samples of a signal; spatial filtering involves processing spatial samples of a signal. The pass-band of the signal at the location of interest  $\theta$  must have an unit response:

$$W_{\theta}^T B(\theta) = 1 \quad (1.6)$$

while at any other point  $s$  must be satisfied:

$$W_{\theta}^T B(s) = 0 \quad (1.7)$$

In practice, to fully suppress the contribution of other sources is not possible. The idea behind LCMV-Beamformer (Van Veen et al., 1997) used to address this problem is to find a  $W_{\theta}^T$  minimize the signal power (or variance) maintaining the linear response constraint from equation 1.6.

The signal at each location in the brain is composed by three component dipole (each one oriented in a direction). Hence, three spatial filters for each location are computed. Each virtual sensor will have weighed contribution of the MEG sensors (see Figure 1.15) for each one of the locations. However, The interpretation of the source signals is facilitated if the posterior measurements are performed in if plain channels rather than a triplet of channels. The most common option is to project the time-series along the dipole direction that explains most



Figure 1.16: General scheme of the idea behind spatial filtering. The ideal spatial filtering is only sensitive to the source of interest and non-sensitive to other interference sources. In reality, it exists some spatial leakage. A general filter, such as dipole fitting procedure, do not actively suppress the interfering source. The LCMV-Beamforming is an optimized spatial filter that is not only sensitive to the source of interest but is also actively suppressing the interfering sources.

variance. This projection is equivalent to determining the largest (temporal) eigenvector and can be computationally performed using the singular value decomposition (svd).

## Chapter 2

# Problem statement

### 2.1 Introduction

Epilepsy is one of the most common neurological diseases, which affects 1% of the world population (Ramey et al., 2013). The primary therapy for epileptic patients is anti-epileptic drugs that successfully eliminate seizures in about 60% of patients (Franco et al., 2014). The most promising treatment for the remaining 40% is surgical intervention for removing or resecting the area of the brain producing seizures (Jacobs et al., 2012), the epileptogenic zone (EZ).

During the presurgical evaluation of patients, noninvasive techniques play a major role in the delimitation of the EZ. However, in some patients (25% to 30%) the noninvasive localization of the affected area is not possible and the use of invasive electrodes is required (Pittau et al., 2014). These electrodes are implanted in the areas where the epileptic focus is expected, providing an excellent spatial resolution in that area and a higher signal-to-noise ratio. Apart from its high invasiveness, one of the main limitations of intracranial EEG (iEEG) is that only provides a good spatial resolution in the area of implantation. Thus, iEEG does not allow the delimitation of the exact boundaries of the EZ, only providing a locally limited neurophysiological picture (Muthukumaraswamy, 2013).

## 2.2 Noninvasive detection of focal epileptic activity in MEG

The delineation of the EZ is commonly approximated by the area where the clinical seizures originate, the *seizure-onset zone* (SOZ) (Lüders et al., 2006). The SOZ is determined with recordings during the ictal period, but due to the unpredictability of clinical seizures, the delimitation of the SOZ is not always possible (Uijl et al., 2005). The localization of Interictal Epileptiform Discharges (IEDs) sources is a common practice in the presurgical evaluation of epilepsy (Nissen et al., 2016a), but IEDs are generated by the *irritative zone* (IZ). This area partially overlaps the EZ and in some cases can appear distant to the epileptogenic lesion (Tamilia et al., 2017). The relationship between the IZ and the SOZ is still an important research issue (Song et al., 2015; Melani et al., 2013; Strobbe et al., 2016). During the last decade, high-frequency oscillations have emerged as a promising biomarker for epileptogenicity (Jacobs et al., 2012). These interictal oscillations seem to be more specific to the SOZ than IEDs (Jacobs et al., 2008; Crepon et al., 2010).

MEG is a noninvasive technique that, like scalp EEG, records the electromagnetic activity with excellent temporal resolution. Both techniques can be used to reconstruct the focal sources generating the epileptogenic activity. The main advantage of MEG over scalp EEG is that their signals are less distorted by the high resistivity of the skull and the more conductive scalp (Cuffin and Cohen, 1979), providing a better source localization with simpler forward models (Klamer et al., 2015). Furthermore, MEG systems are generally equipped with a larger number of sensors than common EEG systems. For these reasons MEG is more frequently used in the source space analysis.

Noninvasive MEG is an important tool for preoperative evaluation because it can guide the placement of invasive electrodes, the current gold standard. In some cases, MEG and other noninvasive techniques can supply sufficient information for a surgical intervention without invasive recordings, thus reducing invasiveness, discomfort, and cost of the presurgical epilepsy diagnosis (Aydin et al., 2015). However, to enable the evaluation of the areas involved in epileptic processes, MEG recordings have to be clean of artifacts that distort the signal, produce inaccuracies in the localization and even might make it not possible at all. In this thesis, two types of interferences that affect MEG recordings are studied: metallic artifacts that distort the MEG

signals in the frequency ranges that overlap with IEDs, and the high-frequency noise that masks the activity of HFOs.

## 2.3 Objectives

### Main objective

The main objective of this thesis is the development and validation of methods for the effective noninvasive localization of interictal epileptogenic biomarkers with magnetoencephalography.

### Specific objectives

To achieve the main objective, this thesis strives for the following specific objectives:

- I To develop algorithms, using freely-available signal analysis toolboxes, to improve the signal-to-noise ratio of MEG recordings in low and high frequencies.
- II To compare the performance of different BSS algorithms in the reduction of metallic interference.
- III To reduce metallic artifacts in MEG recordings automatically using blind source separation (BSS) techniques, and to evaluate the improvement of the signal-to-noise ratio quantitatively.
- IV To evaluate the influence of metallic interference and its reduction in the detection and localization of interictal epileptiform discharges.
- V To reduce high-frequency noise to detect high-frequency oscillations in MEG signals.
- VI To develop an automatic method to detect high-frequency oscillations in MEG signals, and to compare its detection with intracranial recordings, the current gold standard.
- VII To localize the areas generating pathologic high-frequency oscillations automatically.
- VIII To publish the obtained results and conclusions in high-impact journals, as well as in international and national conferences.

## 2.4 Thesis framework

This thesis and the published articles that provide its content as a compendium were developed in the *Department of Automatic Control (ESAII)* of the *Universitat Politècnica de Catalunya (UPC)* under the framework of the brain research line of the *BIOsignal Analysis for Rehabilitation and Therapy Research Group (BIOART)*, which belongs to the *Biomedical Signals and Systems* division of the *Biomedical Engineering Research Centre (CREB)* of UPC that belongs to the Biomedical Research Networking Center in Bioengineering, Biomaterials and Nanomedicine (CIBER-BBN). The research was done with the collaboration of the *Magnetoencephalography* and the *Epilepsy Units* of the *Centro Médico Teknon*. During the course of the thesis, the candidate did a research stay in the *Dynamic Neuroimaging Laboratory* that belongs to the *McConnell Brain Imaging Centre* of the *Montreal Neurological Institute*, a *McGill University* research and training institute.

Furthermore, this work has been supported by multiple funding projects:

1. Ayudas para la contratación de personal investigador novel (FI-DGR 2012). *Agencia de Gestión de Ayudas Universitarias y de Investigación (AGAUR) - Generalitat de Catalunya.*■
2. Ayudas para la formación del profesorado universitario (FPU12/05631). *Ministerio de educación, cultura y deportes (MECD)*
3. Sistemas multicanal de análisis y sensorización para rehabilitación y monitorización clínica. (DPI2011-22680) *Ministerio de Economía, Industria y Competitividad (MINECO)*
4. Design of methods for assessing processes of neurological and neuromuscular decline associated with aging. (DPI201459049R) *Ministerio de Economía, Industria y Competitividad (MINECO)*
5. Biomedical Research Networking Center in Bioengineering, Biomaterials and Nanomedicine,■  
CIBER-BBN, Instituto de Salud Carlos III, Spain.

## Chapter 3

# Automatic BSS-based filtering of metallic interference in MEG recordings

**Published as:** Migliorelli, C., Alonso J.F., Romero S., Mañanas, Nowak R. and Russi A. Automatic BSS-based filtering of metallic interference in MEG recordings: definition and validation using simulated signals *Journal of Neural Engineering* 12(4):046001, 5 2015

doi: 10.1088/1741-2560/12/4/046001

Impact Factor: 3.493; Position 10 of 76 (Q1) BIOMEDICAL ENGINEERING.

**Abstract:** *Objective.* One of the principal drawbacks of magnetoencephalography (MEG) is its high sensitivity to metallic artifacts, which come from implanted intracranial electrodes and dental ferromagnetic prosthesis and produce a high distortion that masks cerebral activity. The aim of this study was to develop an automatic algorithm based on blind source separation (BSS) techniques to remove metallic artifacts from MEG signals. *Approach.* Three methods were evaluated: AMUSE, a second-order technique; and INFOMAX and FastICA, both based on high-order statistics. Simulated signals consisting of real artifact-free data mixed with real metallic artifacts were generated to objectively evaluate the effectiveness of BSS and the subsequent interference reduction. A completely automatic detection of metallic-related components

was proposed, exploiting the known characteristics of the metallic interference: regularity and low frequency content. *Main results.* The automatic procedure was applied to the simulated datasets and the three methods exhibited different performances. Results indicated that AMUSE preserved and consequently recovered more brain activity than INFOMAX and FastICA. Normalized mean squared error for AMUSE decomposition remained below 2%, allowing an effective removal of artifactual components. *Significance.* To date, the performance of automatic artifact reduction has not been evaluated in MEG recordings. The proposed methodology is based on an automatic algorithm that provides an effective interference removal. This approach can be applied to any MEG dataset affected by metallic artifacts as a processing step, allowing further analysis of unusable or poor quality data.

**Keywords:** Magnetoencephalography, metallic artifact, automatic artifact reduction, blind source separation, AMUSE

### 3.1 Introduction

Magnetoencephalography (MEG) is a noninvasive and functional neuroimaging technique used in clinical practice that measures magnetic fields generated by synchronous brain oscillations. MEG has become an important tool in neurological signal processing and functional neuroimaging (Hall et al., 2014; Baillet et al., 2001). During the last decade, an increasing number of studies of language and cognitive functions and brain connectivity have been carried out (Hari and Salmelin, 2012; Sakkalis, 2011). Modern multichannel whole head systems such as MEG are increasingly being used for clinical applications such as the presurgical evaluation of children and adults requiring invasive surgery as a result of refractory epilepsy or brain tumors (Stufflebeam et al., 2009). This evaluation involves mainly the detection of the spatial focus that should be removed through source localization techniques (Stefan et al., 2011). Several studies claim that MEG adds valuable information to the source localization that is not visible with other imaging techniques such as electroencephalography (EEG) or functional Magnetic Resonance Imaging (fMRI) (Stefan et al., 2011; Barkley, 2004; Sharon et al., 2007).

The magnetic activity of the brain is substantially smaller (starting from a few tenths of femtoeslas) than ambient noise and this is the main reason why MEG recordings are performed in



a magnetically shielded room to isolate them from external magnetic fields. However, as with EEG recordings, some artifacts are unavoidable because subjects may be affected by ocular, cardiac, muscular and other interferences (Stufflebeam et al., 2009) that have to be removed or reduced using signal processing techniques before proper analysis of MEG signals can be performed. In this context, Blind Source Separation (BSS) is one of the most commonly used techniques to achieve an effective removal of several kinds of artifacts.

A drawback of MEG is its increased sensitivity to metallic interference that may come from inside the head, such as implanted intracranial electrodes and dental ferromagnetic prosthesis and brackets, or from outside, such as pacemakers and vagal stimulators (Vrba, 2002). To try to minimize the effect of these interferences, an extremely magnetic hygiene inside the shielded room is required (Hillebrand et al., 2013). Recordings have to be performed with subjects trying to avoid any kind of movement, and even a demagnetization of the subject can be carried out. For this reason, MEG signal recording requires very careful preparation that can only be performed by highly trained specialists. Despite all precautions, sometimes it is not possible to eliminate all sources of metallic artifacts and highly distorted recordings are obtained. Typically, these artifacts appear modulated by breathing and cardiac rhythms (Hillebrand et al., 2013) due to the great sensitivity to movement. The amplitude of metallic artifacts is typically much higher than the amplitude of cerebral signals and can even reach values larger than  $10^5$  fT (Cheyne et al., 2007). Metallic artifacts affect the whole record, overlapping brain activity, and may alter all head channels with varying amplitudes. Usually, there are a certain number of channels whose high level of contamination masks cerebral activity almost completely.

The most widely used method for extracting useful information from contaminated recordings is to remove artifactual channels and to apply band-pass filtering, but there are still a large number of cases with unusable signals due to huge artifact contamination. This results in a loss of information that is particularly necessary when artifacts overlap the cerebral region of interest, for example during preparation of surgery. The literature reports few techniques able to eliminate this sort of metallic interference. For sources located outside the head, temporal Signal Space Separation (tSSS) has been used for metallic artifact reduction using generated metallic signals in a phantom experiment (Taulu and Simola, 2006). To do so, it was necessary to previously identify source patterns at the cost of potentially removing true brain signals as

well (Medvedovsky et al., 2009).

BSS techniques have proven effective for automatically removing cardiac, ocular and movement artifacts (Escudero et al., 2007; Mantini et al., 2008) but, to date, there have not been any studies that use BSS to remove metallic artifacts in an automatic fashion. The goal of BSS algorithms is to estimate the different original source signals or components from the observation signals assuming a linear mixture model. This can be done because, although original source signals and the mixing system are unknown, a certain statistical independence between sources is assumed.

The main aim of this study was to develop an automatic algorithm based on BSS techniques to effectively remove metallic artifacts from MEG signals. It was necessary to evaluate objectively and quantitatively the performance of different BSS methods. Consequently, three well-known algorithms were evaluated: AMUSE, a second order method; and INFOMAX and FastICA, both high order statistics. Semi-automatic AMUSE-based filtering was previously evaluated on a very preliminary study with four real MEG signals (Migliorelli et al., 2013) and its main conclusion stated that AMUSE was able to extract components projecting on the areas where metallic artifacts had more energy. However, the objective evaluation of the effectiveness of each artifact reduction process is difficult to assess with real signals because the components belonging either to artifacts or to brain signals are not fully known. To date, BSS has been tested in EEG simulated signals to reduce artifacts from external sources such as ocular interference (Romero et al., 2008, 2009), but it has not been evaluated using simulated MEG data. Therefore, simulated MEG recordings corresponding to clean signals contaminated with real metallic artifacts were generated in this study to evaluate the effectiveness of separation into components and the subsequent artifact reduction. Previous knowledge of the behavior of metallic artifacts was useful to develop a fully automatic method for the selection of source components related to artifacts, which should be subsequently removed to obtain a successful reconstruction of MEG data.

## 3.2 Materials and Methods

### Subjects and instrumentation

Ten subjects with ferromagnetic implants (age  $23.6 \pm 10.4$  years), six of them with an implanted subdural grid and four with dental brackets, and ten subjects without implants or other metallic artifactual sources (age  $36.7 \pm 10.7$  years) were selected for this study. MEG signals were acquired during 10 min with closed eyes using a whole-head 148-channel magnetometer system (4D-Neuroimaging/BTi) and sampled at 678.19 Hz (bandwidth DC to 250 Hz). Signals were imported into MATLAB using the Fieldtrip toolbox (Oostenveld et al., 2011), and two-minute epochs were selected randomly.

Implant-related artifacts contaminated a large number of channels, some of them with a very high amplitude that masked the cerebral activity completely, which could not be extracted using classical filtering techniques. Artifacts were observed to follow regular or periodic patterns that were present with varying intensity to many channels.

#### 3.2.1 Simulated data

In order to simulate real cases of MEG signals affected by metallic interference, a linear mixture between clean signals and metallic artifacts extracted from contaminated signals was proposed, following a scheme analogous to that proposed in (Romero et al., 2008) for the generation of simulated signals affected by ocular artifacts. Ten two-minute epochs were simulated according to the following mixing model:

$$S = C + WP \tag{3.1}$$

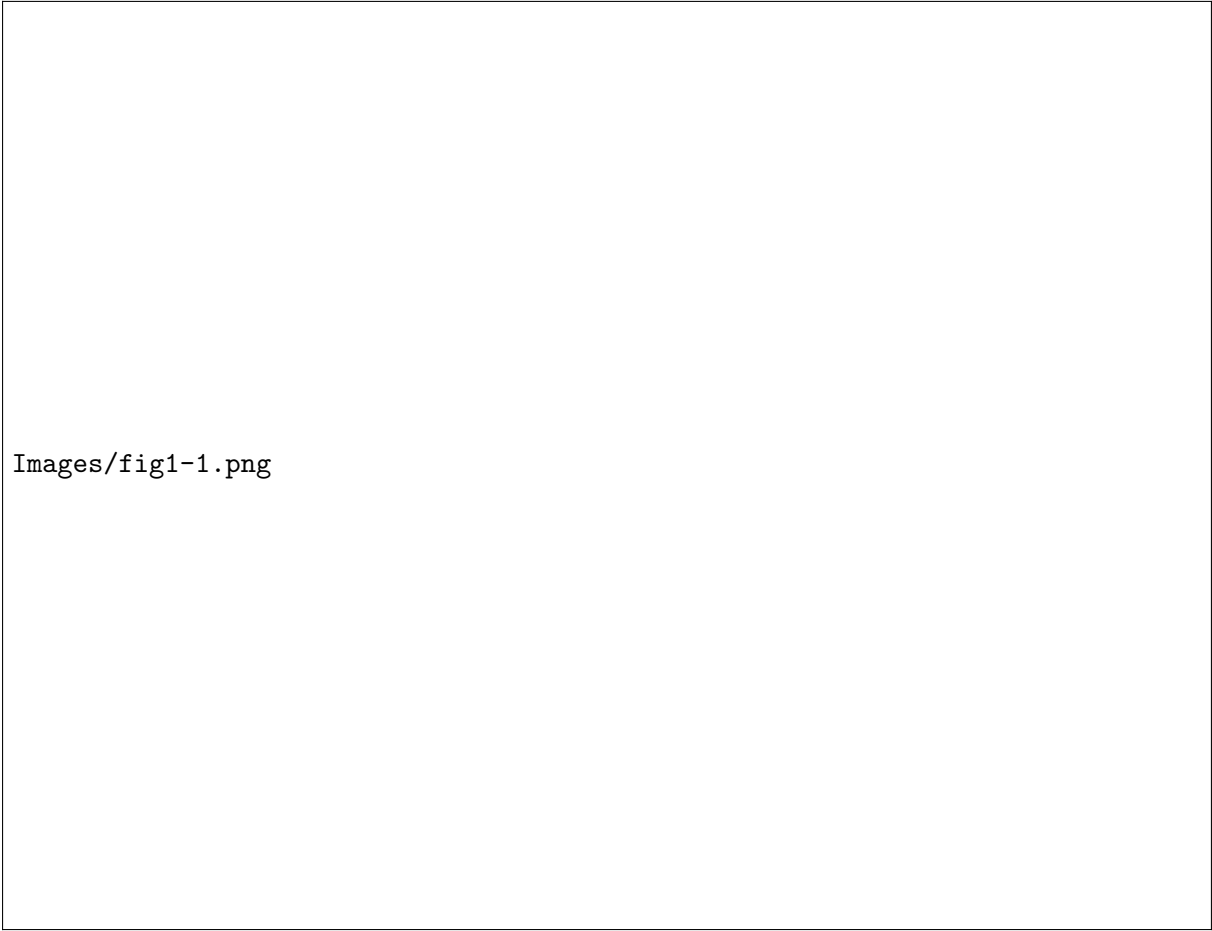
where  $S$  indicates the simulated signals,  $C$  denotes clean MEG recordings,  $W$  corresponds to the mixture weights, and  $P$  represents the different artifactual morphologies selected. These different patterns caused by metallic interference had to be extracted from contaminated recordings and then added to clean signals according to the propagation coefficients obtained by means of an approach based on linear regression.

### Extraction of different metallic artifactual waveforms from contaminated recordings

Most noticeable metallic artifacts are easily identifiable on visual inspection of the signals mainly due to their higher amplitude with respect to the remaining MEG channels, but also to their slower and more regular waveforms, which are usually modulated by the heart or respiratory rates (Hillebrand et al., 2013). In this study, three experts examined the signals and identified channels that clearly and strictly met these criteria of high amplitude, low frequency, regularity, and possible modulation by respiratory or cardiac rhythms. Only those channels selected by all three experts were chosen as artifactual channels and therefore used to obtain the artifactual waveforms. The interobserver agreement was of  $0.829 \pm 0.097$  with a kappa index of  $0.851 \pm 0.095$ , indicating an 'almost perfect' agreement according to the definitions given in (Viera and Garrett, 2005).

In order to extract only the information provided by metallic interference, a low-pass filter with the cutoff frequencies obtained with the cumulative spectra was applied to remove the cerebral activity present in these selected channels ( $7.4 \pm 2.1$  Hz as mean and standard deviation for all channels). The spectra of clean and artifactual signals were similar at high frequencies but they differed at low frequencies due to metallic interference. Considering that this conspicuous difference was due to the presence of the metallic artifact, reverse-cumulative (from high to low frequency) spectra were obtained for each artifactual channel and for the same channel in all artifact-free recordings. Spectra were calculated by means of Welch's periodogram using a five-second Hanning window with 50% overlapping. The difference between the artifactual spectrum and the average of all clean spectra was used to obtain the cutoff frequency for each artifactual channel, searching for the frequency where the normalized difference reached 5% (see figures 3.1(a) and (b)). Subsequently, each selected artifactual channel was filtered with an 8th-order Butterworth filter (figure 3.1(b)).

Metallic interference is known to affect different MEG channels with varying shape and intensity. For this purpose, a selection of the different waveforms spreading over the scalp had to be performed. Consequently, the cross-correlation between artifactual channels was obtained, and only low-correlated waveforms (coefficient  $< 0.5$ ) were preserved. Among those showing high correlation ( $\geq 0.5$ ), only the signal with the highest energy was maintained (see figure 3.1(c)).



Images/fig1-1.png

Figure 3.1: Scheme for generation of a simulated artifactual MEG recording: (a) five-second epoch of raw MEG with metallic artifacts (only 16 selected channels are drawn). Orange traces correspond to the highly artifactual channels selected by the experts; (b) low-pass filtered artifactual channels (cutoff frequency automatically calculated from reverse-cumulative spectra); (c) selected morphologies (orange traces) after correlation among channels in (b), and their corresponding linear regression coefficients (whole head maps); (d) propagation of artifacts corresponding to coefficients obtained in (c); (e) five-second epochs of raw artifact-free MEG channels; and (f) simulated signals obtained by summation of (d) and (e).

In this way, only those morphologies that were different enough were selected as artifactual patterns (figure 3.1(d)).

### Calculation of propagation coefficients by linear regression and generation of simulated data

Propagation coefficients represented the amount of metallic interference that was present in a particular MEG channel with respect to a specific artifactual pattern. Linear regression between all channels of the actual artifactual recordings and each selected pattern was performed, taking

into account the entire two-minute recordings. The obtained regression coefficients (represented as topographic maps in figure 3.1 (c)) were used as weights of the mixing matrix  $\mathbf{W}$  (equation 3.1) and then patterns were propagated to all channels (figure 3.1(d)). Finally, the simulated artifacts were added to clean recordings (figure 3.1(e)) to obtain a set of simulated artifactual signals (figure 3.1(f)). These steps were performed 10 times to obtain 10 sets of simulated MEG signals with known metallic interference.

### 3.2.2 Blind source separation approaches to artifact reduction

BSS techniques estimate source signals from a set of mixed signals, separating MEG signals into spatial components to later reconstruct the brain signal discarding the components associated with artifacts. The model of the identification process is expressed by:

$$x(t) = As(t) \quad (3.2)$$

where  $x(t)$  is the observation signal vector and  $s(t)$  the unknown source signal vector with  $n$  and  $m$  rows respectively.  $A$  is the  $n \times m$  mixing matrix which should be estimated and represents the weights of the projection of the corresponding source signals at different channels.

Usually, BSS methods can be classified according to the order of the statistic used to perform the separation. Methods based on second order statistics (SOS) assume sources that are only uncorrelated. One of the techniques used in this study is the Algorithm for Multiple Unknown Signals Extraction (AMUSE) (Tong et al., 1991), which exploits SOS through a first step of signal whitening and a second step of an eigenvalue decomposition. AMUSE is sometimes classified as an independent component analysis (ICA) technique because decorrelation can be considered as a weak form of statistical independence (Hyvärinen et al., 2001). However, SOS are effectively enough to separate and remove those Independent Components (IC) corresponding to various types of artifacts (Escudero et al., 2010).

While SOS-based algorithms provide independence in terms of correlation, in the case of higher order statistics (HOS) a more general concept is considered: two random variables are independent when the statistical behavior of one of them is not affected by the values taken by the other.

Statistical independence can be estimated using several different methods based on mutual information, non-gaussianity or maximum likelihood, for example. Additionally to AMUSE, two HOS-based techniques, INFOMAX and FastICA, were used in this work. Both algorithms are iterative and require proper initialization and parameter setting.

On the one hand, INFOMAX maximizes the joint entropy of a neural processor output, based on the fact that the maximum entropy of joint variables only occurs when they are statistically independent (Bell and Sejnowski, 1995). In this study, separation by means of an extended version of INFOMAX was performed using the default parameters proposed in the EEGLAB toolbox for MATLAB (Delorme and Makeig, 2004; Lee et al., 1999)

On the other hand, FastICA is based on a fixed-point iterative scheme that maximizes non-gaussianity as a measure of statistical independence between sources. A weight matrix is obtained after a certain number of iterations, but non-gaussianity of the independent components is necessary for a successful convergence of the algorithm (Hyvärinen, 1999). However, the step size can be adjusted through a stabilization parameter so that convergence can be achieved in unfavorable conditions.

Automatic selection of metallic-related components For all three algorithms evaluated, a decomposition scheme that provided as many ICs as available MEG channels was used (148). Once the components were estimated, it was necessary to design an automatic selection procedure to detect those components related to metallic artifacts, taking into account their known features: low frequency and regular behavior, especially modulated by the heart and breathing rhythms. Two criteria were considered to identify the extracted independent components related to metallic artifacts (figure 3.2(a)):

- (i) The frequency below which the spectrum holds most of the energy of the signal. If the spectral content is located principally at low frequencies, it is more likely that the component corresponds to metallic interference.
- (ii) The regularity of the signal, as measured by the sample entropy (Richman and Moorman, 2000). This criterion was directly associated with the typical modulation of metallic artifacts, which makes them more regular than cerebral activity.

Images/fig1-2.png

Figure 3.2: Automatic artifact-related component selection: (a) frequency and entropy estimation (for all extracted ICs) and thresholds (blue dashed lines). (b) Artifactual area selected by the union of the regions of interest of the selected ICs. (c) As an example, evaluation of the projection of ICs 3 and 4 is shown. Regions of interest are indicated with dark blue shading. IC 3 is outside the artifactual area and therefore would not be selected by the automatic algorithm, whereas IC 4 would, as its region of interest is inside the artifactual area and the weak criteria concerning frequency and entropy are met.

The procedure carried out in order to select the artifactual components was based on two steps: the selection of the artifactual region and a comparison of this region with the projection of each IC.

The purpose of the first step was to locate the artifactual area that, due to the particular origin of metallic artifacts, could be located anywhere on the scalp. In this first step, those components which simultaneously met the two above-mentioned criteria were selected as artifactual components (figure 3.2(b)) and used to identify the area of the scalp where the artifact was located. A strong version of the criteria was applied, and only ICs with 90% of the energy in the slowest frequency bands delta and theta (up to 7.5 Hz) and high regularity (sample entropy lower than 0.3, obtained with an embedding dimension of 3 and a search radius of 0.1 times the standard deviation of the signal) were selected.

A region of interest was defined for each selected component, taking into account the BSS weights normalized with respect to the maximum for each channel and discarding the lowest quartile. The final artifactual region was defined as the union of the regions of each component. The purpose of this selection was to define a region where the artifact projected and to prevent artifactual regions being focused on only a few high-energy channels.



The second step involved the comparison between the artifactual region and the region of interest of every IC (figure 3.2(c)). When this region of interest was included in the artifactual region and an IC fulfilled a weak version of the aforementioned criteria (90% of energy below 15 Hz, sample entropy lower than 0.5), then the IC under evaluation was marked as an artifactual component. This second step was performed in order to ensure the selection of artifactual components that displayed characteristics highly related to metallic interference and were focused on the defined artifactual region. To achieve an effective removal of metallic interference, all marked ICs had to be removed, and the resulting artifact-free signal was obtained as the product of the remaining components by the weight matrix obtained by the algorithm.

### 3.2.3 Performance assessment

In order to assess the performance of the metallic artifact removal methodology, several error measurements based on time and frequency domain were calculated for each channel and each simulated recording.

- (i) The normalized mean squared error (nMSE),

$$NMSE_n = 100 \cdot \frac{\sum_i^N (x_n(i) - y_n(i))^2}{\sum_i^N y_n(i)^2} \quad (3.3)$$

- (ii) The variation of absolute power in the delta band (0.5 to 4 Hz) was obtained to study the error in the band most affected by metallic artifacts.

$$\Delta\delta = 100 \cdot \frac{\delta_x - \delta_y}{\delta_y} \quad (3.4)$$

where  $\delta_x$  and  $\delta_y$  represent the power of the  $\delta$  band of the filtered MEG channel under evaluation and of the original clean signal respectively.

- (iii) The variation of absolute power in the alpha band (7.5 to 13 Hz) was also calculated in order to observe the error made in a band where metallic artifacts should have little influence, and therefore errors should be lower.

$$\Delta\alpha = 100 \cdot \frac{\alpha_x - \alpha_y}{\alpha_y} \quad (3.5)$$

where  $\alpha_x$  and  $\alpha_y$  represent the power in the  $\alpha$  band of the signal under evaluation and of the original clean signal respectively.

## 3.3 Results

### 3.3.1 Simulated data

Ten simulated datasets were generated following the steps explained in figure 3.1. The number of channels containing visible metallic interference selected by the experts was  $6.6 \pm 4.4$ , and, in general, artifacts contaminated channels with varying amplitudes. While in some subjects the high amplitude of the artifacts affected many channels, there were other cases where high amplitudes focused on a reduced number of channels. In spite of the dispersion shown by the location of the artifact, their associated signals showed low frequency and regular pattern characteristics, modulated by cardiac and respiratory rates.

Once the different waveforms (patterns) were obtained, and after proper filtering and correlation procedures explained in the previous sections, propagation to the whole head was performed by means of linear regression. Figure 3.3 shows the propagation coefficients normalized with respect to the maximum obtained after regression. It is noticeable that metallic artifacts affected different areas of the scalp depending on the subject, and while in some cases artifacts were focused at specific regions, in others they appeared more dispersed and covered a larger area of the head.

### 3.3.2 Blind source separation and automatic detection

Separation of ICs was performed with AMUSE, INFOMAX and FastICA for the ten simulated subjects. AMUSE and INFOMAX algorithms successfully extracted ICs from the mixed signals in which artifact-related source components were visually identifiable. Subgaussianity of the

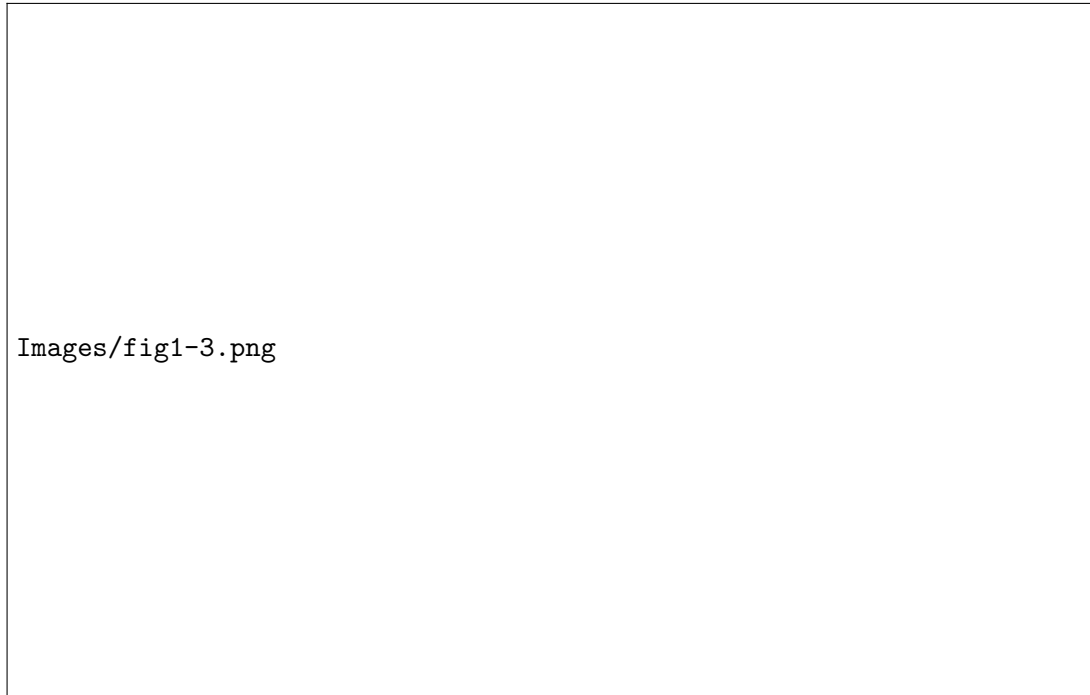


Figure 3.3: Sum of the linear regression coefficients normalized with respect to its maximum for all of the selected artifactual patterns for the 10 simulated MEG sets. Coefficients were obtained for the whole head after morphology selection and linear regression of each channel with the selected morphologies. Note that metallic artifacts behave differently depending on their nature and therefore they can appear in different areas of the head for each simulated MEG set.

data, especially related to metallic artifacts, caused a non-effective decomposition in the case of the FastICA algorithm, which could not separate ICs related to brain signals from metallic artifacts even after using the stabilization parameters to ensure convergence.

The automatic detection procedure was applied to the obtained ICs to detect which components were associated with the metallic interference and therefore were to be discarded to obtain a successful removal of metallic artifacts.

Figure 3.4(a) shows, as an example, an artifact-free subject signal; and figure 3.4(b) shows the simulated signals obtained after the addition of artifactual waveforms to the same subject. Figure 3.5 shows the results, in time domain, of the artifact reduction process on simulated signals shown in figure 3.4. Figures 3.5(a), (b) and (c) show the extracted ICs for AMUSE, INFOMAX and FastICA respectively, with the selected ICs displayed in a different color. The resulting signals obtained after reconstruction without considering the ICs associated with metallic interference are shown in figures 3.5(d), (e) and (f). It is noticeable that the automatic algorithm

procedure was not able to identify any metallic-related ICs in the FastICA decomposition, and this led to a full reconstruction of the signal with the original metallic interference. Visual inspection of the extracted components and the reconstructed signals indicated that INFOMAX was not completely successful in separating brain-related activity from artifactual waveforms, but AMUSE was indeed able to separate metallic interference from MEG activity. INFOMAX provided components related to artifactual activity mixed with cerebral waveforms and the effects of such a decomposition were remarkable after signal reconstruction (figure 3.5(e)), especially when compared to AMUSE (figure 3.5(d)), which showed much more similar signals compared to the clean set (figure 3.4(a)).

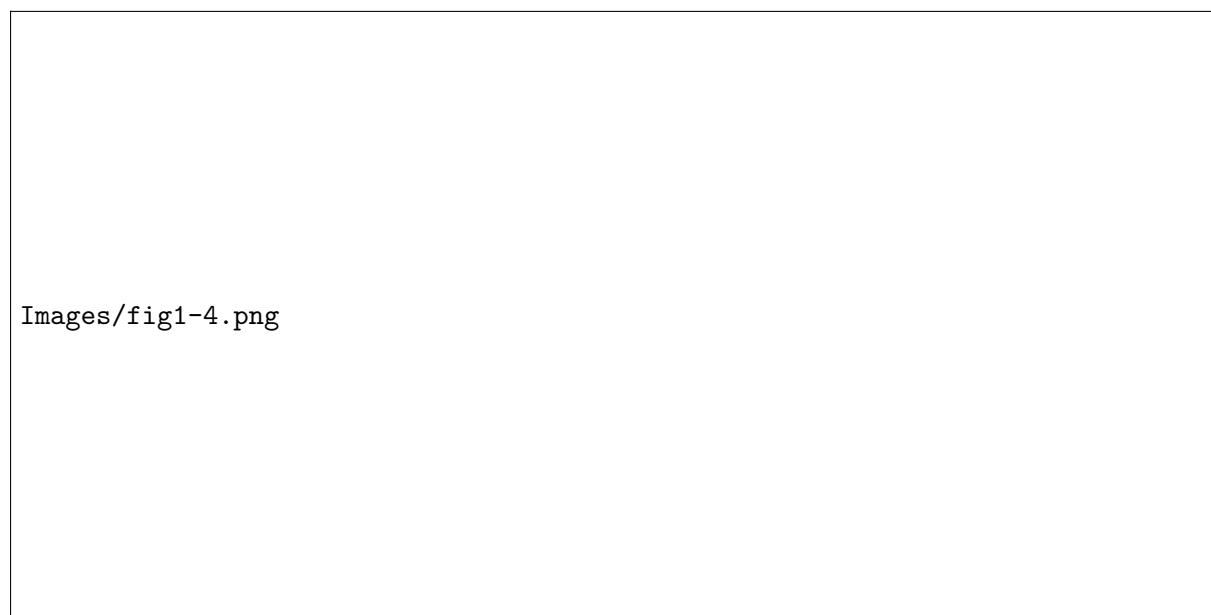


Figure 3.4: MEG channels (16 distributed evenly on the scalp) for: (a) control subject, that is, clean recording, free of metallic artifacts; (b) simulated subject. Orange traces indicate channels originally selected as artifacts by the experts.

### 3.3.3 Performance assessment

Figure 3.6 shows the percentage error in several subjects as an example, represented as whole-head topographic maps. These errors were calculated for three conditions: simulated signals without correction, to observe the amount of artifact introduced; and after applying AMUSE- and INFOMAX-based artifact filtering. Metallic contamination was mainly present in the area of high-energy artifacts, while the distortion of the remaining channels was considerably lower.

Images/fig1-5.png

Figure 3.5: Artifact-reduction for a simulated subject: (a), (b) and (c) show the first 20 extracted ICs corresponding to AMUSE, INFOMAX and FastICA algorithms, respectively. Note that the first 2 ICs (orange traces) obtained by AMUSE and INFOMAX were automatically selected and removed to perform signal reconstruction, whose results are shown in (d) and (e), respectively. FastICA was not able to extract useful artifact-related components and the reconstruction shown in (f) does not remove any amount of artifact (and, consequently, the reconstructed signals equal those of figure 3.4(b)).

For this reason the amount of error observed for the uncorrected case always showed a maximum error value in the artifactual region. As expected, errors in the delta frequency band after filtering were higher than in the alpha band because of the characteristics of metallic contamination, and INFOMAX showed higher errors than AMUSE.

As explained in the previous sections, metallic contamination masked the cerebral activity of some channels in real cases. This situation was reproduced in the simulated MEG subjects and, in fact, the energy introduced by metallic artifacts in MEG activity was huge in many cases (see values and average in table 3.1). After applying INFOMAX-based correction, this error was reduced but still high, whereas after AMUSE-based filtering this error was lower than 1%.

Images/fig1-6.png

Figure 3.6: Error percentage for normalized MSE, delta power and alpha power, shown for three different simulated subjects as examples. Errors are shown for non-corrected, AMUSE-corrected and INFOMAX-corrected signals. Due to the frequency content of metallic artifacts, errors are expected to be lower in the alpha band and higher in the delta band, focusing especially on the areas where the artifact is located. Note that AMUSE-based reconstruction shows the lowest errors for the three measures.

Table 3.1: Error percentage for nMSE, delta power and alpha power (average of all channels) for non-corrected signals, AMUSE-corrected signals and INFOMAX-corrected signals.

Subj.	nMSE			Delta error (%)			Alpha Error (%)		
	Non-corrected	Amuse	Infomax	Non-corrected	Amuse	Infomax	Non-corrected	Amuse	Infomax
1	521.70	0.12	414.10	2464.23	0.52	2226.07	2.12	0.31	3.99
2	7811.33	0.33	173.02	44500.04	0.42	214.46	1.30	0.88	121.7
3	43.94	0.02	48.02	84.01	0.15	83.93	0.02	0.07	2.15
4	20926.17	1.51	3622.56	64421.30	2.50	12293.77	0.97	2.52	475.44
5	219.99	0.02	19.68	1568.38	0.13	131.80	0.01	0.06	2.06
6	3754.65	0.21	50.55	14169.41	0.48	66.97	32.76	0.62	42.49
7	9061.74	0.57	3417.17	59869.96	0.80	9964.57	0.01	0.44	1665.48
8	8379.42	0.19	135.58	43106.98	0.22	174.84	0.01	0.12	114.64
9	3795.21	0.13	45.05	14018.33	0.64	39.15	121.08	0.52	38.35
10	3764.70	0.59	205.70	14720.35	1.33	308.99	148.16	2.01	102.39
<b>Mean</b>	<b>5827.89</b>	<b>0.37</b>	<b>813.14</b>	<b>25892.30</b>	<b>0.72</b>	<b>2550.45</b>	<b>30.64</b>	<b>0.75</b>	<b>256.87</b>

The variability in amplitude and energy of metallic artifacts caused the amount of error introduced to be very inhomogeneous. As can be observed in figure 3.6, INFOMAX was not an appropriate method to remove the interference because of the large amount of error obtained: the error provided in the alpha band, sometimes higher than without correction, suggested that INFOMAX ICs associated with artifacts were a mixture of metallic and cerebral signals,

and possibly some brain-related activity was being deleted. On the contrary, AMUSE always provided low alpha power errors, below 3%.

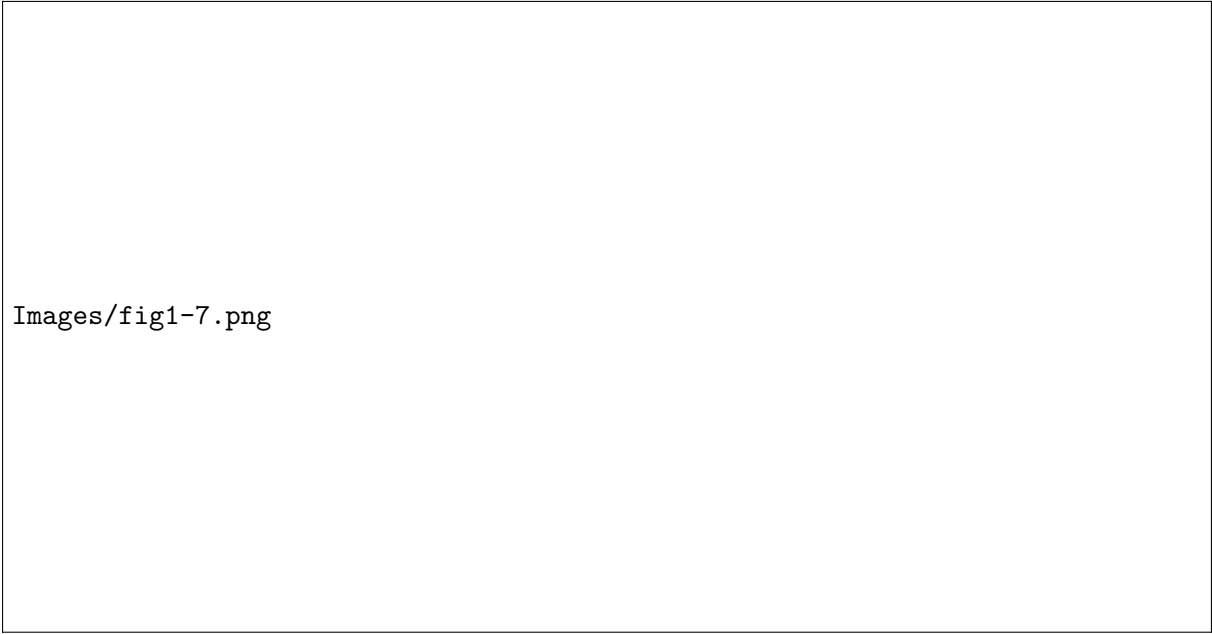
### 3.3.4 Real data

Once the effectiveness of the automatic BSS-based procedure has been measured using simulated signals, assessment of its performance with real MEG data is pertinent. Real spontaneous MEG signals with eyes closed corresponding to the 10 subjects with ferromagnetic implants described in the 'Materials and Methods' section were used for this purpose. One way to demonstrate the filtering performance is to show that alpha-band oscillations with eyes closed can be better detected after artifact removal.

Figure 3.7(a) shows as an example a five-second epoch corresponding to a subject with a metallic subdural grid affecting the posterior region of the scalp where a high interference is clearly noticeable. The AMUSE algorithm, which has been shown to be the most effective and efficient technique in the simulated database, was used for the BSS decomposition. After applying the filtering procedure (see figure fig:1-7(b)), alpha waves could be easily recognized by visual inspection. Moreover, topographic maps of the average alpha power of the 10 subjects with metallic implants before and after applying the automatic procedure are shown in figure fig:1-8. Although metallic artifacts mainly affected the delta and theta bands, the alpha-band is also significantly affected, as shown in figure fig:1-8(a) where alpha power is scattered over the scalp due to metallic interference. Once the BSS-based artifact reduction procedure was applied, the map shows a physiologically more plausible distribution of alpha power mainly focused on the posterior region, as expected.

## 3.4 Discussion

Metallic artifacts in MEG recordings are an important issue in the diagnosis of neurobiological events because they can hugely distort MEG signals and render many single-channel signals unusable. This leads to an unavoidable loss of information regarding the activity of the brain, or even worse, to a rejection of the MEG technique as a mean to obtain reliable cerebral signals



Images/fig1-7.png

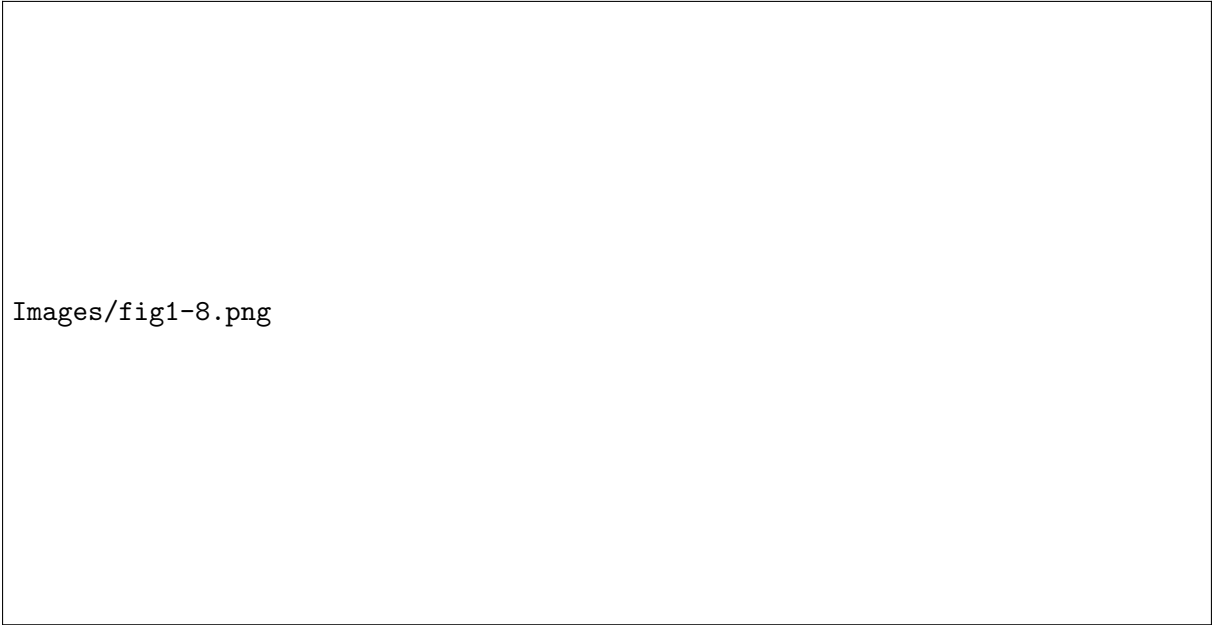
Figure 3.7: (a) Five-second epoch of raw MEG signals containing prominent metallic interference. Posterior channels are shown as an example. (b) Corrected MEG signals obtained after applying automatic AMUSE-based metallic removal procedure.

of those patients who have metallic elements that could generate such interferences.

Signal space separation (SSS) (Taulu et al., 2004) and temporal SSS (tSSS) (Taulu and Simola, 2006) are also methods for MEG filtering. Applying SSS or tSSS is highly advised for Elekta-Neuromag systems (Gonzalez-Moreno et al., 2014) and their algorithms are provided by a software registered and available only on this equipment. On the other hand, the filtering approach presented in this paper is based on BSS standard libraries which are freely available and could be used with signals from different MEG systems such as CTF/VSM, 4D Neuroimaging, Elekta and Yokogawa.

The tSSS algorithm was applied efficiently to remove MEG artifacts in several studies (Gonzalez-Moreno et al., 2014; Nenonen et al., 2012; Taulu and Hari, 2009) and in particular, in the case of metallic interferences: (Hillebrand et al., 2013; Cheyne et al., 2007; Taulu and Simola, 2006). These studies showed the improvement of dipole fitting procedures when tSSS is applied instead of SSS but they did not evaluate the noise reduction of metallic interference or measure it quantitatively. Furthermore, there are no comparative studies of this technique with other artifact reduction algorithms such as BSS or epoch rejection.





Images/fig1-8.png

Figure 3.8: (a) Topographic distribution of the average alpha power of the 10 artifactual subjects. (b) Average of alpha power obtained after applying automatic AMUSE-based metallic removal procedure.

In (Gonzalez-Moreno et al., 2014) an interesting SNR analysis was carried out when SSS and tSSS were first applied followed by the BSS or epoch-rejection procedure. This study concluded that SNR increased by 100% after applying SSS or tSSS techniques. Moreover, the SNR improved an additional 33–36% when BSS methods were subsequently applied. The latter suggests that not all noise was successfully removed by the tSSS method and BSS algorithms could remove interferences that remained after applying tSSS techniques. In addition, these studies also concluded that one of the main drawbacks of BSS-based noise-reduction techniques is the need for manual selection of noisy or artifactual components, which is done visually. However, our study describes an automatic approach to detect artifactual components.

As the location and intensity of metallic artifacts usually varies among different subjects, it is not possible to make feasible *a priori* assumptions on these characteristics to adjust an automatic detection algorithm. In this work, a new BSS-based automatic procedure using freely available standard libraries was presented to identify components related to metallic activity, whose performance was tested using simulated MEG signals, which are essential to objectively quantify the effectiveness of the method while reproducing standard clinical situations as faithfully as possible.

One of the main questions arising when working with BSS is the estimation of the number of independent components (ICs) to be extracted. At most, it is possible to extract as many ICs as there are channels that the record is composed of, but when this number is high it is usually advisable to reduce it and usually a lower number of ICs is obtained. The search for the optimal number allows one to avoid over- and under-fitting phenomena (Li et al., 2007), and is often achieved by selecting the ICs that can explain a high percentage of the variance of the signals. Due to the high amount of energy accounted for by metallic artifacts, the reduction of the number of ICs was not appropriate when dealing with this kind of interference. The energy of the artifacts was much greater than that of cerebral signals (around four orders of magnitude in some cases) and consequently the number of ICs corresponding to very high percentages of the total variance resulted in being very low. Thus, it was not possible to achieve a successful separation between cerebral activity and metallic interferences. For this reason, all BSS algorithms were forced to extract as many components as available channels.

One Second-Order Statistics (SOS) and two Higher-Order Statistics (HOS) techniques were tested. The SOS-based algorithm, AMUSE, showed considerably lower errors and therefore a valid decomposition. In the case of HOS, two algorithms were tested, INFOMAX and FastICA. While the first one was successful in separating ICs related to brain activity from those of metallic interference, the second did not manage to generate a valid decomposition. FastICA is an algorithm that uses the kurtosis to evaluate the gaussianity in order to separate independent components. This algorithm is very effective in dealing with supergaussian sources such as cardiac and ocular interferences (kurtosis higher than 3), but its principal drawback is poor convergence when working with gaussian and subgaussian signals, which is the case for metallic interferences that, in general, present a kurtosis value close to 3. Even after ensuring convergence by means of the stabilizer provided by (Hyvärinen, 1999), the decomposition was not effective and no metallic-related components could be identified.

On the other hand, the extended version of INFOMAX was able to work with subgaussian signals, and effective convergence and IC separation were achieved. However, the algorithm was not able to separate metallic components as accurately as AMUSE, and part of the cerebral signals remained, mixed with metallic components. That is the main reason why some of the error measures increased significantly when INFOMAX was applied.

After source decomposition, a simple two-step procedure for metallic-related component identification was applied. This simple scheme, based on two criteria which exploited the basic characteristics of metallic artifacts (low frequency and regularity), allowed the delimitation of an artifactual region. Once this region was obtained, all possible ICs that exhibited artifactual behavior were identified and removed from the reconstruction matrix.

This artifact-filtering methodology was tested on 10 sets of simulated MEG signals consisting of clean recordings to which metallic artifacts were added. The extraction of these artifacts from real signals was performed taking into account the different morphologies and varying propagation of this contamination by means of filtering, correlation and estimation of propagation coefficients by linear regression.

Results showed that the two-step automatic detection methodology was able to detect ICs related to metallic interference especially when they were extracted through the AMUSE algorithm. Normalized MSE error showed an average value of 0.37% (see table 3.1). Errors in delta power were lower than 1% in average, showing a great performance in the most affected spectral band.

It is notable that these error measures presented very low values when compared to non-corrected sets of signals. However, there were some cases in which alpha power showed a slightly higher error (worst case subject 4, 1.55% in excess) but this amount can be considered negligible with respect to the general improvement achieved.

Moreover, the performance of the automatic BSS reduction method was assessed in real MEG signals. Results showed that even high-amplitude metallic interference was properly removed from the MEG data. A study based on the alpha activity confirmed that the BSS-based procedure was able to reduce the metallic artifacts and show a more plausible topographic distribution of alpha-band signal after filtering.

Therefore, after applying the fully automated BSS procedure in simulated and real artifactual MEG data, it can be concluded that AMUSE is the most suitable technique to be used along with the two-step algorithm presented in this study for effectively removing metallic interference from MEG signals.

### **3.5 Acknowledgments**

CIBER-BBN is an initiative of the Instituto de Salud Carlos III, Spain. This work has been partially supported by the Ministry of Economy and Competitiveness (MINECO), Spain, under contracts DPI2011-22680 and DPI2014-59049-R and the Ministry of Education, Culture and Sports (MECO) FPU12/05631.

## Chapter 4

# Influence of metallic artifact filtering on MEG signals for source localization during interictal epileptiform activity.

**Published as:** Migliorelli, C., Alonso J.F., Romero S., Mañanas, Nowak R. and Russi A. Influence of metallic artifact filtering on MEG signals for source localization during interictal epileptiform activity. *Journal of Neural Engineering* 13(2):026029, 2016

doi:10.1088/1741-2560/13/2/026029

Impact Factor: 3.493; Position 10 of 76 (Q1) BIOMEDICAL ENGINEERING.

**Abstract:** *Objective.* Medical intractable epilepsy is a common condition that affects 40% of epileptic patients that generally have to undergo resective surgery. Magnetoencephalography (MEG) has been increasingly used to identify the epileptogenic foci through equivalent current dipole (ECD) modeling, one of the most accepted methods to obtain an accurate localization of interictal epileptiform discharges (IEDs). Modeling requires that MEG signals are adequately preprocessed to reduce interferences, a task that has been greatly improved by the use of blind source separation (BSS) methods. MEG recordings are highly sensitive to metallic interferences

originated inside the head by implanted intracranial electrodes, dental prosthesis, etc and also coming from external sources such as pacemakers or vagal stimulators. To reduce these artifacts, a BSS-based fully automatic procedure was recently developed and validated, showing an effective reduction of metallic artifacts in simulated and real signals (Migliorelli et al., 2015). The main objective of this study was to evaluate its effects in the detection of IEDs and ECD modeling of patients with focal epilepsy and metallic interference. *Approach.* A comparison between the resulting positions of ECDs was performed: without removing metallic interference; rejecting only channels with large metallic artifacts; and after BSS-based reduction. Measures of dispersion and distance of ECDs were defined to analyze the results. *Main results.* The relationship between the artifact-to-signal ratio and ECD fitting showed that higher values of metallic interference produced highly scattered dipoles. Results revealed a significant reduction on dispersion using the BSS-based reduction procedure, yielding feasible locations of ECDs in contrast to the other two approaches. *Significance.* The automatic BSS-based method can be applied to MEG datasets affected by metallic artifacts as a processing step to improve the localization of epileptic foci.

**Keywords:** magnetoencephalography, metallic artifact, automatic artifact reduction, blind source separation, epilepsy, IEDs

## 4.1 Introduction

Epilepsy is one of the most common neurological disorders affecting about one percent of the world population (Ramey et al., 2013). Its main therapeutic option relies on pharmacological treatment with antiepileptic drugs, which produce a seizure-free outcome for approximately 60% of patients (Schuele and Lüders, 2008). For the remaining 40% of patients with focal refractory epilepsy, the most frequent therapeutic alternative is resective surgery of the epileptogenic area, which has demonstrated high rates of success (Ramey et al., 2013).

An accurate localization of epileptic foci is necessary to minimize risk for surgical candidates. Frequently, invasive techniques such as subdural electrodes and depth electrodes are required to identify the epileptic focus. Over the last years, modern noninvasive whole-head systems based on magnetoencephalography (MEG) or electroencephalography (EEG) have been increasingly

used to identify epileptogenic foci in children and adults requiring surgery (Stufflebeam et al., 2009). As a result of their high spatiotemporal resolution, MEG and EEG are able to track transient neural events that can be used to perform the source analysis which estimates the generators of electromagnetic activity inside the brain (Gross et al., 2013). Intracranial recordings are still the gold standard Panzica et al. (2013) for the epileptogenic zone identification, but even in this case, the evaluation with non-invasive techniques is crucial to determine the region where the electrodes will be implanted. For epilepsy studies, the identification of interictal epileptiform discharges (IEDs) is most commonly used for this purpose (Bagić et al., 2011; Bouet et al., 2012). The main advantage of MEG over EEG is that magnetic fields measured by MEG are much less influenced by the electrical conductivity of the tissues surrounding the cerebral cortex than electrical fields (Shibasaki et al., 2007). Both techniques can be considered complementary, and the detection of IEDs improves substantially when used simultaneously (Lin et al., 2003; Patarraia et al., 2005; Knake et al., 2006), although MEG has showed superior performance than EEG when localizing IEDs sources (Amo et al., 2003; Stefan et al., 2004; Ramantani et al., 2006)

In clinical applications, one of the most accepted methods for obtaining an accurate localization of IEDs onset zone is the equivalent current dipole (ECD) model (Anderson et al., 2014) that assumes that cortical activity captured by MEG signals is generated by a single dipolar source. This technique provides excellent clinical models whenever is reasonable to assume that the MEG field pattern arises from a single dipolar source (Lütkenhöner, 1998), as happens with focal epilepsy. Its accuracy for epileptic foci localization has been validated in several studies (Stefan et al., 2003; Fischer et al., 2005; Oishi et al., 2006).

Prior to ECD modeling of MEG or EEG data, signals must be adequately preprocessed to reduce biological and environmental interferences so that enough IEDs can be detected in spontaneous data (Bagić et al., 2011). After that, it is possible to adjust an equivalent dipole to cerebral activity reliably and with high goodness of fit and low confidence volume. Interferences may come from different sources such as cardiac, ocular, or muscular activity (Stufflebeam et al., 2009). Among the different possible methods of filtering, blind source separation (BSS) techniques have proven very effective for the reduction of many kinds of artifacts. Several studies have demonstrated the improvement of source localizations using BSS-based filtering approaches to remove cardiac, ocular or muscular artifacts (Mantini et al., 2008; Fatima et al., 2013). MEG recordings

are also highly sensitive to metallic interferences originated inside the head, such as implanted intracranial electrodes, dental ferromagnetic prosthesis, and brackets; and also coming from external sources such as pacemakers, vagal stimulators (Vrba, 2002) or deep brain stimulation (Airaksinen et al., 2011). Although an extremely magnetic hygiene inside the shielded recording room is required (Hillebrand et al., 2013), often it is not possible to eliminate all sources of metallic contamination and highly distorted data are then obtained. These artifacts appear modulated by breathing and cardiac rhythms and affect the whole record, overlapping the brain activity. In addition, there are usually a number of channels, grouped in one or more areas of the scalp, with a very high level of contamination and whose cerebral activity is masked almost completely (Migliorelli et al., 2015).

Modeling ECDs from IEDs with such metallic artifacts is not always possible due to the high distortion of the data. Worse still, patients whose recordings are highly affected by this interference have to be excluded from analysis. If not excluded, a reliable dipole localization can only be achieved by selecting subsets of channels associated with the dipolar field and rejecting those with high metallic interference (Bagić et al., 2011). However, this reduction of the number of channels close to the epileptic region has several disadvantages: firstly, an inappropriate channel selection can lead to an incorrect source estimation due to the loss of valuable information (Bagić et al., 2011); secondly, removing the most artifacted channels does not necessarily mean that metallic interference has been cleaned, since it can also be present in the rest of the record; and thirdly, if high levels of metallic artifacts are present, IEDs may stay masked behind them, rendering visual identification very difficult or impossible at all. To overcome these limitations, a fully automatic procedure for reducing metallic interference from spontaneous MEG signals based on BSS recently showed an effective reduction of metallic artifacts in simulated and real signals (Migliorelli et al., 2015).

Signal space separation and temporal signal space separation (tSSS) algorithms (Taulu and Simola, 2006) have proven its efficiency removing MEG artifacts in several studies (Song et al., 2009; Kakisaka et al., 2012; Jin et al., 2013; Wang et al., 2013). However, these algorithms are only available, specifically designed and mandatory for Elekta-Neuromag systems (Gonzalez-Moreno et al., 2014). On the other hand, the filtering approach presented in (Migliorelli et al., 2015) is based on standard libraries which are freely available and can be used with signals from



different MEG systems such as CTF/VSM, 4D Neuroimaging, Elekta and Yokogawa.

The main objective of the present study was to evaluate the effects of this automatic filtering procedure in the detection of IEDs and EDC modeling of patients with focal epilepsy and metallic interference, assessing the hypothesized improvement due to metallic artifact reduction. A comparative study of the resulting positions of ECDs was performed for three cases: considering the acquired data without removing metallic interference; rejecting only channels with large metallic artifacts; and after BSS-based reduction of metallic artifacts. To analyze the results obtained for each situation, measures of dispersion and distance of EDCs were defined.

## 4.2 Materials and methods

### 4.2.1 Patients, acquisition settings and previous preprocessing

14 patients diagnosed with intractable epilepsy (age  $15.34 \pm 10.66$  years, mean and standard deviation) were selected for this study. All of them had some kind of nonremovable device that produced metallic interferences: eight patients had dental orthodontics, four an implanted subdural grid, one a vagus nerve stimulator, and one ventricular bypass valve. All patients selected for this study presented interictal activity coming from one focal generator. Table 4.1 show the summary of the data of all 14 subjects.

MEG signals were acquired in a magnetically shielded room during 10 min with eyes closed using a whole-head 148-channel magnetometer system (4D-Neuroimaging/BTi, San Diego, California, USA) and sampled at 678.19 Hz (bandwidth DC to 250 Hz). A 19-channel EEG was simultaneously recorded using a Neurofax amplifier (Nihon-Kohden Co., Tokyo, Japan), with sampling rate set to 512 Hz (bandwidth 3–70 Hz). The relative position of the patient’s head with respect to the MEG sensors was recorded continuously using head-localization coils.

Signals were imported into MATLAB using the Fieldtrip toolbox (Oostenveld et al., 2011) and processed with an 8th order bandpass Butterworth filter with cutoff frequencies set to 3 and 70 Hz as recommended by the clinical practice guidelines (Bagić et al., 2011).

Table 4.1: Summary of all patients. Age, type of epilepsy, type of metallic artifacts.

Subject	Age	Type of epilepsy	Type of metallic artifacts
1	10	PLE	Dental
2	34	TLE	Dental
3	31	TLE	Dental
4	25	TLE	Vagus nerve stimulator
5	19	PLE	Subdural implant
6	15	TLE	Subdural implant
7	4	TLE	Ventricular bypass valve
8	16	FLE	Subdural implant
9	25	PLE	Dental
10	8	TLE	Dental
11	9	FLE	Dental
12	5	TLE	Subdural implant
13	6	TLE	Dental
14	3	TLE	Dental
<b>Mean</b>	<b>15.38</b>		
<b>Std</b>	<b>10.66</b>		

TLE: temporal lobe epilepsy, PLE: parietal lobe epilepsy,  
FLE: frontal lobe epilepsy.

#### 4.2.2 Volume conduction model

The patient's index points and head shape were digitized with a 3Space Fasttrack (Polhemus, Vermont, USA) prior to each measurement. The nasion, an anatomical landmark, and the left and right ear canal points served as index points and were used to define a right-handed coordinate system, called headframe coordinate system: the  $x$ -axis points to the front, the  $y$ -axis to the left, and the  $z$ -axis to the top of the head.

The scalp and brain meshes for each subject were obtained by aligning and warping the default anatomy provided by the Montreal Neurological institute with Brainstorm software (Tadel et al., 2011). The volume conduction model was obtained with the localspheres algorithm provided by Fieldtrip in which a local sphere is fitted to the brain surface for each separated channel (Huang et al., 1999).

#### 4.2.3 IED identification

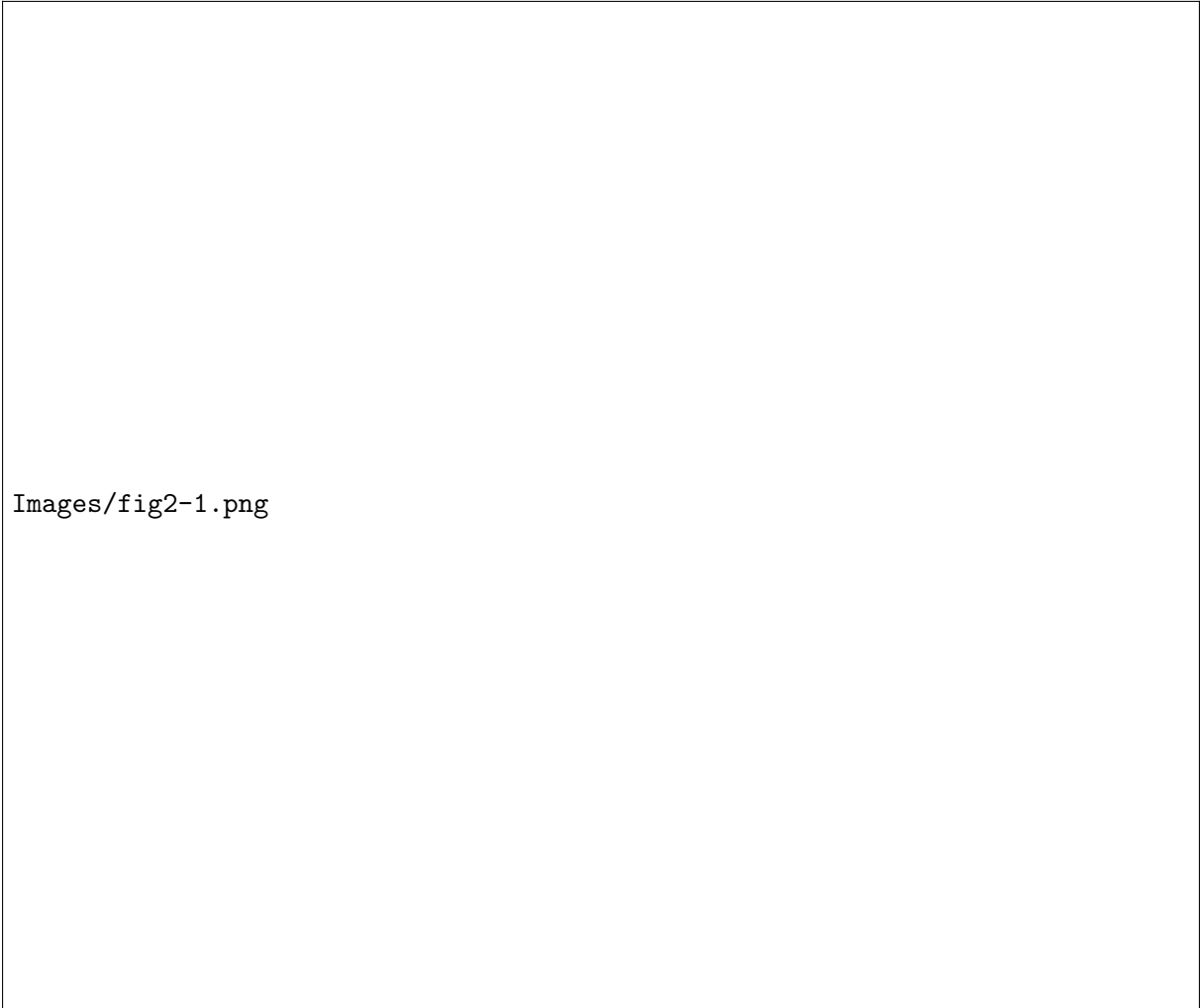
MEG data was visually inspected by three different experts for detection of IEDs. Well-defined IEDs, were selected following the definition of basic morphologic IED characteristics (Nowak et al., 2009; Jaseja and Jaseja, 2012). Inspection of the whole-head MEG data took into account

the simultaneous EEG recordings to verify IED presence and discard other waveforms, especially in highly artifacted MEG signals. For each IED identified by the three experts, the corresponding magnetic and electric isofield maps were obtained and inspected to assess its spatial distribution, looking for dipolar patterns on a sample-by-sample basis. Only those IEDs that produced stable voltage fields in the simultaneous EEG showing little change in shape and position over time were used since these are the most appropriate IEDs to be modeled by a dipolar distribution (Townsend and Ebersole, 2008). The onset of a spike was defined as the time point when spiking activity was distinguishable from the background noise and when a single distinctive dipolar pattern was observed in the simultaneous EEG (figure 4.1). The peak of a spike was defined as the maximum peak value after the spike onset. The channel closest to the origin of the dipolar activity was defined as the central channel. Since only a small number of MEG sensors show a prominent signal for a single source (Hämäläinen et al., 1993), a subset of 36 neighboring channels (25% of the total number of channels) at the time interval under study were selected for further ECD calculations. This selection was done in order to prevent under- and over-fitting phenomena as it has been demonstrated that not much is gained when using more than 40 channels when modeling spike potentials (Ebersole, 2003).

#### 4.2.4 Artifact removal

In this study, two different strategies were used to remove interference coming from metallic sources. The first consisted in the rejection of highly artifacted channels, and the second involved the application of a BSS-based automatic procedure for metallic artifact reduction.

Regarding channel rejection, the most affected channels were easily identified by visual inspection, because these prominent metallic artifacts exhibit characteristic features: high amplitude in comparison with the remaining MEG leads; and slow and regular waveforms, usually modulated by cardiac and respiratory activity (Hillebrand et al., 2013). The three experts examined the 37 channels selected for each IED and visually identified the artifacted channels following these criteria. Those channels identified by the three experts were excluded from the subsequent ECD estimation. Moreover, in order to prevent the over-fitting of the dipole model due to the channel reduction, additional and nearby artifact-free channels were selected to replace the ar-



Images/fig2-1.png

Figure 4.1: (a) Example of IED identification for subject 1 by in EEG simultaneous data. Green line denotes the spike onset and orange line the spike peaks. (b) Topographical map at spike onset where a dipolar distribution between T4 and P4 is observed.

tifactual channels in the ECD estimation. Thus, this ECD estimation was always performed using 37 channels. With respect to automatic artifact reduction, the 10 min MEG recordings of each patient were filtered of metallic contamination by using the fully automatic procedure described in (Migliorelli et al., 2015). This method is based on the AMUSE algorithm and decomposes the signals into independent components exploiting second order statistics (Tong et al., 1991), which proved effective enough in the separation of components corresponding to various types of artifacts (Escudero et al., 2010). The employed automatic methodology decomposed MEG signals into as many independent components as available channels, and these components were checked for known metallic interference features: regular behavior, measured by the sample entropy; and low frequency content, measured by the percentage of energy below

a specific frequency. Given these characteristics of each independent component, a two-step process was carried out, firstly to define the area or areas of the scalp corresponding to artifacted regions, and secondly to detect all independent components related to metallic activity. After these steps, the corrected artifact-free MEG data was obtained by reconstruction without considering the independent components associated with metallic artifacts. This method for automatic artifact reduction applied was previously validated with real and simulated signals in the study published in (Migliorelli et al., 2015). The amount of error for the artifact reduction procedure was significantly reduced (worst case around 2.5%). A detailed description of the actual algorithm is given in (Migliorelli et al., 2015).

To quantify the amount of interference removed, an artifact-to-signal ratio (ASR) was defined for each IED:

$$ASR = 100 \cdot \sum_n \left\langle \frac{\sum_t (s_n(t) - sf_n(t))^2}{\sum_t sf_n(t)} \right\rangle, \quad (4.1)$$

where  $n$  denotes the MEG channel,  $sf$  represents the filtered signal,  $s$  is the original raw signal, and  $\langle \rangle$  indicates average over all samples comprised between the beginning and the end of the IED (Nowak et al., 2009).

#### 4.2.5 Estimation of the ECD

Single dipole fitting was performed by means of the FieldTrip toolbox (Oostenveld et al., 2011), which uses grid search and nonlinear fitting trying to explain the MEG topography under study. The ECD model was fitted to the patient's head volume conduction model obtained as explained in section 4.2.2. No averaging of IEDs was performed, and a set of dipoles were estimated for each IED during its whole rising phase: from its onset to the spike peak using 4.5 ms time steps (i.e. three samples for each dipole). Each ECD was computed using the data of the subset of channels selected previously. The model was calculated using the maximum likelihood estimation approach that improves the accuracy of the dipole source localization (Lütkenhöner, 1998). The baseline noise (50 ms of recording not containing brain activity of interest) was considered as a multivariate Gaussian distribution and characterized by a covariance matrix.

The performance of the fitting procedure was assessed by means of the following goodness-of-fit measure:

$$,gof = 100 \cdot \left(1 - \frac{(v - \hat{v})^T((v - \hat{v}))}{v^T v}\right), \quad (4.2)$$

where  $v$  and  $\hat{v}$  represent the vectors of the measured and modeled magnetic fields, respectively and by the 95% confidence volume defined as the volume of the ellipsoid comprising the confidence intervals of each of the dipole projections:  $x$ ,  $y$  and  $z$ :

$$V = \frac{4\pi}{3} \cdot \frac{CI_x}{2} \cdot \frac{CI_y}{2} \cdot \frac{CI_z}{2}, \quad (4.3)$$

where  $CI_x$ ,  $CI_y$  and  $CI_z$  represent the 95% confidence interval in each of the dipole directions.

Dipole fitting was applied to all IEDs and their corresponding 37 selected channels for three different conditions: (1) using all channels without removing metallic interference; (2) rejecting channels with large metallic artifacts visually determined by the experts; and (3) after applying the BSS-based metallic reduction procedure. Ten IEDs were selected for further study, corresponding to those which obtained the lowest confidence volume in the first condition, with a minimum *gof* threshold value of 85%.

#### 4.2.6 Evaluation of estimated sources

To evaluate the differences among the three conditions, the distribution of the obtained dipoles at the onset time for each patient was analyzed by means of its central position and dispersion. Additionally, the running distance of the path followed by dipoles associated to each IED was computed. For these purposes, IEDs showing estimated sources outside of the head were excluded to maintain anatomical plausibility. To calculate this running distance, the whole computed ECDs from the spike onset to the spike peak were used to check the consistency of each IED during the rising phase of the spike.

The distance of each IED path was computed as the sum of the distances between consecutive dipoles. Since IEDs that produce a stable magnetic field and show little change in shape and

position over time where used in this study, it is expected to find a slight unidirectional change in the dipole position during the whole rising phase of the dipole (Townsend and Ebersole, 2008)(Townsend and Ebersole 2008). Moving dipole models that make sudden changes in direction may be the result of multiple sources overlapping, as occurs when dealing with metallic artifact. For this reason, distance values are expected to be lower when the source is produced by a single dipolar source.

The central source position was obtained as the averaged position of all estimated ECDs of the ten selected IEDs of each patient. The total dispersion was calculated as the average distance between each ECD and the central position.

## 4.3 Results

### 4.3.1 Artifact removal

For the channel rejection approach, the 37 selected channels of each selected IED and patient were visually inspected by the three experts. Channels with presence of metallic artifacts showing regular behavior and considerably higher amplitudes than the rest of the channels were removed from the analysis, but only if they had been identified by the three experts. The agreement among experts was quantified by calculating the kappa index (Viera and Garrett, 2005) and a high inter-rater reliability was obtained ( $\text{kappa} = 0.87 \pm 0.10$ ). Table 4.2 contains the number of rejected channels and shows that four subjects did not show artifacted channels in the area of the dipole. No rejection was performed in these cases.

Figure 4.2(a) shows, as an example, a 5 s epoch of the 37 selected raw channels used to fit ECDs in the case of metallic artifacts of dental origin affecting the right temporal zone of the scalp (patient 1). Highly artifacted channels selected to be removed are emphasized in red.

The BSS-based automatic artifact reduction procedure was applied to the 10 min records and independent components corresponding to metallic artifacts were removed before signal reconstruction. Figure 4.2(b) shows an example of the corrected MEG signals, where it can be observed how the energy of highly artifacted channels decreased markedly. The number of in-

Table 4.2: Results for all patients

Subj.	R.chan.	R.IC	ASR	R.IEDs		Confidence Volume		Dispersion			Distance				
				NC	CR	NC	CR	AF	NC	CR	AF	NC	CR	AF	
1	7	10	549.75	1	1	65.65	48.24	24.97	1.86	1.18	0.62	4.15	3.62	2.19	
2	2	6	93	1	0	39.47	31.55	10.85	3.31	2.22	2.16	7.93	18.49	4.21	
3	1	15	54.57	1	1	49.14	19.24	4.61	2.97	2.92	3.05	16.18	10.74	5.50	
4	0	21	1147.72	2	2	18.91	18.91	3.35	3.88	3.88	0.95	11.88	11.88	2.83	
5	0	17	92.23	0	0	15.51	15.51	14.14	1.12	1.12	1.01	3.79	3.79	2.12	
6	12	36	1991.77	2	1	67.84	35.28	18.87	7.30	3.54	1.92	5.65	6.98	2.78	
7	3	7	283.58	5	1	27.55	27.77	24.88	3.12	1.94	1.98	8.01	5.55	3.13	
8	0	14	195.6	1	1	47.94	47.94	37.51	2.44	2.44	2.21	23.84	23.84	2.27	
9	0	4	66.7	1	1	32.04	32.04	11.85	1.65	1.65	1.54	14.60	14.60	3.05	
10	4	8	1241.27	2	2	26.24	19.58	15.13	8.03	3.15	1.08	10.83	6.21	3.41	
11	4	11	145.42	0	0	27.24	21.29	21.19	1.14	0.77	0.76	1.52	1.74	1.86	
12	4	18	170.57	1	1	79.56	12.50	8.84	1.37	1.03	1.12	5.12	5.39	3.32	
13	7	6	939.85	5	1	14.11	8.76	7.78	7.10	3.65	3.12	13.06	3.07	2.49	
14	5	3	733.14	1	0	9.50	9.45	8.84	2.42	1.64	0.51	6.91	4.44	1.82	
Mean	3.23	12.57	550.37			37.19	24.72	15.20	3.41	2.22	1.57	9.53	8.6	2.93	
Std	3.48	8.72	588.41			21.17	12.80	9.43	2.36	1.06	0.85	5.99	6.52	1.00	

R.Chan: Removed Channels, R.IC: Removed independent components R.IEDs: Removed IEDs, NC: Non corrected, CR: Channel removal, AF: Artifact filtering


dependent components removed was  $12.57 \pm 8.72$  (out of 148, mean and standard deviation for all patients).

The topographic distribution of normalized energy corresponding to the removed metallic activity is shown in the maps of figure 4.3. Each map presents a different distribution of energy that mainly depended on the type of metallic artifact. Table 4.2 also shows the average ASR obtained for each patient, evidencing a high variability among subjects probably due to the different nature of metallic contamination.

### 4.3.2 ECD estimation

Temporal signals and electric isofields from each IED were analyzed to identify spike onsets time considering morphological IED characteristics and field dipolar distribution (figure 4.1). Figure 4.4(a) shows the magnetic isofield of a spike, corresponding to the spike in figures 4.1 and 4.2 (onset indicated by a green vertical line), before applying the artifact reduction procedure. Figures 4.4(b) and (c) show the equivalent maps to figure 4.4(a) when channel rejection and the automatic artifact reduction were performed, respectively. Magnetic isofields changed,





Images/fig2-2.png

Figure 4.2: 5 s epoch corresponding to 37 MEG channels for subject 1 selected for dipole fitting. Vertical lines show the onset of at the same well-defined IED shown in figure 4.1. (a) RAW signal before applying automatic reduction procedure. Red channels were selected by experts as highly artifacted channels and removed in the channel rejection procedure. (b) Corrected MEG signals obtained after applying automatic AMUSE-based metallic removal procedure.

suggesting different dipole locations depending on the approach. Figure 4.4(c) presented a more plausible dipolar distribution more similar to EEG distribution (figure 4.1(b)).

Dipoles were calculated at each IED onset in three cases: (1) using all 37 selected channels without any kind of correction; (2) rejecting channels with clearly visible metallic artifacts; and (3) applying an automatic BSS-based artifact reduction. The ten IEDs whose dipoles achieved the lowest  $V$  in the first case were selected for further study, taking into account a minimum  $gof$  value of 85%. Paired sample T-tests with significance set to 0.05 were used to compare the three approaches. The confidence volume measure showed significant differences between the three approaches ( $p\text{-value} < 0.04$  in any case). No statistically significant differences were obtained for the  $gof$  values.

Figure 4.5 shows the positions of the dipoles obtained for the ten IEDs of patient 1 (planes  $XY$ ,  $XZ$ , and  $YZ$ ). Dipoles are drawn inside the anatomical representation of the head and brain of the patient. Dipoles that appeared outside of the brain cortex (see dipole 4 of the no-correction approach, in blue), were discarded for subsequent measurements of dispersion and distance, which were calculated for all 14 subjects and the three approaches.

Table 4.2 shows the obtained dispersion values for each patient and the number of spikes dis-

Images/fig2-3.png

Figure 4.3: Topographic distribution of normalized energy corresponding to the removed metallic activity for the 14 subjects. Artifact distribution of energy mainly depended on the type of metallic interference, to its position and size.

carded due to their location outside the brain. Interestingly, all dipoles obtained after BSS-based artifact reduction were found inside the head, and therefore it was possible to use all of them to estimate the dispersion measure. The average dispersion for all patients was of  $3.41 \pm 2.36$  cm if no artifact filtering was applied, and this value decreased to  $2.22 \pm 1.06$  cm when channel rejection was performed ( $p\text{-value} = 0.06$  with respect to no artifact correction), and decreased even more if automatic BSS-based reduction was chosen, reaching a value of  $1.57 \pm 0.85$  cm ( $p\text{-values}$  of 0.007 and 0.036 with respect to no artifact correction and channel rejection approaches, respectively). Differences between automatic approach and the two previous were statistically significant (paired T-tests, significance set to 0.05), with probability values of 0.007 and 0.036 for non-corrected signals and channel rejection approaches, respectively.

With respect to the running distance of ECDs, figure 4.6 shows an example of the positions obtained for the consecutive dipoles fitted during the rising phase of an IED. Table 4.2 demonstrates that the distance traveled by ECDs was clearly lower after applying the automatic procedure: distances for the naive and the channel rejection approaches showed similar values of  $9.53 \pm 5.99$  cm and  $8.60 \pm 6.52$  cm, respectively (no significant differences were found,  $p\text{-value} = 0.277$ ), whereas the automatic filtering obtained a measure of  $2.93 \pm 1.00$  cm. Analogously to the dispersion measure, differences between the automatic approach were significant, with probability values of 0.001 and 0.003 for non-corrected signals and channel rejection approaches, respectively.


Images/fig2-4.png

Figure 4.4: Magnetic isofields computed for the 37 selected channels corresponding to the same IED onset shown in figure 4.1. For the three approaches: (a) before applying any filtering procedure (no correction), (b) after channel rejection, (red channels were removed, green channels were included); and (c) after applying the metallic reduction procedure. The central channel is shown in blue.

### 4.3.3 Influence of the ASR on dipole localization.

Metallic artifacts affected MEG signals with different intensity depending on the region of the scalp (see figure 4.3), which was primarily determined by the nature of the artifact. ASR values, which were defined for the 37-channel region where dipole fitting was performed, are shown in table 4.2. As ASR increased, ECD fitting of non-corrected MEG data produced more scattered dipoles and therefore a higher dispersion value, as evidenced by the linear regression shown in figure 4.7.

Two additional regressions were studied to assess the influence of artifact levels on ECD fitting before and after applying the BSS-based automatic reduction of metallic artifacts, as shown in figure 4.8. Figure 4.8(a) is a scatterplot of ASR versus the distance between central source position before and after the automatic artifact reduction procedure for all subjects. For small ASR values, distances were lower than 1 cm, but they increased as ASR did. An equivalent analysis was performed for differences in dispersion measures, shown in figure 4.8(b), and similar results were obtained indicating higher dispersion as ASR increased. Regression lines showed values of  $r = 0.75$  ( $p\text{-value} = 0.002$ ) and  $0.89$  ( $p\text{-value} < 0.001$ ), respectively.



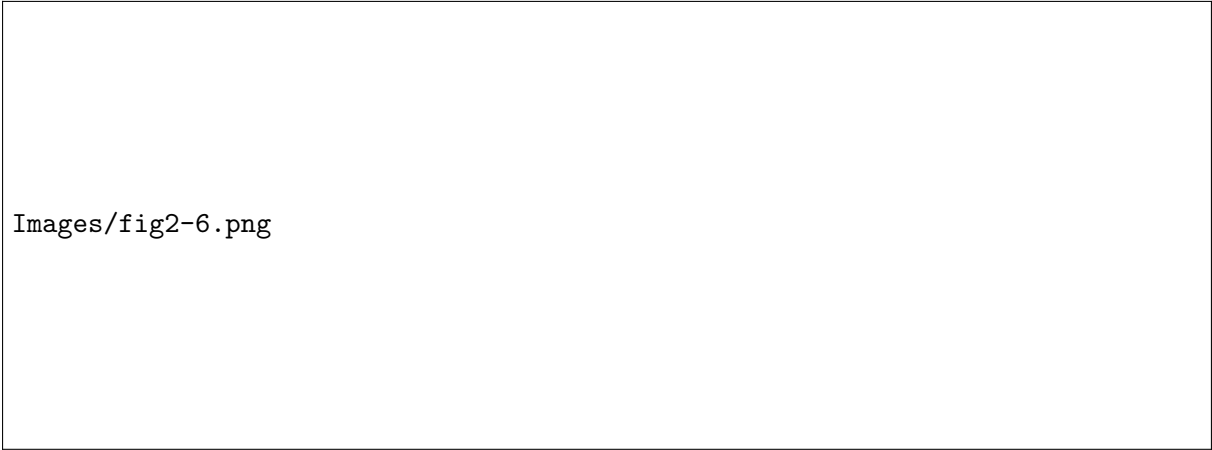
Images/fig2-5.png

Figure 4.5: Dipoles obtained for the ten IEDs of Patient 1 (a)  $XY$  plane, (b)  $XZ$  plane and (c)  $YZ$  plane. Blue, green and red dipoles belong to no-correction, channel rejection and automatic filter procedures. Dipole 4, located outside the brain in the no-correction procedure, was discarded for the subsequent measurements of dispersion and distance.

## 4.4 Discussion

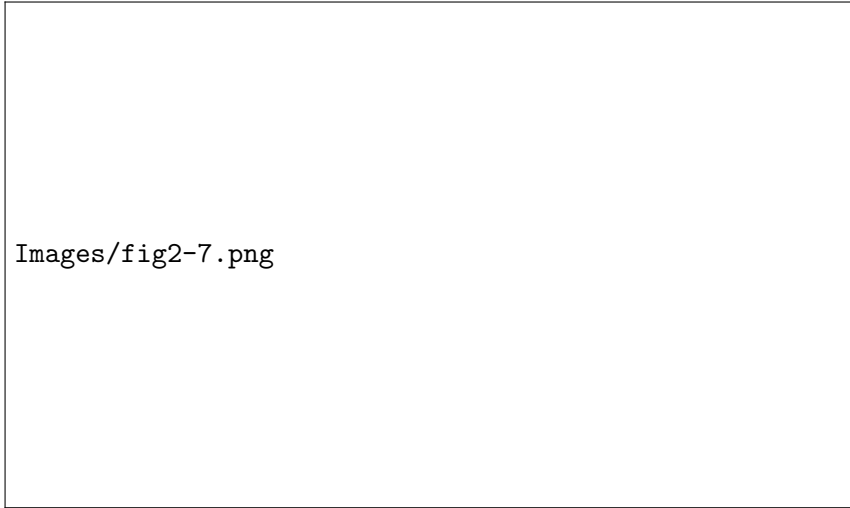
Patients suffering from refractory epilepsy usually have to undergo resective surgery, and this process requires an extensive presurgical evaluation to determine the epileptogenic area and to plan the suitable strategies for neurosurgery, taking into account the functions of nearby areas before the resection. Several studies have determined that MEG interictal epileptiform activity is useful to locate epileptic foci (Shibasaki et al., 2007; Enatsu et al., 2008; Englot et al., 2015), and although it cannot replace intracranial EEG at the present time (Shibasaki et al., 2007), MEG can often provide additional and useful information mainly because of its whole-head coverage. Even in those cases where intracranial recordings are strictly necessary (generally when the sources are deep), MEG recordings are useful to determine the area where the electrodes will be implanted. This technique has shown superior performance than EEG (Amo et al., 2003; Stefan et al., 2004; Ramantani et al., 2006).

The standard clinical MEG procedure consists in the inspection of the recordings and the detection of well-defined IEDs so that ECD fitting can be performed to locate an epileptic source. Dealing with metallic artifacts is one of the main drawbacks of the MEG technique because they can affect many subjects (Vrba, 2002). For Elekta-Neuromag systems, the tSSS approach has proven to be effective removing metallic interference coming from different sources (Song et al., 2009; Kakisaka et al., 2012; Jin et al., 2013; Wang et al., 2013). As explained before,



Images/fig2-6.png

Figure 4.6: Positions obtained for the consecutive fitted dipoles during the rising phase of an IED. (a)  $XY$  plane, (b)  $XZ$  plane and (c)  $YZ$  plane. Blue, green and red dipoles belong to no-correction, channel rejection and automatic filter procedures. The dipole measured at the onset of the IED is displayed as 'o'.



Images/fig2-7.png

Figure 4.7: Dispersion values versus ASR for the 14 subjects. Linear regression showed a value of  $r = 0.80$  ( $p\text{-value} = 0.0005$ ).

this technique is not applicable to signals from different MEG systems and the algorithm is not freely available. There are no comparative studies among this technique with other artifact reduction algorithms such as BSS. The analysis of the differences and advantages of these two algorithms in Elekta MEG systems would be an interesting field of study. In an interesting study held by (Gonzalez-Moreno et al., 2014) an SNR analysis was carried out applying tSSS followed by a BSS procedure. The study concluded that SNR increased by 100% after applying tSSS techniques and an additional 33%–36% after applying BSS methods suggesting that not all noise was successfully removed by the tSSS method.

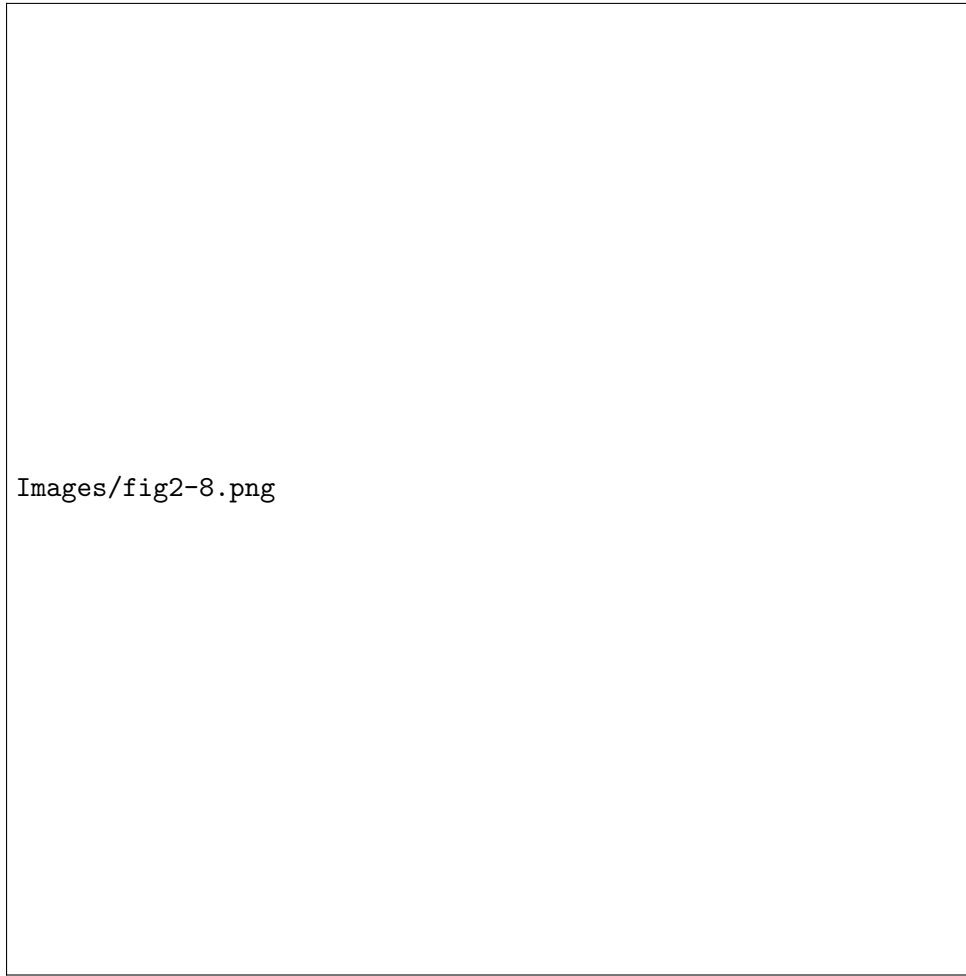


Figure 4.8: (a) Difference between central source position before and after applying automatic filtering procedure versus ASR. Regression line showed a value of  $r = 0.75$  ( $p\text{-value} = 0.002$ ). (b) Difference between dispersions versus ASR. Regression line showed a value of  $r = 0.89$  ( $p\text{-value} < 0.001$ ).

In this study, the effectiveness of an automatic BSS-based artifact reduction procedure algorithm, described in detail and validated in (Migliorelli et al., 2015), was evaluated in patients with refractory focal epilepsy. A comparative analysis of ECD estimation through different usual clinical approaches was performed: using MEG signals without any metallic artifact correction; rejecting highly affected channels; and applying the automatic BSS-based procedure. The resulting dipole locations corresponding to ten well-defined IEDs were analyzed.

Metallic artifacts can be produced by different sources such as dental implants or brackets, cerebral implants such as intracranial electrodes or subdural grids, vagal stimulators, and ventricular bypass valves, among others. Depending on the kind of source, its size and its position, metallic artifacts can affect different areas of the scalp with varying intensity. This variability generates

multiple situations in which artifacts can impact on big areas, or appear localized in a specific region with different intensity, usually exceeding the energy of cerebral activity by several orders of magnitude. The BSS-based automatic artifact correction procedure was able to successfully detect independent components associated to metallic activity and allowing an effective reduction of their effects. This methodology also provided an objective measure of the high variability observed in metallic artifacts as quantified by independent component detection: subjects with very focused artifacts (patients 2, 9, 13, and 14) presented fewer components related to metallic artifacts than subjects with artifacts more spread over the head (patients 3, 6, and 12).

Recordings affected by metallic interference produced highly artifacted temporal signals where brain activity appeared completely masked in some electrodes or regions. Detection of interictal epileptiform activity in this scenario may be a challenging task in clinical routine, especially in cases where the artifacted region overlaps the area where IEDs show maximum magnetic activity. As shown in the example in figure 4.3, metallic interference mainly affected channels in red and was successfully removed from the MEG signal after applying the BSS-based artifact reduction procedure. Although some well-defined IEDs were detected in the artifacted recordings, spike identification became easier after artifact reduction.

Even if well-defined IEDs can be detected in the presence of metallic artifacts, ECD estimation may produce dipoles whose position is outside the brain. It is important to notice that high values of  $gof$  and low values of  $V$  do not imply a feasible physiological location, since this two measures only quantify the fitting of real data to the dipolar model. In other words, if measured data correspond to dipolar sources outside the brain, the ECD estimation will be able to fit a dipole with an excellent  $gof$  and low  $V$ . That is the main reason why the naive approach of using signals without any kind of artifact correction and even the artifacted channel rejection strategy produced several dipoles located outside the brain. These dipoles were discarded for further analysis, and consequently these two approaches provided fewer dipoles than the automatic artifact reduction. This approach always produced dipoles inside the brain and its dispersion and distance measures were computed using all the ten identified IEDs.

For each subject, all the identified IEDs produced similar magnetoencephalographic activity and exhibited their maximum value at the same area of the scalp, showing a similar dipolar

distribution. Under these circumstances, the identified IEDs were expected to be generated by the same internal sources. The dispersion of the location of the fitted dipoles with respect to their average (central source position) was calculated for each subject for the three approaches: naïve, channel rejection, and automatic artifact reduction. As expected, the best results were obtained for the artifact reduction approach. Although more dipoles were obtained inside the brain when performing channel rejection, the corresponding dispersion values did not significantly improve with respect to the naïve approach.

The beginning of epileptiform activity is represented by IED onset, and thus this is the desired point to apply ECD estimation (Bagić et al., 2011). However, the point with the lowest signal-to-noise ratio corresponds to the peak value of a spike. The rising phase of the IED progresses between these two instants and the dipole moves due to the propagation of the epileptiform activity. Observing and characterizing the course of these propagations could be considered a reliable way of assessing the likelihood of the estimated dipoles after the application of different artifact reduction methodologies. Stable dipole trajectories, without abrupt changes of position or direction, are most likely associated with a single cerebral source and can be explained by a single-dipole model (Townsend and Ebersole, 2008) (Townsend and Ebersole 2008). Following this reasoning, several dipoles, estimated during the rising phase of an IED, are shown in figure 4.6. Interestingly, the distribution of dipoles exhibited a more stable time course and distribution after automatic artifact correction, whereas dipoles should be discarded for further analysis due to instability in the other two approaches. Stability was measured by the running distance of IED paths for all patients, and results of table 4.2 evidenced significantly reduced distances for the automatic artifact reduction approach. Removing artifacted channels did not produce any improvement in distances and therefore in the stability of the dipole during the rising phase of the IED.

Metallic artifacts can affect recordings with varying energy, projecting on different areas of the scalp. In order to analyze the effect of metallic artifacts on detected IEDs, the relationship between their dispersion and the ASR for artifacted data is shown in figure 4.7. Results indicated more variability in the location of estimated ECDs of a subject when metallic artifacts were higher, resulting in higher values of dispersion. In this sense, the differences in central source position and dispersion observed before and after applying the BSS-based automatic artifact



reduction procedure evidenced that dipole locations changed significantly for high values of ASR, but were not altered when lower levels of artifacts were present (see figure 4.8). Noticeably, the high dispersion values shown in figure 4.7 corresponded to the highest differences depicted in figure 4.8, demonstrating that the artifact reduction approach produced a more reliable ECD estimation thanks to reduced levels of metallic artifacts.

Although the results show a significant improvement of the dipole fitting procedure, an additional validation with the actual localization of the epileptic focus would have been useful. However, in this study, no detailed information about surgery or intracranial electrodes data was available. Nevertheless, lower levels of dispersion and distance measures shown by data after applying the artifact reduction procedure suggested an improvement in the stability of the dipolar sources and therefore a more reasonable association with the discharges produced by the epileptic tissue.

Hence, the results encourage the use of such a BSS-based automatic artifact reduction procedure to improve IED detection and reliable ECD fitting in these patients whose MEG recordings are affected by metallic interference, which otherwise would not be suitable for presurgical analysis and would require alternative and possibly more invasive strategies to prepare for resective surgery.

## 4.5 Acknowledgments

CIBERBBN is an initiative of the Instituto de Salud Carlos III, Spain. This work has been partially supported by the Ministry of Economy and Competitiveness (MINECO), Spain, under contract DPI201459049R and the Ministry of Education, Culture and Sports (MECD) FPU12/05631.

## Chapter 5

# Automated detection of Epileptic Ripples in MEG using beamformer-based Virtual Sensors

**Published as:** Migliorelli, C., Alonso J.F., Romero S., Mañanas, Nowak R. and Russi A. Automated detection of Epileptic Ripples in MEG using beamformer-based Virtual Sensors. *Journal of Neural Engineering Accepted Manuscript*

doi: 10.1088/1741-2552/aa684c

Impact Factor: 3.493; Position 10 of 76 (Q1) BIOMEDICAL ENGINEERING.

**Abstract:** *Objective.* In epilepsy, high-frequency oscillations (HFOs) are considered events highly linked to the seizure onset zone (SOZ). The detection of HFOs in noninvasive signals such as scalp EEG and MEG is still a challenging task. The aim of this study was to automatize the detection of ripples in MEG signals reducing the high-frequency noise using beamformer-based virtual sensors (VS) and applying an automatic procedure exploring the time-frequency content of the detected events. *Approach.* 200 seconds of MEG signals and simultaneous iEEG were selected in nine patients with refractory epilepsy. A two-stage algorithm was implemented. Firstly, beamforming was applied to the whole head to delimitate the region of interest (ROI) within a coarse grid of MEG-VS. Secondly, a beamformer using a finer grid in the ROI was

computed. The automatic detection of ripples was performed using the time-frequency response provided by the Stockwell Transform. The performance was evaluated by comparing with simultaneous iEEG signals. *Main results.* For the nine subjects, ROIs were located within the seizure-generating lobes. Precision and sensitivity values were 79.18% and 68.88%, respectively, considering iEEG detected events as benchmark. A higher number of ripples were detected inside the ROI compared to the same region in the contralateral lobe. *Significance.* The evaluation of interictal ripples using noninvasive techniques can help in the delimitation of the EZ and guide the placement of intracranial electrodes. This is the first study that automatically detects ripples in MEG in the time domain located within the clinically expected epileptic area taking into account the time-frequency characteristics of the events through the whole signal spectrum. The algorithm was tested against intracranial recordings, the current gold standard. Further studies should explore this approach to enable the localization of noninvasively recorded HFOs to help during pre-surgical planning and to reduce the need for invasive diagnostics.

**Keywords:** high frequency oscillations, epilepsy, MEG, ripples, beamformer.

## 5.1 Introduction

Epilepsy is a neurological disorder that affects about 1% of the world population (Ramey et al., 2013). The most common therapeutic treatment relies on antiepileptic drugs (AEDs) which aims to reduce or eliminate seizures. Approximately 20% to 40% of patients diagnosed with epilepsy become refractory to treatment (Liu et al., 2015b). For these patients, the most frequent therapeutic alternative is the neurosurgical resection of the epileptogenic zone (EZ), defined as the cortex area that is necessary and sufficient for initiating the epileptic discharges and whose removal is necessary for complete abolition of seizures (Schuele and Lüders, 2008).

In current practice, the epileptogenic zone is approximated by the seizure onset zone (SOZ), defined as the area where the clinical seizures originate. The delimitation of this area is often done by the presurgical analysis with intracranial electroencephalography (iEEG) (Rosenow and Lüders, 2001) during the pre-ictal and ictal periods. In several recent studies, high-frequency oscillations (HFOs) have been evaluated as a specific biomarker for epileptogenicity in iEEG (Jacobs et al., 2012; Fujiwara et al., 2012; Sun et al., 2015a). These fast oscillations appear in

the frequency range of 80-500Hz, classified into ripples (80-200Hz) and fast ripples (200-500Hz) and are defined as spontaneous patterns above the baseline, clearly distinguished from noise and with at least four oscillations (Worrell et al., 2012). They can be recorded during the interictal period, without having to record ictal activity and thereby, reduce discomfort and risk for the patient as well as the recording time. HFOs may appear in concordance with interictal epileptiform discharges (IEDs) but also isolated. The relationship between them is still an open discussion although HFOs seem to be more specific to delimitate the EZ than IEDs (Jacobs et al., 2012).

Visual marking of HFOs is highly time-consuming. For iEEG, several automatic algorithms have been proposed in the time domain and in the time-frequency domain (Liu et al., 2016; Burnos et al., 2014; von Ellenrieder et al., 2012; Zelmann et al., 2012). Time-frequency domain detectors can considerably reduce the false positives but also are computationally more demanding. The detection of HFOs in non-invasive signals such as scalp EEG and magnetoencephalography (MEG) is still a challenging task, mainly because of the low signal-to-noise ratio (SNR) in high-frequency bands (Muthukumaraswamy, 2013). MEG and EEG signals must be adequately preprocessed to reduce biological and environmental interferences coming from different sources (Stufflebeam et al., 2009). Recent studies have shown that fast oscillations related to epilepsy can be identified in scalp EEG (Andrade-Valenca et al., 2011; Melani et al., 2013; Fahoum et al., 2014; Zelmann et al., 2014), however, depending on the number of channels and due to the distortion of the signals caused by the skull, this technique may attenuate high frequency activity and present a poor spatial resolution (Zelmann et al., 2014).

As it is much less influenced by the electrical conductivity of the surrounding tissues on the cerebral cortex (Shibasaki et al., 2007), MEG can provide a more accurate non-invasive biomarker for epileptogenicity (Muthukumaraswamy, 2013). Some studies in MEG investigate the power in high frequency bands (Papadelis et al., 2016; Miao et al., 2014; Tenney et al., 2014). There are few recent studies that have successfully detected high frequency activity at the time domain. In the study developed by von Ellenrieder et. al. (von Ellenrieder et al., 2016), an automatic detection of fast oscillations (FO) (40-160Hz) previously developed for scalp EEG (von Ellenrieder et al., 2012), followed by a visual discarding of false positives performed in scalp MEG, and then compared with the epileptogenic region defined by two specialists. However, presumably due

to the low SNR of the FOs, the detection produced unsuccessful source localizations in some patients. Van Klink et. al. introduced an interesting approach to detect HFOs improving the SNR using beamformer localization (van Klink et al., 2016), one of the most used approaches for detecting MEG sources (Baillet et al., 2001). Beamformer reconstructs neuronal activity in a particular position as a weighted contribution from different sensors acting as a spatial filter capable to reduce and attenuate noise from distant sources (Hillebrand and Barnes, 2005; Vrba, 2002; Muthukumaraswamy, 2013). Time domain signals can be reconstructed at specific locations, usually known as virtual sensors (VS) that can reveal information that is not discernable in the physical sensors (van Klink et al., 2016). The detection of HFOs was done visually, and the determination of the region of interest was based on the localization of IEDs. This region is commonly known as the irritative zone (Rosenow and Lüders, 2001), a region that is usually more extensive than the theoretical EZ and that may even not overlap it.

In this study, an automatic method to detect ripples (80-120Hz) in MEG is proposed. To remove high frequency noise, a beamformer analysis similar to (van Klink et al., 2016) was performed in a two-step approach. VS were used for the identification of epileptic HFOs that could not be assessed at the MEG sensor level. A simpler version of this approach was developed for a preliminary study (Migliorelli et al., 2017a) where HFOs were visually observed in the region of interest and compared with simultaneous iEEG recordings. In this study, a comparison between the automated detection of ripples in MEG and iEEG was performed. To the author's knowledge, this is the first automatic algorithm that detect HFOs in MEG time course signals.

## 5.2 Materials and Methods

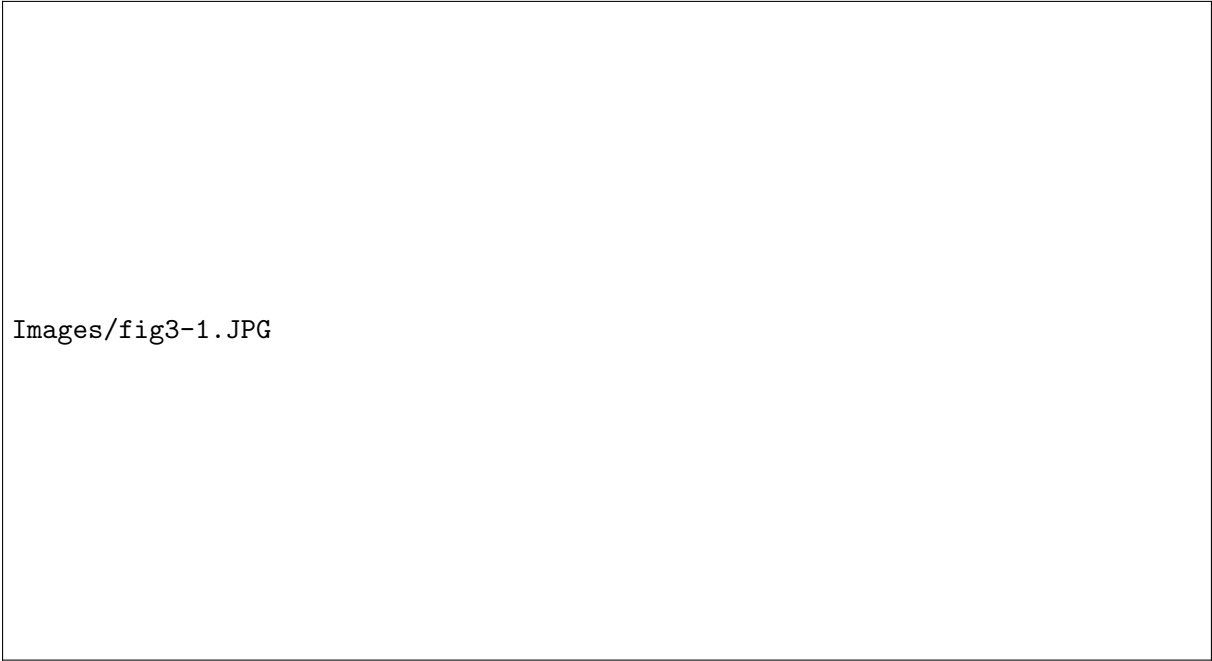
### 5.2.1 Patients, signal acquisition settings and previous preprocessing.

Nine patients diagnosed with intractable epilepsy were selected for this study. All of them had simultaneous MEG and iEEG recordings. The selected subjects for this study presented interictal activity coming from one focal generator. Table 5.1 shows the summary of the available clinical information, seizure type, the area where the ictal electrode was identified by clinicians and iEEG contact number.

Table 5.1: Clinical information of the Patients

Patient	Sex/Age	Seizure type	Ictal Electrode placement	N° of iEEG contacts
1	M/9	OLE complex partial (L)	Occipital (L)	8
2	F/9	MTLE complex partial (R)	Middle Temporal (R)	6
3	M/6	MTLE complex partial (R)	Middle Temporal (R)	6
4	M/13	MTLE complex partial (R)	Middle Temporal (R)	6
5	M/10	OLE complex partial (L)	Occipital (L)	8
6	F/22	MTLE complex partial (L)	Middle Temporal (L)	6
7	M/6	MTLE complex partial (R)	Middle Temporal (R)	6
8	M/9	MTLE complex partial (R)	Middle Temporal (R)	8
9	M/7	MTLE complex partial (R)	Middle Temporal (R)	6

MEG signals were acquired in a magnetically shielded room during 10 minutes with eyes closed in supine position in order to remove head movements. A whole-head 148-channel magnetometer system (4D-Neuroimaging/BTi San Diego, California USA) sampled at 678,19Hz (bandwidth DC to 250Hz) was used to acquire MEG signals and simultaneously, iEEG was recorded using the same sampling rate and bandwidth conditions. For each patient, one depth electrode was implanted on the target region. Each electrode was 1.1 mm in diameter and included 6, or 8 leads 2,4 mm in length, 5 mm apart (AD-TECH, Racine, WI). The relative position of the patient's head with respect to the MEG sensors was recorded continuously using head-localization coils. Signals were imported into MATLAB using the Fieldtrip toolbox (Oostenveld et al., 2011). MEG was filtered to remove ocular, cardiac, and metallic artifacts using automatic blind source separation algorithms (Migliorelli et al., 2015; Romero et al., 2009), and visually inspected to select 200s of interictal periods for posterior analysis. These algorithms have proven to be effective in the localization of epileptic sources (Migliorelli et al., 2016). The general recommendation, to be able to visualize HFOs, is to use a sampling frequency of at least 5 times the frequency of the oscillation of interest (Worrell et al., 2012) and, for this reason, the maximum frequency of analysis was set to 120Hz. MEG and iEEG signals were band-pass filtered from 1 to 120Hz to obtain the whole spectrum ( $MEG_{WS}$ ) within these two frequencies and from 80 to 120Hz to obtain the high frequency spectrum ( $MEG_{HF}$ ) in both cases using a FIR filter (80<sup>th</sup> order).



Images/fig3-1.JPG

Figure 5.1: Scheme of the two stages HFO detection algorithm.

### 5.2.2 Volume conduction model

The patient's index points and head shape were digitized with a 3Space Fasttrack (Polhemus, Vermont, USA) prior to each measurement. The nasion, an anatomical landmark, and the left and right ear canal points served as index points and were used to define a right-handed coordinate system, called headframe coordinate system: the x-axis points to the front, the y-axis to the left, and the z-axis to the top of the head.

The scalp and brain meshes for each subject were obtained by aligning and warping the default anatomy provided by the Montreal Neurological Institute with the Brainstorm software (Tadel et al., 2011). The volume conduction model was obtained with the single shell algorithm provided by Fieldtrip in which a realistic single shell model based on lead field expansion is computed (Nolte, 2003).

### 5.2.3 MEG automatic detection of ripples

The proposed algorithm was divided into two main steps:

- In the first step, beamforming was applied to the whole head within a coarse grid of MEG-

VS to delimitate the region of interest. As beamformer computation time increases with higher resolution, this step allowed to delimitate the area of analysis in an efficient way.

- In the second step, a second beamformer in the region of interest was computed and a finer MEG-VS grid was obtained. The automatic detection of ripples was performed with a modified version of the algorithm developed by (Burnos et al., 2014). This algorithm uses the Stockwell Transform (Stockwell et al., 1996) which provides an excellent time-frequency decomposition and reduces the computational run time.

In order to assess the performance of the proposed procedure, ripples detected in simultaneous iEEG signals were used as the gold standard. To facilitate the understanding of the whole procedure, a scheme is shown in Figure 5.1 and detailed explanation is provided in the next subsections.

### First Stage: whole-head Beamformer and detection of the region of interest (ROI)

- (a) *Whole-head Beamformer:* The first stage was performed to define the area where the epileptic high-frequency activity was taking place. To obtain this area, a Linearly Constrained Minimum Variance Beamformer (LCMV-Beamformer) (Van Veen et al., 1997) was computed to obtain the weights of the spatial filtering using an evenly spaced (1.5 cm) grid of VS including the whole brain volume of each subject. Beamformer weights ( $BF_w$ ) were computed from  $MEG_{HF}$  using sliding windows of 100ms with a 50% overlapping. For each time segment, Virtual sensors ( $VS_{HF}$ ) were obtained as the product of the MEGHF signals with the filter weights projecting the time-series along a unique dipole direction corresponding to the maximum variance, following the equation 5.1:

$$\begin{matrix} VS_{HF} \\ n \times s \end{matrix} = \begin{matrix} BF_w \\ n \times m \end{matrix} \cdot \begin{matrix} MEG_{HF} \\ m \times s \end{matrix} \quad (5.1)$$

where  $n$  is the number of  $VS_{HF}$ ,  $m$  is the number of MEG channels and  $s$  is the length of the signal. The noise covariance was computed with the first 10 seconds of the unfiltered data (van Klink et al., 2016). Finally, MEG-VS signals were reconstructed averaging the overlapped and successive time segments.



- (b) *Detection of events of interest:* For each computed VSHF, events of interest (EOIs) were detected using an adapted version of the first phase of the algorithm developed in (Burnos et al., 2014) for iEEG signals. For each VSHF:
- (1) The envelope of the band-pass signal was computed with the Hilbert transform
  - (2) The mean and the standard deviation (SD) of the envelope was computed to set a threshold equal to  $mean + 3 \cdot SD$ .
  - (3) An event was detected when the envelope exceeded the threshold. The duration of the event was defined as the interval between the upward and downward crossings through half the detection threshold, that was  $0.5 \cdot (mean + 3 \cdot SD)$ .
  - (4) If the duration of the event exceeded 6 ms, the event was qualified as an EOI.
  - (5) EOIs with an inter-event interval of less than 10 ms were merged.
  - (6) Events not having a minimum of 4 peaks greater than  $2 \cdot SD$  from the mean baseline were rejected.
- (c) *ROI selection:* Using the information provided by the EOIs, where a preliminary selection of high-frequency activity was performed discarding a fair amount of noisy events, a region with greater epileptogenic high-frequency activity could be delimited. To do so, the number of EOIs appearing in each VSHF was computed, and all possible  $3 \times 3 \times 3$  subgrids were considered and the one showing the highest number of EOIs was selected as the ROI.

### **Second stage: Detection of ripples inside the ROI.**

- (a) *Beamforming inside the ROI:* A new and finer grid (0.75 cm between  $VS_{HF}$ ) was computed inside the selected cubic ROI, creating a volume of  $5 \times 5 \times 5$  points where new beamformer weights were calculated and time-series signals were obtained for each VSHF using the same procedure applied in the whole-head approach.
- (b) *Detection of EOIs:* EOI detection was performed for VSHF using the same algorithm explained in section 5.2.3. However, visual analysis of the selected segments revealed that the detection threshold of the algorithm was very restrictive and some of the events detected in

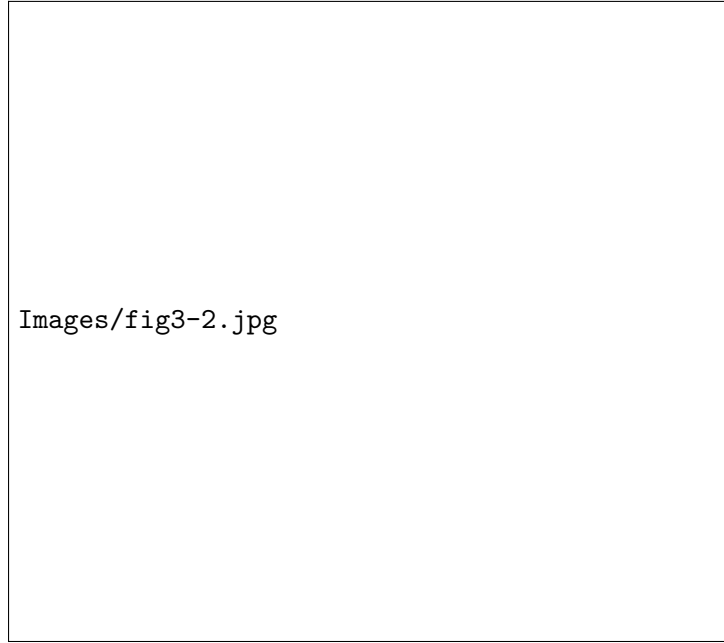


Figure 5.2: Schematic example of the overlapping conditions. If two events had common samples and if the length of the common samples, LOV, was higher to the half of the length of the first event L1 and the second event L2, then the both events were considered as overlapping events.

iEEG that were observable in  $VS_{HF}$  were not being selected as EOIs due to a lower SNR, and therefore, failed to detect a considerable number of visible events in MEG-VS. Consequently, to perform the selection of EOIs and the subsequent detection of ripples, several thresholds  $mean \pm factor_{SD} \cdot SD$  were evaluated by varying the  $factor_{SD}$  from 1.5 to 3 in steps of 0.25.

- (c) *Recognition of ripples among EOIs:* The recognition of ripples among the selected EOIs was performed using a similar algorithm to the second step explained in (Burnos et al., 2014), which discards EOIs elicited by other activity than oscillatory (Jacobs et al., 2012; Otsubo et al., 2008; Muthukumaraswamy, 2013). The assumption taken for this step was to define a HFO as a short-lived event with an isolated spectral peak at a distinct frequency (Crepon et al., 2010; Cho et al., 2012). Beamformer was computed from  $MEG_{WS}$  for each detected  $EOI \pm 0.25s$  and  $VS_{WS}$  was obtained as the product of the  $MEG_{WS}$  with the filter weights projecting the time-series along a unique dipole direction corresponding to the maximum variance as explained in subsection 5.2.3. The time-frequency response of the  $VS_{WS}$  was performed using the Stockwell Transform. An event was considered a ripple if its frequency response presented a clear distinguishable peak above 80Hz. To measure this, the following



Figure 5.3: Example of a ripple with a clear and distinguishable peak in high frequency and the selection of HiFP, Trough, LoFP in the PSD estimation at the maximum point of the envelope.

steps were computed:

- (1) The instantaneous power spectrum density (PSD) was obtained for the maximum point of the envelope (obtained by means of the Hilbert transform). An example of the computed time-frequency response and the corresponding PSD is observed in Figure 5.3.
- (2) From the PSD, three parameters were computed (see Figure 5.3):
  - (i) The high-frequency peak (*HiFP*) was selected as the spectral peak of a possible HFO. The minimum frequency of this peak is 80Hz and the maximum is 120Hz.
  - (ii) The *trough* was defined as the minimum point in the range between 40Hz and *HiFP*.
  - (iii) The low frequency peak (*LoFP*) was defined as the closest local maximum below the *trough*.

(3) The EOI under analysis was selected as a ripple if the following conditions were fulfilled:

$$\frac{Power(Trough)}{Power(HiFP)} < 0.8 \quad (5.2)$$

$$\frac{Power(HiFP)}{Power(LoFP)} > 0.5 \quad (5.3)$$

(d) *Whole grid analysis*: An additional feature was taken into account to discard ripples that appeared in just a few VS and isolated from their adjacent channels. All the detected ripples occurring at the same time segment (with a minimum of 50% of overlapping) were assigned to the same specific ripple event. The overlapping conditions are shown in Figure 5.2. The relative power of the ripple in one virtual sensor  $RP(VS_i)$  was computed as follows:

$$RP(VS_i) = \frac{P_{event}(VS_i) - P_{200s}(VS_i)}{P_{200s}(VS_i)} \quad (5.4)$$

where  $P_{event}$  is the power in the 80-120Hz band of the ripple event in the  $i^{th}$  VS and  $P_{200s}$  is the power of the whole 200s signal in the same frequency band in the  $i^{th}$  VS.

The energy of an event ( $E_r$ ) was then computed as the sum of the maximum relative power of each VS belonging to the ripple with respect to the sum of the relative power of all the VS in that same event:

$$E_r = 100 \cdot \frac{\sum_{n=1}^{nVS} RP(VS_n)}{\sum_{k=1}^1 25RP(VS_k)} \quad (5.5)$$

where nVS is the number of VS with a detected ripple. Once the  $E_r$  was calculated, the detected ripple was discarded if its value was not high enough. The energy threshold  $thres_{E_r}$  was defined with the purpose of discarding isolated events or with low energy and, thereby, obtaining a better performance of the algorithm. Several values for  $thres_{E_r}$  were considered from 0% to 100% in steps of 1%.

#### 5.2.4 Threshold selection: Precision/recall curves.

The evaluation of the performance of the current algorithm was done using iEEG signals as gold standard. Ripples iEEG were automatically detected with the time-frequency analysis

algorithm described in (Burnos et al., 2014). For each pair of values considered in both thresholds ( $factor_{SD}$  and  $thres_{Er}$ ) and for each automatically detected ripple in iEEG and MEG-VS, a co-occurring event was defined if these aforementioned ripples overlapped in time (see Figure 5.2). Each ripple event in iEEG was considered independently for each channel. In MEG-VS, all the virtual sensors containing an overlapped event (Figure 5.2) were considered as one individual event. This co-occurring ripple was considered a true positive (TP). A false positive (FP) was defined as a detected ripple in MEG-VS that was not detected in iEEG. Finally, a false negative (FN) was defined as a detected ripple in iEEG but not visible in MEG-VS. The recall (R), precision (P) and F1 score (F1) were computed as:

$$R = 100 \cdot \frac{TP}{TP + FN} \quad (5.6)$$

$$P = 100 \cdot \frac{TP}{TP + FP} \quad (5.7)$$

$$F1 = 2 \cdot \frac{P \cdot R}{P + R} \quad (5.8)$$

The F1 score measures the test accuracy, and can be interpreted as a weighted average of the precision and the recall. The influence of both thresholds on the discrimination of ripples from noise was evaluated by observing increases of recall or precision. To select the optimum threshold values, a leave-one-out procedure was used. The values of energy and SD threshold were computed as a function nine times, each one leaving one of the subjects out. For each of the curves, the Er and SD values that produced the higher F1 score were selected. The values selected for the classifier,  $factor_{SD}$  and  $thres_{Er}$  were selected using the median values for each one of the leave-one-out functions.

### 5.2.5 Detection and localization of ripples inside and outside the ROI

As mentioned before, the ROI was selected as the area with higher number of EOIs, and where the VS belonging to the ROI were expected to be more active. In order to show this hypothesis, once the automatic selection was performed and the remaining noisy events were discarded, the comparison between the number of detected ripples inside and outside the ROI was performed.

For each patient, the contralateral hemisphere was selected as the area outside the ROI and the same automatic procedure to detect ripples was applied. Results were compared between the two regions.

## 5.3 Results

### 5.3.1 Detection of the region of interest

To evaluate the selected ROIs resulting from the first stage in the volume reconstruction model, the coordinates of the central virtual sensor were normalized into MNI space using brainstorm software (Figure 5.4) and the gyrus and lobes were obtained for this position in the normalized atlas (Table 5.2). The central VS of the 9 subjects matched the lobe where seizures had been generated (Table 5.1).

### 5.3.2 Threshold selection inside the ROI

To select the values of  $factor_{SD}$  and  $thres_{Er}$  as the trade-off between precision and recall, the detection in iEEG and MEG-VS was compared when varying these two parameters, selecting the values that produced higher F1 score, which is, maximizing both precision and recall. To obtain these values, a leave-one-out cross validation approach was used, in which each subject was left out and the selected values were calculated with the rest. The results of the selected values for  $factor_{SD}$  and  $thres_{Er}$  are shown in Table 5.3. The obtained median values were used as the final selected values: 2.25 for  $factor_{SD}$  and 17.75% for  $thres_{Er}$ . The averaged precision/recall and F1 score curves for all the subjects are shown in Figure 5.5. A decrease of  $factor_{SD}$  allowed to detect higher number of ripples increasing recall but with the risk of introducing false positive events (decreasing precision) with less energy that would appear simultaneously in a lower number of virtual sensors. This is why a similar effect was found with  $thres_{Er}$ : higher precision but lower recall with higher values.



Figure 5.4: Example of localization of the middle virtual sensor (in red) in the warped anatomy and the posterior MNI transformation.

### 5.3.3 Automatic detection

The automatic detection was applied to the 9 subjects using the selected threshold values. The values of recall and precision were  $68.9 \pm 0.8$  and  $79.2 \pm 1.5$ , respectively (*mean*  $\pm$  *SD* of all subjects). The resulting F1 score was  $73.7 \pm 0.6$  (TP:  $25.2 \pm 10.0$ ; FN:  $11.4 \pm 4.7$ ; FP:  $6.6 \pm 2.5$ ). The average number of detected events was  $31.8 \pm 12.5$ , which produced a rate of ripples per minute of  $9.5 \pm 3.7$ , similar to the value of  $6.7 \pm 4.8$  obtained by visual inspection in (van Klink et al., 2016) with MEG. The number of detected ripples in iEEG was  $36.7 \pm 14.7$ , producing a rate of  $11.0 \pm 4.4$  ripples per minute. The detector was evaluated to ensure better-than-chance performance (Andrzejak et al., 2009) using the Poisson random probability distribution proposed in (Snyder et al., 2008). Precision, Recall and F1 score were significantly lower ( $p\text{-value} < 0.0001$ ) for the random distribution.

Figure 5.6 shows, as an example, MEG-VS time-domain signals for Patient 1 after applying the beamforming algorithm. The same time segments of the iEEG channel with higher ripple rate and the 9 closest scalp-MEG channels are also shown. Ripples that are unrecognizable in scalp-MEG are observed in MEG-VS, and occur simultaneously in iEEG signals. Furthermore,

the different possible situations (TP, FP, FN) of automatic detection of ripples in MEG and iEEG are shown. Table 5.2 summarizes the performance of the automatic algorithm for each patient along with the global performance using the aforementioned thresholds.

Table 5.2: Brodmann Areas and lobes of the ROI and detection of ripples in MEG-VS compared to iEEG (R: right, L: left)

Patient	Gyrus/Lobe	Ripples MEG-VS	Ripples iEEG	TP	FN	FP	Recall	Precision	F1score
1	Fusiform/Occipital (L)	44	51	35	16	9	68.6	79.5	73.7
2	Middle Temporal/Temporal (R)	48	55	38	17	10	69.1	79.2	73.8
3	Fusiform/Temporal (R)	54	63	43	20	11	68.2	79.6	73.5
4	Middle Temporal/Temporal (R)	26	31	21	10	5	67.7	80.8	73.7
5	Middle Occipital/Occipital (L)	23	26	18	8	5	69.2	78.3	73.5
6	Superior Temporal/Temporal (L)	17	19	13	6	4	68.4	76.5	72.2
7	Sub-gyral/Temporal (R)	22	24	17	7	5	70.8	77.3	73.9
8	Middle Temporal/Temporal (R)	25	29	20	9	5	69.0	80.0	74.1
9	Sub-gyral/Temporal (R)	27	32	22	10	5	68.8	81.5	74.6
Mean		31.8	36.7	25.2	11.4	6.56	68.9	79.2	73.7
SD		12.5	14.7	10.0	4.7	2.50	0.8	1.5	0.6

Note that the automated detection used for iEEG signals was based in the automatic algorithm developed in (Burnos et al., 2014), where the thresholds were trained heuristically to optimize sensitivity/specificity only in a single patient. In the current work, visual inspection of iEEG revealed that some of the events that fulfilled the Stockwell conditions were discarded in the first stage because they did not reach the threshold of  $mean + 3 \cdot SD$ . In addition, the same authors concluded that these three times of SD could be too restrictive and high. Table 5.5 shows changes in precision, recall, and F1 score values produced when the iEEG threshold was

Table 5.3: Optimum SD and Energy for each LOO iteration

Loo Patient	Optimum SD	Optimum $E_{HFO}(\%)$
1	2.25	17.75
2	2.25	21.21
3	1.75	13.31
4	2.25	20.21
5	2.0	14.79
6	2.25	17.75
7	2.25	17.75
8	2.25	17.75
9	2.25	20.21
Median	2.25	17.75



Table 5.4: Number of ripples, mean number of MEG-VS in each ripple for all the subjects and percentage of detected ripples inside the most active region. The evaluation outside the ROI was performed placing a grid of the same size and number of channels in the contralateral hemisphere where the ROI was placed.

Patient	No. of HFOs		No. of VS/HFO (mean $\pm$ sd))		% Detected ripples	
	inside ROI	outside ROI	insideROI	outsideROI	insideROI	outsideROI
1	44	21	14.6 $\pm$ 10.1	17.7 $\pm$ 6.4	42.5	14.6
2	48	15	18.2 $\pm$ 8.7	9.2 $\pm$ 4.1	37.0	16.4
3	54	21	21.7 $\pm$ 16.8	12.1 $\pm$ 7.7	37.9	13.4
4	26	14	22.6 $\pm$ 8.6	15.5 $\pm$ 8.7	34.0	9.1
5	23	7	13.1 $\pm$ 6.3	11.4 $\pm$ 6.5	32.0	24.4
6	17	11	24.7 $\pm$ 11.5	19.0 $\pm$ 9.6	28.8	19.3
7	22	8	14.9 $\pm$ 6.7	14.7 $\pm$ 7.8	44.7	22.9
8	25	13	16.3 $\pm$ 7.2	18.5 $\pm$ 5.3	35.9	17.2
9	27	11	20.3 $\pm$ 7.9	15.6 $\pm$ 11.2	30.6	16.6
Mean	31.8	13.4	18.4	12.6	35.9	17.1
SD	13.2	5.0	4.0	3.8	5.3	4.7

lowered to 2.5 and 2 times of SD. For this step, MEG-VS threshold values stayed invariant. An improvement in precision and F1 score values were produced when the iEEG threshold was lowered to  $2.5 \cdot SD$ , and only slightly lower recall values were observed. When the threshold was further decreased to  $2 \cdot SD$ , precision increased a bit but recall decreased more, producing a lower F1 score. These results suggested that iEEG threshold was fixed to be too restrictive for the data presented in this study and a slight lower value would have been more appropriate.

#### 5.3.4 Detection and Localization of ripples inside and outside the ROI

The average number of detected ripples inside the ROI was  $31.8 \pm 13.2$  and this value decreased to  $13.4 \pm 5.0$  when computed outside the ROI (*mean  $\pm$  SD*). The number of VSWS involving each ripple event was also computed. An average number of  $18.4 \pm 4.0$  VS were involved in each ripple event inside the ROI, whereas this value was slightly lower outside the ROI which showed an average of  $12.6 \pm 3.8$  VS. The differences (inside and outside the ROI) between the number of detected ripples and the average number of virtual sensors were statically significant (paired T-tests, significance set to 0.05) with probability values of 0.002 and 0.02, respectively. Table 5.4 shows the number of detected ripples outside the ROI and the mean number of VS involving each ripple for each patient.

The localization maps inside and outside the ROI for Patient 1 are shown in Figure 5.7. These maps measure the number of times that a specific virtual sensor was associated to a ripple. Figure 5.8 shows the grid inside and outside in slices (of the z-plane) for the nine subjects. These figures suggested that specific VS appeared clustered, close to each other and involved in a high number of ripples inside the ROI, showing a more focalized localization map than outside the ROI. In order to quantify this effect, the percentage of detected ripples for the most active region inside and outside the ROI is shown in Table 5.4. To compute this score, the VS showing the highest number of ripples and its six closest neighbors were selected for each subject. The ratio of the average number of ripples detected in seven clustered VS to the number of detected ripples was then computed. As expected, the percentage of ripples involved in the most active region inside the ROI was significantly higher ( $p\text{-value} < 0.001$ ) than outside the ROI.

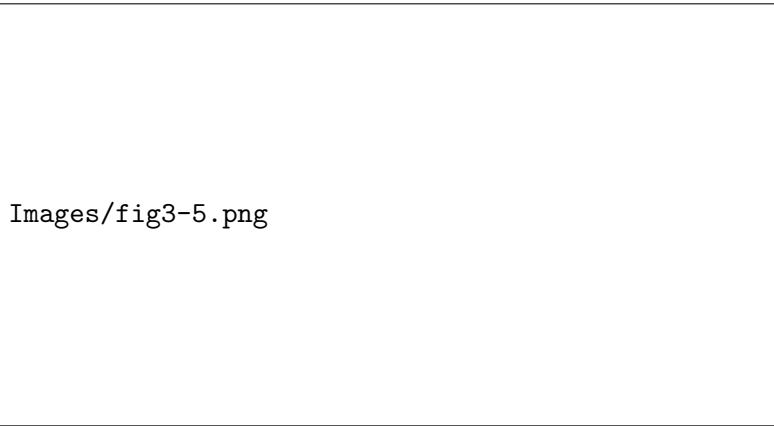


Figure 5.5: Averaged performance curves. a) Precision-Recall curves for all the tested factorSD thresholds. Each value correspond to a pair of  $factor_{SD}$  and  $thres_{Er}$ . b) F1score – Energy for all the tested thresholds. c) and d) show the recall and precision curves with respect to the energy threshold. The optimum  $factor_{SD}$  and  $thres_{Er}$  values were 2.25 and 17.75% respectively.

## 5.4 Discussion

### 5.4.1 Main contribution of the study

There are only a few studies that identify interictal epileptic HFOs using MEG in the time domain. In (von Ellenrieder et al., 2016) a semi-automatic approach was proposed to detect fast oscillations (40 Hz to 160 Hz) using MEG where the proposed algorithm was adjusted to have high sensitivity, discarding false positives by human intervention (two experts). Visual detection

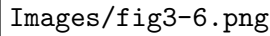


Figure 5.6: Simultaneous detection of TP, FP and FN in MEG, iEEG and MEG-VS signals. MEG VS channels shown are placed on a tridimensional star-shaped configuration. MEG channels shown belong to the nearest closest scalp area where the ROI was found. Green events correspond to a detected HFO in iEEG and MEG-VS (TP). Red events correspond to a detected HFO in MEG-VS but not visible in iEEG (FP). Pink events correspond to a detected HFO in iEEG but not visible in MEG-VS (FN). Non-labeled visible events did not meet the first conditions (EOI detection).

of HFOs in the temporal domain is a time-consuming and highly subjective procedure. The current work represents the first study proposing an automatic approach that takes into account the time-frequency characteristics of the high-frequency events to detect ripples, while discarding other high-frequency noise events. Moreover, von Ellenrieder et al. performed the detection of ripples at the sensor level and consequently they obtained low detection rates of ripples due to the low SNR of the signals at the scalp level. Thanks to a beamformer-based spatial filtering, a high amount of high-frequency noise reduction was achieved, allowing to discern ripples that could not be identified in scalp MEG (Figure 5.6). The remaining noisy events were discarded using a two-step algorithm based on thresholds whose values were selected to maximize the

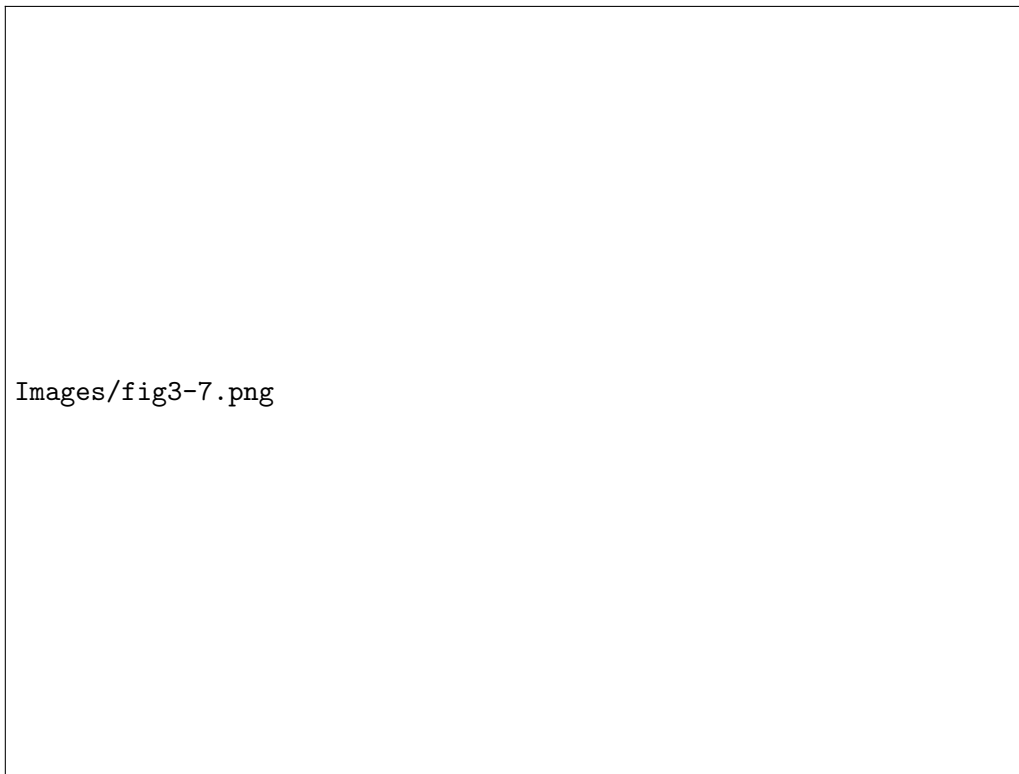


Figure 5.7: Localization maps for the number of detected ripples a) inside the ROI and b) outside the ROI, on the contralateral hemisphere for Patient 1.

correspondence with ripple events in iEEG, the current gold standard. However, beamforming algorithms can be computationally consuming, and a hybrid approach combining algorithms that detect some events at the sensor level (such as the one proposed by von Ellenrieder et al. (von Ellenrieder et al., 2016)) and algorithms that are focused in the source level could provide a good compromise between computation time and detection accuracy in MEG signals.

Furthermore, the whole-head beamformer step allowed to choose the ROI without relying on epileptic spikes. The exact relationship between IEDs and HFOs remains unclear, and it is unknown whether HFOs are produced by the same generators as IEDs or not (Jacobs et al., 2008). Interictal HFOs have proven to be reliable markers of the seizure onset zone, and better than epileptic spikes (Jacobs et al., 2010, 2008). In (van Klink et al., 2016), the authors defined a ROI based on the location of the spikes in the physical MEG sensors, but this ROI was inaccurate in two out of twelve patients. In the current study, a finer VS grid was used and fixed to the area where most high-frequency events took place, minimizing the possibilities of missing ripples occurring inside the volume of the grid.



Figure 5.8: Localization maps in slices of the number of detected ripples for all subjects for a) inside the ROI and b) outside the ROI. The colormap measures the number of times that a VS appeared in a ripple.

#### 5.4.2 Threshold selection and performance analysis

To the best of the author’s knowledge, this is the first study that compares the simultaneous detection in time of ripples in noninvasive signals (MEG) against iEEG, the current gold standard for the detection of HFOs. Zelmann et al. (Zelmann et al., 2014) had previously analyzed the spatial distribution between HFOs in iEEG and scalp EEG. In their study, the poor spatial correlation found between the two modalities was justified by the low number of channels (19 channel EEG-system), the distortion produced by the electrical conductivity of the surrounding tissues and the low SNR of the signals. The use of systems with a higher number of channels, and less influenced by the conductive properties of the skull such as MEG systems, and methods for improving the SNR of the signals, such as beamforming, provides better results in terms of

localization. The automatic analysis was performed in iEEG and the values for two thresholds were selected for MEG-VS to achieve a maximum F1 score, in other words, the weighted average of precision and recall measures. Unfortunately, the exact location of iEEG in the head or the MRI of the subjects was unavailable for this study. Furthermore, the direct comparison of the recorded oscillations between these two signal acquisition methods is still uncertain. On the one hand, iEEG is an invasive technique that records electrical activity inside the head yielding a high SNR and consequently can detect events that could remain hidden in MEG signals, even after beamforming. Although there is no previous study evaluating HFOs in MEG and iEEG simultaneously in time, there are studies comparing IEDs simultaneous detection and their values of recall (or sensitivity) in MEG-VS detection with respect to iEEG which were comparable to the results of the current study, around 60-80% (Bouet et al., 2012; Huiskamp et al., 2010; Nowak et al., 2009). While a more exhaustive comparison between the detection of IEDs and HFOs with both techniques under the same conditions should be carried out, the results on the detection should be comparable because IEDs and ripples have similar SNR values at their respective frequency bands (von Ellenrieder et al., 2012), and because signals are equally attenuated at all frequencies of interest (Zelmann et al., 2014). On the other hand, MEG can often provide additional and useful information mainly because of its whole-head coverage while iEEG recordings usually only provide a locally limited neurophysiological picture (Muthukumaraswamy, 2013). The number of depth electrodes for this study covered a small region of the brain. For this reason, there is still some uncertainty regarding the FP ripples because they could be either noise being incorrectly detected as HFOs or actual ripples not recorded by iEEG.

Table 5.5: Average values of performance (Precision, Recall and F1 score) and number of Co-detected Events, Detected Events only in iEEG, and detected events only in MEG when iEEG SD threshold was lowered. The duration of the EOI was set to  $0.5 \cdot (mean + 3 \cdot SD)$  for the three evaluated thresholds

	iEEG SD	3.0	2.5	2.0
Co-detected Events		25.2	26.2	26.4
Detected Events in iEEG		11.4	12.0	13.5
Detected events in MEG		6.7	5.6	5.4
Recall		68.9	71.2	70.1
Precision		79.2	82.4	83.0
F1 score		73.7	76.4	76.0

The automatic detection of HFOs in invasive records is still an open field of study (Liu et al., 2016; Burnos et al., 2014). For all these reasons, using the iEEG as gold standard implies the acceptance of the detection provided by this technique. Table 5.5 shows that changing the SD threshold in the iEEG automatic detection produced variations in the number of co-detected events, suggesting that the threshold proposed in (Burnos et al., 2014) might be fairly restrictive depending on the characteristics of the signals. The abovementioned selection of values for both thresholds considered the highest values of F1 scores, but they could be selected different depending on the purpose of the detection: The values of  $factor_{SD}$  and  $thres_{Er}$  could be decreased to maximize recall (higher than 80%) and to detect the highest possible number of ripples or, conversely, they could be increased to maximize precision (around 95%) and ensure almost totally that the detected events were equally visible in iEEG and MEG-VS. Nonetheless, more efforts should be directed to provide a reliable detection of ripples in MEG-VS by observing other characteristics of the actual signals (such as HFOs onsets or connectivity between VS) or taking into account post-surgical outcomes (which were not available in this database).

### 5.4.3 Evaluation of ripples inside and outside the ROI

An automatic selection of the area that showed the highest number of EOIs was performed to circumscribe the detection of ripples to a volume of approximately  $9cm^3$ . This area agreed with the affected zone targeted by clinicians (Tables 5.1 and 5.2). The HFO detection algorithm was applied to the same volume in the contralateral hemisphere with the purpose of comparing the number of ripples and the pattern drawn by VSWS involved (Figures 5.6 and 5.7). In general, a group of VS that were detected simultaneously in different ripples produced a focalized map inside the ROI. Although this information was still insufficient to provide a reliable localization of the area generating pathological HFOs because of the lack of precise clinical information, it could be inferred that the oscillations were mostly generated by a common focus and this provides a general idea of the area where the ripples appeared. It is important to remark that although the automatic detection algorithm use a ROI to detect ripples, these can be mapped a posteriori throughout the head, using the temporal information about the detected ripple segments.

The proposed algorithm also detected some ripples outside the ROI but the number of events was significantly lower and involved fewer VS. There is still uncertainty between the differential characteristics and mechanisms of pathological and physiological ripples (Jefferys et al., 2012). Whether all the detected events were actually physiological, pathological, or noise cannot be definitely be demonstrated, but the detected ripples outside the ROI presented lower values of energy, which is a characteristic of physiological HFOs (Matsumoto et al., 2013). Moreover, the pattern of these oscillations appeared more scattered throughout the volume, indicating that these oscillations were not generated by a common area or focus. This finding is in correspondence to the observations with animal studies indicating that the areas generating physiological HFOs appeared more extended (Chrobak and Buzsáki, 1996) than the areas generating pathological HFOs, that are smaller brain regions on the order of cubic millimeters (Bragin et al., 2002). The results from Zelman et al. (2014) suggested that it is possible to measure the activity from small cortical regions at the scalp level. This could be explained by the solid angled concept introduced by Gloor (1985). These measures should be comparable with those obtained with subdural grid contacts, always taking into account that the spatial resolution of the technique should be high.

#### 5.4.4 Limitations of the study and further work

Beamformer virtual sensors allowed the detection of high-frequency activity otherwise not observable by the physical sensors. The main purpose of this study was to automatically detect ripple events in MEG and discern them from noise by analyzing time-frequency characteristics using iEEG recordings to adjust and validate the algorithm. However, due to the lack of spatial location of intracranial electrodes, only a full-scale spatial validation of the detected ripples could be performed.

The spatial resolution of the reconstructed virtual sensors is limited and depends on the depth, position and orientation of the sources, the SNR of the raw data, and the geometry of the head (Hillebrand A, 2002). For all of these reasons, beamformer-based methods are not suitable for clinical application yet for the localization of the epileptic focus through ripples and the replacement of invasive techniques. However, the automatic detection in non-invasive techniques



could be useful to guide the implantation of intracranial electrodes of subdural grids as it has been demonstrated that HFOs delimitate the affected area better than IEDs (Jacobs et al., 2008).

More efforts should be put to increase the SNR of the signals, and in this sense independent component analysis has proven to be effective improving the spatial localization of beamformer spatial filters (Fatima et al., 2013). Ultra-low-noise EEG/MEG techniques (Fedele et al., 2015) are promising in the noninvasive detection of HFOs. Moreover, using the actual MRI of each subject to compute the head model would produce better results in the localization of the epileptic sources. A complete analysis comparing MEG with intracranial recordings should also include the position of implantation of the subdural electrodes. Furthermore, using MEG systems with more channels and higher frequency rates would provide a better spatial and temporal resolution. Several studies have found that fast ripples have shown to be more correlated with the seizure onset zone and presumably highly epileptogenic (Van Klink et al., 2014; Zijlmans et al., 2012; Haegelen et al., 2013; Jacobs et al., 2008) than ripples. Due to the sampling rate limitation, this study only analyzed ripples up to 120Hz. However, the automatic detection algorithm does not depend on the sampling rate and can be used to detect HFOs of higher frequency content acquired at higher rates. This would allow evaluating the differences in localization of ripples and fast ripples and their relationship with the seizure onset zone. Furthermore, fast ripples would likely be downsampled to appear at lower harmonics, being able to detect them, but not to classify them between ripples or fast-ripples. Moreover, the study of ripples by non-invasive methods can also help to lateralize the epileptic focus in secondary bilateral synchrony (Pizzo et al., 2016), delimitate the seizure onset zone in patients where fast ripples are not visible (Van Klink et al., 2014), and in general, provide a better delimitation of the affected area than IEDs (Jacobs et al., 2008). Moreover, the detection of this area with non-invasive techniques can provide relevant information to guide the implantation of intracranial electrodes and for surgical treatment (von Ellenrieder et al., 2016). It is important to highlight that computation time increases with frequency and spatial resolution. These algorithms should be implemented efficiently minimizing the computation time to be suitable for clinical analysis.

Finally, improving the spatial and temporal resolution would also allow to detect HFOs and determine the SOZ in the whole head using automated methods and clustering analysis, com-

puting different features such as density, connectivity, peak frequency, power, amplitude (Modur and Miocinovic, 2015), or spectral entropy (Liu et al., 2016). The automatic detection algorithm presented in this study would also be useful to extend these studies, which are currently limited for iEEG, would exploit the advantage of the whole head coverage of MEG allowing the assessment of the neural mechanisms of epilepsy as well as reducing invasiveness in clinical patients. The comparison between the areas of the brain generating HFOs and IEDs in epilepsy and its relationship would also be an interesting field of study. Moreover, a careful analysis of the whole brain volume could allow to understand the areas involved in the HFO generation, the propagation of this activity and how they are related with the epileptogenic networks.

## 5.5 Conclusion

High-frequency oscillations are promising biomarkers for epilepsy. Several studies detect them automatically in intracranial recordings, but there are few studies evaluating these oscillations in noninvasive signals. To the authors' knowledge, this is the first study dealing with full automatic detection of ripples in MEG in the time domain taking into account the time-frequency characteristics of the events through the whole signal spectrum. Moreover, these ripples corresponded to the clinically expected epileptogenic area. The detection was compared with intracranial EEG recordings, demonstrating that the identification of ripples in MEG is feasible. The noninvasive study of HFOs is an interesting field of study that would allow to evaluate HFO mechanisms in larger groups of epileptic patients and also in healthy subjects to discern the differences between pathologic and physiologic fast oscillations.

## 5.6 Acknowledgments

CIBER-BBN is an initiative of the Instituto de Salud Carlos III, Spain. This work has been partially supported by the Ministry of Economy and Competitiveness, Spain, under contract DPI2014-59049-R and the Ministry of Education, Culture and Sports FPU12/05631. We thank Sylvain Baillet and its group NeuroSpeed (Montreal Neurological Institute, McGill University) for the help and comments during the course of this research that greatly improved this work.

# Chapter 6

## Conclusion

### 6.1 Summary

Magnetoencephalography is a noninvasive technique that provides excellent temporal resolution and a whole-head coverage that allows the spatial mapping of cerebral sources. These characteristics make MEG an appropriate technique to localize the epileptogenic zone (EZ) in the preoperative evaluation of pharmacoresistant epilepsy. There is great interest in using interictal biomarkers to determine the EZ because these can occur more frequently than seizures (Staba et al., 2014) and reduce the discomfort of the patient during the recordings.

Presurgical evaluation with MEG can guide the placement of invasive electrodes, the current gold standard in the clinical practice, and even supply sufficient information for a surgical intervention without invasive recordings, reducing invasiveness, discomfort, and cost of the presurgical epilepsy diagnosis (Aydin et al., 2015). However, MEG signals have low signal-to-noise ratio compared with intracranial EEG and can sometimes be contaminated by noise that mask or distort the brain activity. This may prevent the detection and the localization with interictal epileptiform discharges (IEDs) and high frequency oscillations (HFOs), two important biomarkers used in the preoperative evaluation of epilepsy.

To achieve the main goal of this thesis, namely the development and validation of methods for noninvasive localization of interictal biomarkers with MEG, its signal-to-noise ratio must

improve. The reduction of two kinds of interference was aimed: metallic artifacts that affect exclusively MEG recordings and mask the activity of IEDs; and the high-frequency noise, produced mainly by muscular interferences that mask HFO activity. Considering the large number of MEG channels and the long time of the recordings, reducing noise and marking events manually is a time-consuming task. The algorithms presented in this thesis provide automatic solutions aimed at the reduction of interferences and, the detection of HFOs.

In chapter 3, an automatic BSS-based algorithm to reduce metallic interference was developed and validated using simulated and real signals (Migliorelli et al., 2015). Three methods were evaluated: AMUSE, a second-order BSS technique; and INFOMAX and FastICA, based on high-order statistics. To objectively evaluate the effectiveness of BSS and the subsequent interference reduction, simulated signals consisting in real artifact-free data mixed with real metallic artifacts were generated. Subsequently, an automatic detection of the artifactual components was proposed, exploiting the known characteristics of metallic-related interferences. Results indicated that AMUSE performed better when recovering brain activity and allowed an effective removal of artifactual components.

In chapter 4 the influence of metallic artifact filtering using the previously developed algorithm was evaluated in the source localization of IEDs in patients with refractory focal epilepsy (Migliorelli et al., 2016). In this study, a comparison between the resulting positions of equivalent current dipoles (ECDs) produced by IEDs was performed: without removing metallic interference, rejecting only channels with large metallic artifacts and after BSS-based reduction. The results showed that a significant reduction on dispersion was achieved using the BSS-based reduction procedure, yielding feasible locations of ECDs in contrast to the other two approaches.

In chapter 5 an algorithm for the automatic detection of epileptic ripples in MEG using beamformer-based virtual sensors was developed (Migliorelli et al., 2017b). The automatic detection of ripples was performed using a two-stage approach. In the first step, beamforming was applied to the whole head to determine a region of interest where more high frequency activity was taking place. In the second step, the automatic detection of ripples was performed using the time-frequency characteristics of these oscillations. The performance of the algorithm was evaluated using intracranial EEG recordings as gold standard. Furthermore, the number of events that

were detected inside the region of interest were significantly higher than the number of events found outside.

The main conclusions of the different studies and its relationship with the objective of the thesis are summarized in the following section.

## 6.2 Main conclusions

The main objective of this thesis was to develop and validate methods for the effective non-invasive localization of interictal epileptogenic biomarkers with magnetoencephalography. Two automatic algorithms were developed: a BSS-based procedure to reduce metallic interference present in MEG signals coming from diverse sources; and a method to reduce high frequency interferences and to detect ripples in non-invasive data. Both algorithms were developed using freely available signal analysis tools and methods. Specifically, the toolboxes that were used to achieve this aim were the Fieldtrip toolbox (Oostenveld et al., 2011), Brainstorm software (Tadel et al., 2011), ICALAB (Cichocki and Amari, 2003) and the openly-available S-transform algorithm (Stockwell et al., 1996).

Metallic artifacts can hugely distort MEG signals and mask the brain activity partially or even completely. The proposed algorithm in chapter 3 extracted independent components (ICs) and automatically selected those ones that were artifact-related (Migliorelli et al., 2015). To do so, two characteristics were taken into account both related to metallic artifact nature: the first one measured the frequency spectrum of the IC and the second the regularity of the signal using the sample entropy. Furthermore, an additional condition related to the region where this component projected was taken into account. To validate the automatic algorithm for metallic reduction presented in, simulated signals were generated, consisting of clean recordings to which metallic artifacts were added. The use of simulated signals allowed to objectively quantify the amount of noise reduction achieved by the algorithm using three different approaches: AMUSE, INFOMAX and FastICA. The algorithm presented good performance with the AMUSE technique and was able to remove the metallic interference coming from different sources, projecting in diverse locations and with various levels of intensity.

AMUSE is a second-order statistics BSS method while FastICA and INFOMAX are high-order statistics techniques. AMUSE showed considerably lower errors than the HOS techniques. INFOMAX was able to decompose artifactual ICs from those related to brain activity but part of the cerebral signals remained mixed with the metallic components. FastICA did not manage to generate a valid decomposition of the ICs, even after ensuring convergence with the stabilizer provided by (Hyvärinen, 1999). The reason behind this behaviour is that FastICA decomposes signals by measuring their differences with a normal distribution. For this reason it is very effective dealing with supergaussian sources, such as cardiac and ocular interferences, but when working with subgaussian and specially with gaussian signals which is the case of metallic interferences, the algorithm is not able to separate them from cerebral signals, that present similar distributions.

Other methods that deal with metallic interference are the so-called signal space separation (SSS) (Taulu et al., 2004) and temporal signal space separation (tSSS) (Taulu and Simola, 2006). However, these algorithms are provided by a registered software only available for Elekta-Neuromag systems (Gonzalez-Moreno et al., 2014). The developed BSS-based approach is based on standard libraries that can be used in any MEG system available. Moreover, while tSSS algorithm was evaluated in the removal of metallic interference in previous studies, (Hillebrand et al., 2013; Song et al., 2009; Alexopoulos, 2013) these studies did not evaluate the noise reduction of metallic interference quantitatively. Furthermore, in (Gonzalez-Moreno et al., 2014) a higher signal-to-noise ratio improvement was observed when applying BSS techniques combined with SSS and tSSS methods in comparison of applying these techniques alone, suggesting that after applying SSS and tSSS techniques not all the noise was successfully removed and BSS algorithms were effective in removing the remaining interferences.

The influence of metallic interference and the subsequent reduction with the developed algorithm was tested in patients with pharmacoresistant epilepsy in (Migliorelli et al., 2016). All of the patients had some kind of non-removable device that produced metallic interferences: dental orthodontics, implanted subdural grids, vagus nerve stimulators, or ventricular bypass valves. For these patients, IEDs were detected in the raw recordings by three different experts and the estimation of the ECDs was performed in three different scenarios: without removing the interference, discarding the most affected channels, and applying the automatic removal

procedure. For the three scenarios several measures were used to evaluate the ECD estimation: the confidence volume, the distribution of the dipoles at the onset site, and the running distance of the path followed by dipoles associated to each IED.

In all the subjects, using the BSS-based approach produced smaller confidence volume values for the IED detection, suggesting that each of the computed dipoles and the obtained models were more plausible. Furthermore, the dispersion of the locations of the selected IEDs was measured. Using the automatic BSS technique, the dipoles showed significantly lower dispersion values than with the other proposed approaches, providing a better delineation of the irritative zone, which is the area generating IEDs. Finally, a distance measure allowed to observe the improvement on the stability of the dipolar sources and therefore a more reasonable association with the discharges produced by the epileptic tissue.

In addition to the detection of IEDs, and in line with the main objective, the thesis tackled the detection of high-frequency oscillations in MEG signals. These oscillations often appear masked by the high-frequency activity. In chapter 5, an algorithm was proposed based on spatial filtering beamforming to reduce very noticeably the high-frequency noise, allowing the visual observation of ripples that could not be identified in scalp MEG. Furthermore, the algorithm allowed to automatically detect ripples and discard other noisy events just by using a two-step procedure based on thresholds. The validation of the algorithm was performed using the time-domain information provided by intracranial electroencephalographic recordings (iEEG), the current gold standard. It is important to remark that the automatic detection of HFOs in iEEG is still an open field of study, and that MEG and iEEG are not supposed to record exactly the same type of cerebral activity. While iEEG provides an excellent spatial resolution in which electrodes are implanted, MEG can provide a whole-head image of the network areas that are activated during high-frequency epileptogenic activity.

The results showed that the proposed automatic selection of the area generating most events of interest agreed with the affected zone targeted by clinicians. Moreover, the virtual sensors showing higher ripple activity inside this area appeared focalized in comparison with its contralateral lobe. This finding is in correspondence with the observations of other studies that suggest that the areas producing pathological ripples are less extended than the areas generating

physiological HFOs (Chrobak and Buzsáki, 1996; Bragin et al., 2002). Furthermore, although the automatic detection algorithm uses a delimited region to detect ripples, this is not a limitation of the method because once these are detected, they can be mapped *a posteriori* throughout the head in order to observe the brain networks activated during high frequency epileptogenic activity.

Finally, these findings were published in high-impact journals and they are part of this compendium of publications. In addition, the preliminary studies on the removal of metallic interference and on the detection of high-frequency oscillations were published in the 35<sup>th</sup> Annual International Conference of the IEEE Engineering in Medicine and Biology Society (Migliorelli et al., 2013) and in the International Conference of Neurorehabilitation (Migliorelli et al., 2017a) respectively. Therefore, it can be concluded that the specific objectives raised in this thesis: (I) to develop algorithms, using freely-available signal analysis toolboxes, (II) to compare the performance of different BSS algorithms in the reduction of metallic interference, (III) to reduce metallic artifacts in MEG recordings automatically using blind source separation techniques, (IV) to evaluate the influence of metallic interference in the localization of interictal epileptiform discharges, (V) to reduce high-frequency noise to detect high-frequency oscillations in MEG signals, (VI) to develop an automatic method to detect high-frequency oscillations in MEG signals, and to compare its detection with intracranial recordings, (VII) to localize the areas generating pathologic high frequency oscillations automatically, and (VIII) to publish the obtained results and conclusions in high-impact journals and conferences; were accomplished allowing the fulfillment of the main objective of this thesis: to develop and validate methods for the effective noninvasive localization of interictal epileptogenic biomarkers with magnetoencephalography.

### 6.3 Main contributions

The original contributions provided by the compendium of publications of this thesis are:

- The definition of a novel algorithm, and its validation with simulated signals to remove metallic interference from MEG recordings in a fully automated fashion. This algorithm was developed using freely available toolboxes and methods and can be used on any MEG



system.

- The evaluation of the effects of the automatic filtering procedure in the detection of IEDs and the estimation of ECDs of patients with focal refractory epilepsy. The reduction of metallic interference in this kind of patients is essential, because the purpose of MEG is to provide a reliable detection of the areas producing epileptic activity, but there is a high number of patients with irremovable metallic devices (metallic intracerebral electrodes, vagal stimulators or, in younger patients, dental orthodontics) that distort the signals and produce noneffective localization of the IEDs generators.
- The definition of a novel algorithm, and its validation with intracranial recordings, to reduce high-frequency noise and to automatically detect HFOs, a promising interictal biomarker of epilepsy strongly linked to the epileptogenic zone. To date, this is the only fully-automatic algorithm that detect these oscillations at the source level in noninvasive recordings.
- The previous contributions allow an improved noninvasive detection and localization of interictal epileptic biomarkers, which can help in the delimitation of the epileptogenic zone and guide the placement of intracranial electrodes, or even to determine these areas without additional invasive recordings. As a consequence of this improved detection, and given that interictal biomarkers are much more frequent and easy to record than ictal episodes, the presurgical evaluation process can be more comfortable for the patient.

## 6.4 Future Work

The work developed in this thesis open new possibilities in the brain research line of the *BIOsignal Analysis for Rehabilitation and Therapy Research Group (BIOART)* to which the candidate belongs. Some of the most interesting further possibilities are the following:

- The growing use of brain stimulation in research and clinical applications reflects its capabilities to modulate brain function in ways not feasible with other techniques (Peterchev et al., 2012). However, large artifacts can appear in MEG and EEG recordings when used

simultaneously with this technique (Oswal et al., 2016; Haumann et al., 2016). The BSS-based automatic algorithm for the reduction of metallic interference can be useful to deal with this source of artifacts and provide new solutions to observe the brain activity that can stay masked behind large sources of interference.

- The improvement of the beamformer-based algorithm for the detection of HFOs in MEG by using time-frequency characteristics and advanced clustering methods (Liu et al., 2016) in the whole-head virtual sensors would allow to identify the epileptogenic zone in an automatic, accurate, and efficient manner. This, in turn, would allow to characterize the spatial, frequency, and temporal distribution of the high-frequency activity.
- Increased efforts should be put to improve the SNR of the noninvasive cerebral signals, and in this sense independent component analysis has proven to be effective in improving the spatial localization of beamformer spatial filters (Fatima et al., 2013). These techniques could be combined in order to improve the localization of HFOs and IEDs.
- Due to the sampling rate limitation of the available MEG database, the beamformer-based automatic detection algorithm only evaluated ripples up to 120Hz. However, the algorithm does not depend on the sampling rate and can be used to detect higher frequency HFOs content if signals are acquired at higher rates. Several studies have found that fast ripples have shown to be more correlated with the seizure onset zone, and presumably more epileptogenic (Jacobs et al., 2008; Van Klink et al., 2014; Zijlmans et al., 2012) than ripples. The application of the automatic algorithm to databases with higher frequency rates would allow the comparison between ripples and fast ripples in terms of density or spatial location.
- Although the results show a significant improvement of the localization of IEDs and HFOs with noninvasive techniques, additional validation taking into account the spatial localization of the epileptic focus provided by ictal intracranial recordings would be helpful. However, this information was not available for the recordings used for this thesis. Also, an interesting study combining multimodal analysis techniques such as EEG or fMRI would provide more information about the localization of the cerebral sources.
- Using the developed algorithms, the spatial comparison of the brain areas generating

IEDs and HFOs could be objectively performed. This will allow to identify differences between the IEDs originating in the same areas than HFOs, and those generating in widespread areas. Understanding the differences between IEDs and its relationship with HFOs would help to interpret the processes of epileptogenesis and to determine whether there are different types of IEDs, some that might act to suppress seizures, while others could promote them (Staba and Bragin, 2011).

- Finally, to faster and increase the use of the methods developed in this thesis, the algorithms could be published, along with other developed by the BIOART group, in an open and freely-available toolbox. This will facilitate the use of these techniques by other research groups or even by clinicians.

# Bibliography

- American Electroencephalographic Society guidelines for standard electrode position nomenclature. *Journal of clinical neurophysiology : official publication of the American Electroencephalographic Society*, 8(2):200–2, 4 1991.
- Airaksinen, K., Mäkelä, J. P., Taulu, S., Ahonen, A., Nurminen, J., Schnitzler, A., and Pekkonen, E. Effects of DBS on auditory and somatosensory processing in Parkinson’s disease. *Human Brain Mapping*, 32(7):1091–1099, 7 2011.
- Alexopoulos, A. V. Pharmacoresistant epilepsy: Definition and explanation. *Epileptology*, 1(1):38–42, 2013.
- Amo, C., Saldaña, C., Hidalgo, M. G., Maestú, F., Fernández, A., Arrazola, J., and Ortiz, T. Magnetoencephalographic localization of peritumoral temporal epileptic focus previous surgical resection. *Seizure*, 12(1):19–22, 1 2003.
- Anderson, C. T., Carlson, C. E., Li, Z., and Raghavan, M. Magnetoencephalography in the Preoperative Evaluation for Epilepsy Surgery. *Current Neurology and Neuroscience Reports*, 14(5):446, 5 2014.
- Andrade-Valenca, L. P., Dubeau, F., Mari, F., Zelmann, R., and Gotman, J. Interictal scalp fast oscillations as a marker of the seizure onset zone. *Neurology*, 77(6):524–31, 8 2011.
- Andreassi, J. L. *Psychophysiology : human behavior and physiological response*. Lawrence Erlbaum, 2007.
- Andrzejak, R. G., Chicharro, D., Elger, C. E., and Mormann, F. Seizure prediction: any better than chance? *Clinical neurophysiology : official journal of the International Federation of Clinical Neurophysiology*, 120(8):1465–78, 8 2009.
- Asaad, W. and Cosgrove, G. R. Chapter 11 – Imaging and Epilepsy: The Key to Surgical Success. In *Image-Guided Neurosurgery*, pages 263–276. 2015.
- Attal, Y., Bhattacharjee, M., Yelnik, J., Cottureau, B., Lefèvre, J., Okada, Y., Bardinet, E., Chupin, M., and Baillet, S. Modeling and detecting deep brain activity with MEG & EEG. In *Annual International Conference of the IEEE Engineering in Medicine and Biology - Proceedings*, 2007.
- Aydin, U., Vorwerk, J., Dümpelmann, M., Küpper, P., Kugel, H., Heers, M., Wellmer, J., Kellinghaus, C., Haueisen, J., Rampp, S., Stefan, H., and Wolters, C. H. Combined EEG/MEG Can Outperform Single Modality EEG or MEG Source Reconstruction in Presurgical Epilepsy Diagnosis. *PLOS ONE*, 10(3):e0118753, 3 2015.

- Bagić, A. I., Knowlton, R. C., Rose, D. F., Ebersole, J. S., and ACMEGS Clinical Practice Guideline (CPG) Committee. American Clinical Magnetoencephalography Society Clinical Practice Guideline 1. *Journal of Clinical Neurophysiology*, 28(4):1, 8 2011.
- Baillet, S., Mosher, J., and Leahy, R. Electromagnetic brain mapping. *IEEE Signal Processing Magazine*, 18(6):14–30, 2001.
- Barkley, G. L. Controversies in neurophysiology. MEG is superior to EEG in localization of interictal epileptiform activity: Pro. *Clinical Neurophysiology*, 115(5):1001–1009, 5 2004.
- Barnard, A. C., Duck, I. M., Lynn, M. S., and Timlake, W. P. The application of electromagnetic theory to electrocardiology. II. Numerical solution of the integral equations. *Biophysical journal*, 7(5):463–91, 9 1967.
- Bartolomei, F., Trébuchon, A., Bonini, F., Lambert, I., Gavaret, M., Woodman, M., Giusiano, B., Wendling, F., and Bénar, C. What is the concordance between the seizure onset zone and the irritative zone? A SEEG quantified study. *Clinical Neurophysiology*, 127(2):1157–1162, 2 2016.
- Baumgartner, C. Controversies in clinical neurophysiology. MEG is superior to EEG in the localization of interictal epileptiform activity: Con. *Clinical Neurophysiology*, 115(5):1010–1020, 5 2004.
- Bear, M., Connors, B., and Paradiso, M. *Neuroscience: Exploring the Brain*. Wolters Kluwer, Philadelphia, 4th edition, 2016.
- Bell, A. J. and Sejnowski, T. J. An information-maximization approach to blind separation and blind deconvolution. *Neural Computation*, 7(6):1129–1159, 1995.
- Belliveau, J. W., Kennedy, D. N., McKinstry, R. C., Buchbinder, B. R., Weisskoff, R. M., Cohen, M. S., Vevea, J. M., Brady, T. J., and Rosen, B. R. Functional mapping of the human visual cortex by magnetic resonance imaging. *Science (New York, N.Y.)*, 254(5032):716–9, 11 1991.
- Berg, A. T., Vickrey, B. G., Langfitt, J. T., Sperling, M. R., Walczak, T. S., Shinnar, S., Bazil, C. W., Pacia, S. V., Spencer, S. S., and Multicenter Study of Epilepsy Surgery. The multicenter study of epilepsy surgery: recruitment and selection for surgery. *Epilepsia*, 44(11):1425–33, 11 2003.
- Boto, E., Meyer, S., Shah, V., Alem, O., Knappe, S., Kruger, P., Fromhold, M., Lim, M., Morris, P. G., Bowtell, R., Barnes, G. R., and Brookes, M. J. A New Generation of Magnetoencephalography: Room Temperature Measurements using Optically-Pumped Magnetometers. *NeuroImage*, 1:404–414, 4 2016.
- Bouet, R., Jung, J., Delpuech, C., Ryvlin, P., Isnard, J., Guenot, M., Bertrand, O., and Mauguière, F. Towards source volume estimation of interictal spikes in focal epilepsy using magnetoencephalography. *NeuroImage*, 59(4):3955–3966, 2012.
- Bragin, A., Mody, I., Wilson, C. L., and Engel, J. Local Generation of Fast Ripples in Epileptic Brain. *Journal of Neuroscience*, 22(5), 2002.
- Breuer, L., Dammers, J., Roberts, T. P. L., and Shah, N. J. A Constrained ICA Approach for Real-Time Cardiac Artifact Rejection in Magnetoencephalography. *IEEE Transactions on Biomedical Engineering*, 61(2):405–414, 2 2014.

- Burnos, S., Hilfiker, P., Sürücü, O., Scholkmann, F., Krayenbühl, N., Grunwald, T., and Sarnthein, J. Human Intracranial High Frequency Oscillations (HFOs) Detected by Automatic Time-Frequency Analysis. *PLoS ONE*, 9(4):e94381, 4 2014.
- Buzsáki, G., Horvath, Z., Urioste, R., Hetke, J., and Wise, K. High-frequency network oscillation in the hippocampus. *Science*, 256(5059), 1992.
- Buzsáki, G., Anastassiou, C. A., and Koch, C. The origin of extracellular fields and currents — EEG, ECoG, LFP and spikes. *Nature Reviews Neuroscience*, 13(6):407–420, 5 2012.
- Carpenter, R. H. S. R. H. S. and Reddi, B. *Neurophysiology : a conceptual approach*. Hodder Arnold, an Hachette UK Company, 2012.
- Cetin, M. S., Houck, J. M., Rashid, B., Agacoglu, O., Stephen, J. M., Sui, J., Canive, J., Mayer, A., Aine, C., Bustillo, J. R., and Calhoun, V. D. Multimodal Classification of Schizophrenia Patients with MEG and fMRI Data Using Static and Dynamic Connectivity Measures. *Frontiers in Neuroscience*, 10:466, 10 2016.
- Cheyne, D., Bostan, A. C., Gaetz, W., and Pang, E. W. Event-related beamforming: a robust method for presurgical functional mapping using MEG. *Clinical neurophysiology : official journal of the International Federation of Clinical Neurophysiology*, 118(8):1691–704, 8 2007.
- Cho, J. R., Joo, E. Y., Koo, D. L., Hong, S. C., and Hong, S. B. Clinical utility of interictal high-frequency oscillations recorded with subdural macroelectrodes in partial epilepsy. *Journal of clinical neurology (Seoul, Korea)*, 8(1):22–34, 3 2012.
- Chrobak, J. J. and Buzsáki, G. High-Frequency Oscillations in the Output Networks of the Hippocampal–Entorhinal Axis of the Freely Behaving Rat. *Journal of Neuroscience*, 16(9), 1996.
- Cichocki, A. and Amari, S.-i. *Adaptive Blind Signal and Image Processing: Learning Algorithms and Applications*. 2003.
- Cichocki, A., Shishkin, S. L., Musha, T., Leonowicz, Z., Asada, T., and Kurachi, T. EEG filtering based on blind source separation (BSS) for early detection of Alzheimer’s disease. *Clinical Neurophysiology*, 116(3):729–737, 2005.
- Claus, S., Velis, D., Lopes da Silva, F. H., Viergever, M. A., and Kalitzin, S. High frequency spectral components after Secobarbital: The contribution of muscular origin—A study with MEG/EEG. *Epilepsy Research*, 100(1):132–141, 2012.
- Cohen, D. Magnetoencephalography: Evidence of Magnetic Fields Produced by Alpha-Rhythm Currents. *Science*, 161(3843):784–786, 8 1968.
- Coles, M. G. H. and Rugg, M. D. Event-related brain potentials: an introduction. In *Electrophysiology of Mind*, chapter Introducti, pages 1–26. Oxford University Press, 9 1996.
- Crepon, B., Navarro, V., Hasboun, D., Clemenceau, S., Martinerie, J., Baulac, M., Adam, C., and Le Van Quyen, M. Mapping interictal oscillations greater than 200 Hz recorded with intracranial macroelectrodes in human epilepsy. *Brain*, 133(1):33–45, 1 2010.
- Criswell, E. and Cram, J. R. *Cram’s introduction to surface electromyography*. Jones and Bartlett, 2011.

- Croft, R. and Barry, R. Removal of ocular artifact from the EEG: a review. *Neurophysiologie Clinique/Clinical Neurophysiology*, 30(1):5–19, 2 2000.
- Cuffin, B. N. and Cohen, D. Magnetic Fields of a Dipole in Special Volume Conductor Shapes. *IEEE Transactions on Biomedical Engineering*, BME-24(4):372–381, 7 1977.
- Cuffin, B. N. and Cohen, D. Comparison of the magnetoencephalogram and electroencephalogram. *Electroencephalography and clinical neurophysiology*, 47(2):132–46, 8 1979.
- de Curtis, M., Jefferys, J. G. R., and Avoli, M. *Interictal Epileptiform Discharges in Partial Epilepsy: Complex Neurobiological Mechanisms Based on Experimental and Clinical Evidence*. National Center for Biotechnology Information (US), 2012.
- Delorme, A. and Makeig, S. EEGLAB: an open source toolbox for analysis of single-trial EEG dynamics including independent component analysis. *Journal of Neuroscience Methods*, 134(1):9–21, 2004.
- Ebersole, J. S. Presurgical Assessment of the Epilepsies with Clinical Neurophysiology and Functional Imaging. In *Handbook of Clinical Neurophysiology*, volume 3 of *Handbook of Clinical Neurophysiology*, pages 471–490. Elsevier, 2003.
- Ebrahim, Z. Y., DeBoer, G. E., Luders, H., Hahn, J. F., and Lesser, R. P. Effect of etomidate on the electroencephalogram of patients with epilepsy. *Anesthesia and analgesia*, 65(10):1004–6, 10 1986.
- Enatsu, R., Mikuni, N., Usui, K., Matsubayashi, J., Taki, J., Begum, T., Matsumoto, R., Ikeda, A., Nagamine, T., Fukuyama, H., and Hashimoto, N. Usefulness of MEG magnetometer for spike detection in patients with mesial temporal epileptic focus. *NeuroImage*, 41(4):1206–1219, 2008.
- Engel Jr, J., Bragin, A., Staba, R., and Mody, I. High-frequency oscillations: What is normal and what is not? *Epilepsia*, 50(4):598–604, 4 2009.
- Englot, D. J., Nagarajan, S. S., Imber, B. S., Raygor, K. P., Honma, S. M., Mizuiri, D., Mantle, M., Knowlton, R. C., Kirsch, H. E., and Chang, E. F. Epileptogenic zone localization using magnetoencephalography predicts seizure freedom in epilepsy surgery. *Epilepsia*, 56(6):949–958, 6 2015.
- Ermer, J. J., Mosher, J. C., Baillet, S., and Leah, R. M. Rapidly recomputable EEG forward models for realistic head shapes. *Physics in medicine and biology*, 46(4):1265–81, 4 2001.
- Escudero, J., Hornero, R., Abasolo, D., Fernandez, A., and Lopez-Coronado, M. Artifact Removal in Magnetoencephalogram Background Activity With Independent Component Analysis. *IEEE Transactions on Biomedical Engineering*, 54(11):1965–1973, 11 2007.
- Escudero, J., Hornero, R., Abásolo, D., Cichocki, A., and Takeda, T. Consistency of the blind source separation computed with five common algorithms for magnetoencephalogram background activity. *Medical engineering & physics*, 32(10):1137–44, 12 2010.
- Escudero, J., Hornero, R., Abásolo, D., and Fernández, A. Quantitative Evaluation of Artifact Removal in Real Magnetoencephalogram Signals with Blind Source Separation. *Annals of Biomedical Engineering*, 39(8):2274–2286, 8 2011.
- Fahoum, F., Melani, F., Andrade-Valença, L., Dubeau, F., and Gotman, J. Epileptic scalp ripples are associated with corticothalamic BOLD changes. *Epilepsia*, 55(10):1611–9, 10 2014.

- Falco-Walter, J., Owen, C., Sharma, M., Reggi, C., Yu, M., Stoub, T. R., and Stein, M. A. Magnetoencephalography and New Imaging Modalities in Epilepsy. *Neurotherapeutics*, 14(1): 4–10, 1 2017.
- Fatima, Z., Quraan, M. A., Kovacevic, N., and McIntosh, A. R. ICA-based artifact correction improves spatial localization of adaptive spatial filters in MEG. *NeuroImage*, 78:284–294, 9 2013.
- Fedele, T., Scheer, H. J., Burghoff, M., Curio, G., and Körber, R. Ultra-low-noise EEG/MEG systems enable bimodal non-invasive detection of spike-like human somatosensory evoked responses at 1 kHz. *Physiological Measurement*, 36(2):357–368, 2 2015.
- Fischer, M. J. M., Scheler, G., and Stefan, H. Utilization of magnetoencephalography results to obtain favourable outcomes in epilepsy surgery. *Brain : a journal of neurology*, 128(Pt 1): 153–7, 1 2005.
- Fisher, R. S., Webber, W. R., Lesser, R. P., Arroyo, S., and Uematsu, S. High-frequency EEG activity at the start of seizures. *Journal of clinical neurophysiology : official publication of the American Electroencephalographic Society*, 9(3):441–8, 7 1992.
- Fisher, R. S., Boas, W. v. E., Blume, W., Elger, C., Genton, P., Lee, P., and Engel, J. Epileptic Seizures and Epilepsy: Definitions Proposed by the International League Against Epilepsy (ILAE) and the International Bureau for Epilepsy (IBE). *Epilepsia*, 46(4):470–472, 4 2005.
- Franco, V., Canevini, M. P., Capovilla, G., De Sarro, G., Galimberti, C. A., Gatti, G., Guerrini, R., La Neve, A., Rosati, E., Specchio, L. M., Striano, S., Tinuper, P., and Perucca, E. Off-Label Prescribing of Antiepileptic Drugs in Pharmacoresistant Epilepsy: A Cross-Sectional Drug Utilization Study of Tertiary Care Centers in Italy. *CNS Drugs*, 28(10):939–949, 10 2014.
- Fröhlich, F. and Fröhlich, F. Chapter 24 – Epilepsy. In *Network Neuroscience*, pages 297–308. 2016.
- Fujiwara, H., Greiner, H. M., Lee, K. H., Holland-Bouley, K. D., Seo, J. H., Arthur, T., Mangano, F. T., Leach, J. L., and Rose, D. F. Resection of ictal high-frequency oscillations leads to favorable surgical outcome in pediatric epilepsy. *Epilepsia*, 53(9):1607–17, 9 2012.
- Garcés, P., Pereda, E., Hernández-Tamames, J. A., Del-Pozo, F., Maestú, F., and Ángel Pineda-Pardo, J. Multimodal description of whole brain connectivity: A comparison of resting state MEG, fMRI, and DWI. *Human Brain Mapping*, 37(1):20–34, 1 2016.
- Gloor, P. Neuronal generators and the problem of localization in electroencephalography: application of volume conductor theory to electroencephalography. *Journal of clinical neurophysiology : official publication of the American Electroencephalographic Society*, 2(4):327–54, 10 1985.
- Gonzalez-Moreno, A., Aurtenetxe, S., Lopez-Garcia, M.-E., del Pozo, F., Maestu, F., and Nevado, A. Signal-to-noise ratio of the MEG signal after preprocessing. *Journal of neuroscience methods*, 222:56–61, 1 2014.
- Gotman, J. Automatic recognition of epileptic seizures in the EEG. *Electroencephalography and Clinical Neurophysiology*, 54(5):530–540, 1982.
- Gotman, J. High frequency oscillations: The new EEG frontier? *Epilepsia*, 51(s1):63–65, 2 2010.



- Gross, J., Baillet, S., Barnes, G. R., Henson, R. N., Hillebrand, A., Jensen, O., Jerbi, K., Litvak, V., Maess, B., Oostenveld, R., Parkkonen, L., Taylor, J. R., van Wassenhove, V., Wibral, M., and Schoffelen, J.-M. Good practice for conducting and reporting MEG research. *NeuroImage*, 65:349–363, 1 2013.
- Grova, C., Aiguabella, M., Zelmann, R., Lina, J. M., Hall, J. A., and Kobayashi, E. Intracranial EEG potentials estimated from MEG sources: A new approach to correlate MEG and iEEG data in epilepsy. *Human Brain Mapping*, 2016.
- Haegelen, C., Perucca, P., Châtillon, C.-E., Andrade-Valença, L., Zelmann, R., Jacobs, J., Collins, D. L., Dubeau, F., Olivier, A., and Gotman, J. High-frequency oscillations, extent of surgical resection, and surgical outcome in drug-resistant focal epilepsy. *Epilepsia*, 54(5): 848–857, 5 2013.
- Hall, E. L., Robson, S. E., Morris, P. G., and Brookes, M. J. The relationship between MEG and fMRI. *NeuroImage*, 102:80–91, 11 2014.
- Hämäläinen, M. and Hari, R. Basic Principles and Methods of Data Collection and Source Analysis. In Toga, A. and Mazziotta, J., editors, *Brain mapping: The methods*, chapter 10. 2nd edition, 2004.
- Hämäläinen, M., Hari, R., Ilmoniemi, R. J., Knuutila, J., and Lounasmaa, O. V. Magnetoencephalography—theory, instrumentation, and applications to noninvasive studies of the working human brain. *Reviews of Modern Physics*, 65(2):413–497, 4 1993.
- Hari. Magnetoencephalography in Clinical Neurophysiological Assessment of Human Cortical Functions. 2004.
- Hari, R. and Salmelin, R. Magnetoencephalography: From SQUIDS to neuroscience. *Neuroimage* 20th anniversary special edition. *NeuroImage*, 61(2):386–96, 6 2012.
- Hari, R., Joutsiniemi, S.-L., and Sarvas, J. Spatial resolution of neuromagnetic records: theoretical calculations in a spherical model. *Electroencephalography and Clinical Neurophysiology/Evoked Potentials Section*, 71(1):64–72, 1988.
- Haumann, N. T., Parkkonen, L., Kliuchko, M., Vuust, P., and Brattico, E. Comparing the Performance of Popular MEG/EEG Artifact Correction Methods in an Evoked-Response Study. *Computational intelligence and neuroscience*, 2016:7489108, 2016.
- Heller, L. and Volegov, P. Electric and Magnetic Fields of the Brain. In *Magnetoencephalography*, pages 73–105. Springer Berlin Heidelberg, Berlin, Heidelberg, 2014.
- Hillebrand, A. and Barnes, G. R. Beamformer Analysis of MEG Data, 2005.
- Hillebrand, A., Fazio, P., de Munck, J., and van Dijk, B. Feasibility of clinical Magnetoencephalography (MEG) functional mapping in the presence of dental artefacts. *Clinical Neurophysiology*, 124(1):107–113, 1 2013.
- Hillebrand A, B. G. A quantitative assessment of the sensitivity of whole-head MEG to activity in the adult human cortex. *Neuroimage*, 16:638–50, 2002.
- Huang, M. X., Mosher, J. C., and Leahy, R. M. A sensor-weighted overlapping-sphere head model and exhaustive head model comparison for MEG. *Physics in medicine and biology*, 44 (2):423–40, 2 1999.

- Huang, Z. Brief History and Development of Electrophysiological Recording Techniques in Neuroscience. In *Signal Processing in Neuroscience*, pages 1–10. Springer Singapore, Singapore, 2016.
- Huiskamp, G., Agirre-Arrizubieta, Z., and Leijten, F. Regional differences in the sensitivity of MEG for interictal spikes in epilepsy. *Brain topography*, 23(2):159–64, 6 2010.
- Hyvärinen, A. Fast and robust fixed-point algorithms for independent component analysis. *IEEE transactions on neural networks / a publication of the IEEE Neural Networks Council*, 10(3):626–34, 1 1999.
- Hyvärinen, A. and Oja, E. Independent component analysis: algorithms and applications. *Neural networks : the official journal of the International Neural Network Society*, 13(4-5): 411–30, 2000.
- Hyvärinen, A., Karhunen, J., and Oja, E. Independent Component Analysis. *Independent Component Analysis*, pages 1–8, 2001.
- Iwasaki, M., Nakasato, N., Shamoto, H., and Yoshimoto, T. Focal magnetoencephalographic spikes in the superior temporal plane undetected by scalp EEG. *Journal of clinical neuroscience : official journal of the Neurosurgical Society of Australasia*, 10(2):236–8, 3 2003.
- Jackson, A. F. and Bolger, D. J. The neurophysiological bases of EEG and EEG measurement: A review for the rest of us. *Psychophysiology*, 51(11):1061–1071, 11 2014.
- Jacobs, J., LeVan, P., Chander, R., Hall, J., Dubeau, F., and Gotman, J. Interictal high-frequency oscillations (80-500 Hz) are an indicator of seizure onset areas independent of spikes in the human epileptic brain. *Epilepsia*, 49(11):1893–1907, 11 2008.
- Jacobs, J., Zijlmans, M., Zelmann, R., Chatillon, C.-E., Hall, J., Olivier, A., Dubeau, F., and Gotman, J. High-frequency electroencephalographic oscillations correlate with outcome of epilepsy surgery. *Annals of neurology*, 67(2):209–20, 2 2010.
- Jacobs, J., Staba, R., Asano, E., Otsubo, H., Wu, J. Y., Zijlmans, M., Mohamed, I., Kahane, P., Dubeau, F., Navarro, V., and Gotman, J. High-frequency oscillations (HFOs) in clinical epilepsy. *Progress in neurobiology*, 98(3):302–15, 9 2012.
- James, C. J. and Hesse, C. W. Independent component analysis for biomedical signals. *Physiological Measurement*, 26(1):15–39, 2005.
- Jaseja, H. and Jaseja, B. EEG spike versus EEG sharp wave: differential clinical significance in epilepsy. *Epilepsy & behavior : E&B*, 25(1):137, 9 2012.
- Jefferys, J. G. Nonsynaptic modulation of neuronal activity in the brain: electric currents and extracellular ions. *Physiological reviews*, 75(4):689–723, 10 1995.
- Jefferys, J. G. R., Menendez de la Prida, L., Wendling, F., Bragin, A., Avoli, M., Timofeev, I., and Lopes da Silva, F. H. Mechanisms of physiological and epileptic HFO generation. *Progress in neurobiology*, 98(3):250–64, 9 2012.
- Jin, K., Alexopoulos, A. V., Mosher, J. C., and Burgess, R. C. Implanted medical devices or other strong sources of interference are not barriers to magnetoencephalographic recordings in epilepsy patients. *Clinical neurophysiology : official journal of the International Federation of Clinical Neurophysiology*, 124(7):1283–9, 7 2013.

- Jiruska, P., Csicsvari, J., Powell, A. D., Fox, J. E., Chang, W. C., Vreugdenhil, M., Li, X., Palus, M., Bujan, A. F., Dearden, R. W., and Jefferys, J. G. R. High-Frequency Network Activity, Global Increase in Neuronal Activity, and Synchrony Expansion Precede Epileptic Seizures In Vitro. *Journal of Neuroscience*, 30(16):5690–5701, 4 2010.
- Kakisaka, Y., Kubota, Y., Wang, Z. I., Piao, Z., Mosher, J. C., Gonzalez-Martinez, J., Jin, K., Alexopoulos, A. V., and Burgess, R. C. Use of simultaneous depth and MEG recording may provide complementary information regarding the epileptogenic region. *doi.org*, 14(3): 298–303, 2012.
- Kass, J. S., Mizrahi, E. M., Maheshwari, A., and Haneef, Z. Chapter 22 – Seizures and Epilepsy. In *Neurology Secrets*, chapter 22, pages 301–323. 2017.
- Keller, C. J., Truccolo, W., Gale, J. T., Eskandar, E., Thesen, T., Carlson, C., Devinsky, O., Kuzniecky, R., Doyle, W. K., Madsen, J. R., Schomer, D. L., Mehta, A. D., Brown, E. N., Hochberg, L. R., Ulbert, I., Halgren, E., and Cash, S. S. Heterogeneous neuronal firing patterns during interictal epileptiform discharges in the human cortex. *Brain*, 133(6): 1668–1681, 6 2010.
- Klamer, S., Elshahabi, A., Lerche, H., Braun, C., Erb, M., Scheffler, K., and Focke, N. K. Differences Between MEG and High-Density EEG Source Localizations Using a Distributed Source Model in Comparison to fMRI. *Brain Topography*, 28(1):87–94, 1 2015.
- Klem, G. H., Lüders, H. O., Jasper, H. H., and Elger, C. The ten-twenty electrode system of the International Federation. The International Federation of Clinical Neurophysiology. *Electroencephalography and clinical neurophysiology. Supplement*, 52:3–6, 1999.
- Knake, S., Halgren, E., Shiraishi, H., Hara, K., Hamer, H. M., Grant, P. E., Carr, V. A., Foxe, D., Camposano, S., Busa, E., Witzel, T., Hämäläinen, M. S., Ahlfors, S. P., Bromfield, E. B., Black, P. M., Bourgeois, B. F., Cole, A. J., Cosgrove, G. R., Dworetzky, B. A., Madsen, J. R., Larsson, P. G., Schomer, D. L., Thiele, E. A., Dale, A. M., Rosen, B. R., and Stufflebeam, S. M. The value of multichannel MEG and EEG in the presurgical evaluation of 70 epilepsy patients. *Epilepsy research*, 69(1):80–6, 4 2006.
- Kobayashi, K., Watanabe, Y., Inoue, T., Oka, M., Yoshinaga, H., and Ohtsuka, Y. Scalp-recorded high-frequency oscillations in childhood sleep-induced electrical status epilepticus. *Epilepsia*, 51(10):2190–2194, 10 2010.
- Lee, T. W., Girolami, M., and Sejnowski, T. J. Independent component analysis using an extended infomax algorithm for mixed subgaussian and supergaussian sources. *Neural computation*, 11:417–441, 1999.
- Lee, Y.-H. and Kim, K. Instrumentation for Measuring MEG Signals. In *Magnetoencephalography*, pages 3–33. Springer Berlin Heidelberg, Berlin, Heidelberg, 2014.
- Li, Y.-O., Adah, T., and Calhoun, V. D. Estimating the number of independent components for functional magnetic resonance imaging data. *Human Brain Mapping*, 28(11):1251–1266, 11 2007.
- Lin, Y., Shih, Y., Hsieh, J., Yu, H., Yiu, C., Wong, T., Yeh, T., Kwan, S., Ho, L., Yen, D., Wu, Z., and Chang, M. Magnetoencephalographic yield of interictal spikes in temporal lobe epilepsy: Comparison with scalp EEG recordings. *NeuroImage*, 19(3):1115–1126, 2003.

- Liu, S., Cai, W., Liu, S., Zhang, F., Fulham, M., Feng, D., Pujol, S., and Kikinis, R. Multimodal neuroimaging computing: a review of the applications in neuropsychiatric disorders. *Brain Informatics*, 2(3):167, 2015a.
- Liu, S., Sha, Z., Sencer, A., Aydoseli, A., Bebek, N., Abosch, A., Henry, T., Gurses, C., and Ince, N. F. Exploring the time-frequency content of high frequency oscillations for automated identification of seizure onset zone in epilepsy. *Journal of neural engineering*, 13(2):026026, 4 2016.
- Liu, S.-Y., Yang, X.-L., Chen, B., Hou, Z., An, N., Yang, M.-H., and Yang, H. Clinical outcomes and quality of life following surgical treatment for refractory epilepsy: a systematic review and meta-analysis. *Medicine*, 94(6):e500, 2 2015b.
- Liu, Z., Ding, L., and He, B. Integration of EEG/MEG with MRI and fMRI. *IEEE engineering in medicine and biology magazine : the quarterly magazine of the Engineering in Medicine & Biology Society*, 25(4):46–53, 2006.
- Lodish, H., Berk, A., Zipursky, S. L., Matsudaira, P., Baltimore, D., and Darnell, J. Overview of Neuron Structure and Function. 2000.
- Lüders, H. O., Najm, I., Nair, D., Widdess-Walsh, P., and Bingman, W. The epileptogenic zone: general principles. *Epileptic disorders : international epilepsy journal with videotape*, 8 Suppl 2:1–9, 8 2006.
- Lütkenhöner, B. Dipole source localization by means of maximum likelihood estimation I. Theory and simulations. *Electroencephalography and clinical neurophysiology*, 106(4):314–21, 4 1998.
- Mantini, D., Franciotti, R., Romani, G., and Pizzella, V. Improving MEG source localizations: An automated method for complete artifact removal based on independent component analysis. *NeuroImage*, 40(1):160–173, 3 2008.
- Matsumoto, A., Brinkmann, B. H., Matthew Stead, S., Matsumoto, J., Kucewicz, M. T., Marsh, W. R., Meyer, F., and Worrell, G. Pathological and physiological high-frequency oscillations in focal human epilepsy. *Journal of neurophysiology*, 110(8):1958–64, 10 2013.
- McWhinney, S. R., Bardouille, T., D’Arcy, R. C. N., and Newman, A. J. Asymmetric Weighting to Optimize Regional Sensitivity in Combined fMRI-MEG Maps. *Brain Topography*, 29(1): 1–12, 1 2016.
- Medvedovsky, M., Taulu, S., Bickmullina, R., Ahonen, A., and Paetau, R. Fine tuning the correlation limit of spatio-temporal signal space separation for magnetoencephalography. *Journal of Neuroscience Methods*, 177(1):203–211, 2009.
- Melani, F., Zermann, R., Dubeau, F., and Gotman, J. Occurrence of scalp-fast oscillations among patients with different spiking rate and their role as epileptogenicity marker. *Epilepsy Research*, 106(3):345–356, 2013.
- Miao, A., Xiang, J., Tang, L., Ge, H., Liu, H., Wu, T., Chen, Q., Hu, Z., Lu, X., and Wang, X. Using ictal high-frequency oscillations (80-500Hz) to localize seizure onset zones in childhood absence epilepsy: a MEG study. *Neuroscience letters*, 566:21–6, 4 2014.
- Migliorelli, C., Romero, S., Alonso, J., Nowak, R., Russi, A., and Mananas, M. Reduction of metallic interference in MEG signals using AMUSE. In *Proceedings of the Annual International Conference of the IEEE Engineering in Medicine and Biology Society, EMBS*, 2013.

- Migliorelli, C., Alonso, J. F., Romero, S., Mañanas, M. A., Nowak, R., and Russi, A. Automatic BSS-based filtering of metallic interference in MEG recordings: definition and validation using simulated signals. *Journal of neural engineering*, 12(4):046001, 5 2015.
- Migliorelli, C., Alonso, J. F., Romero, S., Mañanas, M. A., Nowak, R., and Russi, A. Influence of metallic artifact filtering on MEG signals for source localization during interictal epileptiform activity. *Journal of Neural Engineering*, 13(2):026029, 2016.
- Migliorelli, C., Alonso, J. F., Romero, S., Mañanas, M. A., Nowak, R., and Russi, A. Visual Detection of High Frequency Oscillations in MEG. pages 769–773. Springer, Cham, 2017a.
- Migliorelli, C., Alonso, J. F., Romero, S., Nowak, R., Russi, A., and Mananas, M. Automated detection of epileptic ripples in MEG using beamformer-based virtual sensors. *Journal of Neural Engineering*, 3 2017b.
- Modur, P. and Miocinovic, S. Interictal high-frequency oscillations (HFOs) as predictors of high frequency and conventional seizure onset zones. *Epileptic Disorders*, 17(4):413–424, 2015.
- Mosher, J. C., Leahy, R. M., and Lewis, P. S. EEG and MEG: forward solutions for inverse methods. *IEEE transactions on bio-medical engineering*, 46(3):245–59, 3 1999.
- Mosher, J. C., Baillet, S., and Leahy, R. M. Equivalence of linear approaches in bioelectromagnetic inverse solutions. In *IEEE Workshop on Statistical Signal Processing Proceedings*, volume 2003-Janua, pages 294–297. IEEE, 2003.
- Muthukumaraswamy, S. D. High-frequency brain activity and muscle artifacts in MEG/EEG: a review and recommendations. *Frontiers in human neuroscience*, 7:138, 1 2013.
- Nenonen, J., Nurminen, J., Kičić, D., Bickmullina, R., Lioumis, P., Jousmäki, V., Taulu, S., Parkkonen, L., Putaala, M., and Kähkönen, S. Validation of head movement correction and spatiotemporal signal space separation in magnetoencephalography. *Clinical neurophysiology : official journal of the International Federation of Clinical Neurophysiology*, 123(11):2180–91, 11 2012.
- Niedermeyer, E., Schomer, D. L., and Lopes da Silva, F. H. *Niedermeyer’s electroencephalography : basic principles, clinical applications, and related fields*. Wolters Kluwer Health, 2010.
- Nissen, I. A., Stam, C. J., Citroen, J., Reijneveld, J. C., and Hillebrand, A. Preoperative evaluation using magnetoencephalography: Experience in 382 epilepsy patients. *Epilepsy Research*, 124, 2016a.
- Nissen, I. A., van Klink, N. E., Zijlmans, M., Stam, C. J., and Hillebrand, A. Brain areas with epileptic high frequency oscillations are functionally isolated in MEG virtual electrode networks. *Clinical Neurophysiology*, 127(7):2581–2591, 7 2016b.
- Nolte, G. The magnetic lead field theorem in the quasi-static approximation and its use for magnetoencephalography forward calculation in realistic volume conductors. *Physics in medicine and biology*, 48(22):3637–52, 11 2003.
- Nowak, R., Santiuste, M., and Russi, A. Toward a definition of MEG spike: parametric description of spikes recorded simultaneously by MEG and depth electrodes. *Seizure : the journal of the British Epilepsy Association*, 18(9):652–5, 11 2009.

- Oishi, M., Kameyama, S., Masuda, H., Tohyama, J., Kanazawa, O., Sasagawa, M., and Otsubo, H. Single and multiple clusters of magnetoencephalographic dipoles in neocortical epilepsy: significance in characterizing the epileptogenic zone. *Epilepsia*, 47(2):355–64, 2 2006.
- Oostenveld, R., Fries, P., Maris, E., and Schoffelen, J.-M. FieldTrip: Open source software for advanced analysis of MEG, EEG, and invasive electrophysiological data. *Computational intelligence and neuroscience*, 2011:156869, 1 2011.
- Oswal, A., Jha, A., Neal, S., Reid, A., Bradbury, D., Aston, P., Limousin, P., Foltynie, T., Zrinzo, L., Brown, P., and Litvak, V. Analysis of simultaneous MEG and intracranial LFP recordings during Deep Brain Stimulation: a protocol and experimental validation. *Journal of neuroscience methods*, 261:29–46, 3 2016.
- Otsubo, H., Ochi, A., Imai, K., Akiyama, T., Fujimoto, A., Go, C., Dirks, P., and Donner, E. J. High-frequency oscillations of ictal muscle activity and epileptogenic discharges on intracranial EEG in a temporal lobe epilepsy patient. *Clinical Neurophysiology*, 119(4):862–868, 2008.
- Panzica, F., Varotto, G., Rotondi, F., Spreafico, R., and Franceschetti, S. Identification of the Epileptogenic Zone from Stereo-EEG Signals: A Connectivity-Graph Theory Approach. *Frontiers in Neurology*, 4:175, 1 2013.
- Papadelis, C., Tamilia, E., Stufflebeam, S., Grant, P. E., Madsen, J. R., Pearl, P. L., and Tanaka, N. Interictal High Frequency Oscillations Detected with Simultaneous Magnetoencephalography and Electroencephalography as Biomarker of Pediatric Epilepsy. *Journal of visualized experiments : JoVE*, (118), 12 2016.
- Patarraia, E., Lindinger, G., Deecke, L., Mayer, D., and Baumgartner, C. Combined MEG/EEG analysis of the interictal spike complex in mesial temporal lobe epilepsy. *NeuroImage*, 24(3): 607–614, 2005.
- Penfield, W. and Jasper, H. *Epilepsy and the functional anatomy of the human brain*, volume 6. Elsevier, London, 1 1954.
- Peterchev, A. V., Wagner, T. A., Miranda, P. C., Nitsche, M. A., Paulus, W., Lisanby, S. H., Pascual-Leone, A., and Bikson, M. Fundamentals of transcranial electric and magnetic stimulation dose: Definition, selection, and reporting practices. *Brain Stimulation*, 5(4):435–453, 10 2012.
- Pittau, F., Grouiller, F., Spinelli, L., Seeck, M., Michel, C. M., and Vulliemoz, S. The role of functional neuroimaging in pre-surgical epilepsy evaluation. *Frontiers in neurology*, 5:31, 2014.
- Pizzo, F., Ferrari-Marinho, T., Amiri, M., Frauscher, B., Dubeau, F., and Gotman, J. When spikes are symmetric, ripples are not: Bilateral spike and wave above 80Hz in focal and generalized epilepsy. *Clinical Neurophysiology*, 127(3):1794–1802, 2016.
- Purves, D. and Williams, S. M. S. M. *Neuroscience. 2nd edition*. Sinauer Associates, 2nd edition, 2001.
- Ramantani, G., Boor, R., Paetau, R., Ille, N., Feneberg, R., Rupp, A., Boppel, T., Scherg, M., Rating, D., and Bast, T. MEG Versus EEG: Influence of Background Activity on Interictal Spike Detection. *Journal of Clinical Neurophysiology*, 23(6):498–508, 12 2006.

- Ramey, W. L., Martirosyan, N. L., Lieu, C. M., Hasham, H. A., Lemole, G. M., and Weinand, M. E. Current management and surgical outcomes of medically intractable epilepsy. *Clinical neurology and neurosurgery*, 115(12):2411–8, 12 2013.
- Reece, J., Urry, L., Cain, M., Wasserman, S., Minorsky, P., and Jackson, R. *Campbell Biology*, volume 12. 9th edition, 2013.
- Richman, J. S. and Moorman, J. R. Physiological time-series analysis using approximate entropy and sample entropy. *American journal of physiology. Heart and circulatory physiology*, 278(6):2039–49, 6 2000.
- Rolls, E. T. Limbic systems for emotion and for memory, but no single limbic system. *Cortex*, 62:119–157, 2015.
- Romero, S., Mañanas, M. a., and Barbanoj, M. J. A comparative study of automatic techniques for ocular artifact reduction in spontaneous EEG signals based on clinical target variables: a simulation case. *Computers in biology and medicine*, 38(3):348–60, 3 2008.
- Romero, S., Mañanas, M. A., and Barbanoj, M. J. Ocular reduction in EEG signals based on adaptive filtering, regression and blind source separation. *Annals of Biomedical Engineering*, 37(1):176–191, 2009.
- Rosenow, F. and Lüders, H. Presurgical evaluation of epilepsy. *Brain : a journal of neurology*, 124(Pt 9):1683–700, 9 2001.
- Rummel, C., Abela, E., Andrzejak, R. G., Hauf, M., Pollo, C., Müller, M., Weisstanner, C., Wiest, R., and Schindler, K. Resected Brain Tissue, Seizure Onset Zone and Quantitative EEG Measures: Towards Prediction of Post-Surgical Seizure Control. *PloS one*, 10(10):e0141023, 2015.
- Sakkalis, V. Review of advanced techniques for the estimation of brain connectivity measured with EEG/MEG. *Computers in biology and medicine*, 41(12):1110–7, 12 2011.
- Santiuste, M., Nowak, R., Russi, A., Tarancon, T., Oliver, B., Ayats, E., Scheler, G., and Graetz, G. Simultaneous magnetoencephalography and intracranial EEG registration: technical and clinical aspects. *Journal of clinical neurophysiology : official publication of the American Electroencephalographic Society*, 25(6):331–9, 12 2008.
- Schomer, D. L. and Lopes da Silva, F. *Niedermeyer's Electroencephalography : Basic Principles, Clinical Applications, and Related Fields*. Wolters Kluwer Health, 2010.
- Schuele, S. U. and Lüders, H. O. Intractable epilepsy: management and therapeutic alternatives. *The Lancet. Neurology*, 7(6):514–24, 6 2008.
- Schulze-Bonhage, A. and Zentner, J. The preoperative evaluation and surgical treatment of epilepsy. *Deutsches Arzteblatt international*, 111(18):313–9, 5 2014.
- Sharon, D., Hämäläinen, M. S., Tootell, R. B. H., Halgren, E., and Belliveau, J. W. The advantage of combining MEG and EEG: comparison to fMRI in focally stimulated visual cortex. *NeuroImage*, 36(4):1225–1235, 2007.
- Shibasaki, H., Ikeda, A., Nagamine, T., Wennberg, R., Sharma, R., Otsubo, H., and Al., E. Use of magnetoencephalography in the presurgical evaluation of epilepsy patients. *Clinical neurophysiology : official journal of the International Federation of Clinical Neurophysiology*, 118(7):1438–48, 7 2007.

- Smith, S. J. M. EEG in neurological conditions other than epilepsy: when does it help, what does it add? *Journal of neurology, neurosurgery, and psychiatry*, 76 Suppl 2(suppl 2):8–12, 6 2005.
- Snyder, D. E., Echauz, J., Grimes, D. B., and Litt, B. The statistics of a practical seizure warning system. *Journal of neural engineering*, 5(4):392–401, 12 2008.
- Song, T., Cui, L., Gaa, K., Feffer, L., Taulu, S., Lee, R. R., and Huang, M. Signal Space Separation Algorithm and Its Application on Suppressing Artifacts Caused by Vagus Nerve Stimulation for Magnetoencephalography Recordings. *Journal of Clinical Neurophysiology*, 26(6):392–400, 12 2009.
- Song, Y., Sanganahalli, B. G., Hyder, F., Lin, W. C., and Riera, J. J. Distributions of irritative zones are related to individual alterations of resting-state networks in focal epilepsy. *PLoS ONE*, 10(7), 2015.
- Sörnmo, L., Laguna, P., Sörnmo, L., and Laguna, P. Chapter 1 – Introduction. In *Bioelectrical Signal Processing in Cardiac and Neurological Applications*, pages 1–24. 2005.
- Staba, R. J. and Bragin, A. High-frequency oscillations and other electrophysiological biomarkers of epilepsy: underlying mechanisms. *Biomarkers in Medicine*, 5(5):545–556, 10 2011.
- Staba, R. J., Stead, M., and Worrell, G. A. Electrophysiological biomarkers of epilepsy. *Neurotherapeutics : the journal of the American Society for Experimental NeuroTherapeutics*, 11(2):334–46, 4 2014.
- Stefan, H., Hummel, C., Scheler, G., Genow, A., Druschky, K., Tilz, C., Kaltenhäuser, M., Hopfengärtner, R., Buchfelder, M., and Romstöck, J. Magnetic brain source imaging of focal epileptic activity: a synopsis of 455 cases. *Brain : a journal of neurology*, 126(Pt 11):2396–405, 11 2003.
- Stefan, H., Scheler, G., Hummel, C., Walter, J., Romstöck, J., Buchfelder, M., and Blümcke, I. Magnetoencephalography (MEG) predicts focal epileptogenicity in cavernomas. *Journal of neurology, neurosurgery, and psychiatry*, 75(9):1309–13, 9 2004.
- Stefan, H., Rampp, S., Knowlton, R. C., Al., E., Binns, D., and Hicks, R. Magnetoencephalography adds to the surgical evaluation process. *Epilepsy & behavior : E&B*, 20(2):172–7, 2 2011.
- Sternickel, K. and Braginski, A. I. Biomagnetism using SQUIDS: status and perspectives. *Superconductor Science and Technology*, 19(3):S160–S171, 3 2006.
- Stockwell, R., Mansinha, L., and Lowe, R. Localization of the complex spectrum: the S transform. *IEEE Transactions on Signal Processing*, 44(4):998–1001, 4 1996.
- Strobbe, G., Carrette, E., López, J. D., Montes Restrepo, V., Van Roost, D., Meurs, A., Vonck, K., Boon, P., Vandenberghe, S., and Van Mierlo, P. Electrical source imaging of interictal spikes using multiple sparse volumetric priors for presurgical epileptogenic focus localization. *NeuroImage: Clinical*, 11:252–263, 2016.
- Stufflebeam, S. M., Tanaka, N., and Ahlfors, S. P. Clinical applications of magnetoencephalography. *Human Brain Mapping*, 30(6):1813–1823, 6 2009.



- Sun, Y. P., Wang, Y. P., Wang, Z. H., Wu, F. Y., Tang, L. O., Zhang, S. W., Pei, H. T., Wang, Y., Huang, Z. Y., Xue, Q., Xu, C. P., and Tai, J. L. High-frequency oscillations and the seizure onset zones in neocortical epilepsy. *Chinese Medical Journal*, 128(13):1724–1727, 7 2015a.
- Sun, Y.-P., Wang, Y.-P., Wang, Z.-H., Wu, F.-Y., Tang, L.-O., Zhang, S.-W., Pei, H.-T., Wang, Y., Huang, Z.-Y., Xue, Q., Xu, C.-P., and Tai, J.-L. High frequency Oscillations and the Seizure Onset Zones in Neocortical Epilepsy. *Chinese medical journal*, 128(13):1724–7, 7 2015b.
- Tadel, F., Baillet, S., Mosher, J. C., Pantazis, D., and Leahy, R. M. Brainstorm: A user-friendly application for MEG/EEG analysis. *Computational Intelligence and Neuroscience*, 2011, 2011.
- Talairach, J. and Bancaud, J. Lesion, &quot;irritative&quot; zone and epileptogenic focus. *Confinia neurologica*, 27(1):91–4, 1966.
- Talairach, J. and Bancaud, J. Stereotaxic Approach to Epilepsy. pages 297–354. Karger Publishers, 1973.
- Tamila, E., Madsen, J. R., Grant, P. E., and Pearl, P. L. Current and Emerging Potential of Magnetoencephalography in the Detection and Localization of High-Frequency Oscillations in Epilepsy. 8(January):1–28, 2017.
- Taulu, S. and Hari, R. Removal of magnetoencephalographic artifacts with temporal signal-space separation: Demonstration with single-trial auditory-evoked responses. *Human Brain Mapping*, 30(5):1524–1534, 5 2009.
- Taulu, S. and Simola, J. Spatiotemporal signal space separation method for rejecting nearby interference in MEG measurements. *Physics in medicine and biology*, 51(7):1759–68, 4 2006.
- Taulu, S., Kajola, M., and Simola, J. Suppression of interference and artifacts by the Signal Space Separation Method. *Brain topography*, 16(4):269–75, 1 2004.
- Tenney, J. R., Fujiwara, H., Horn, P. S., Vannest, J., Xiang, J., Glauser, T. A., and Rose, D. F. Low- and high-frequency oscillations reveal distinct absence seizure networks. *Annals of neurology*, 76(4):558–67, 10 2014.
- Tewarie, P., Bright, M., Hillebrand, A., Robson, S., Gascoyne, L., Morris, P., Meier, J., Van Mieghem, P., and Brookes, M. Predicting haemodynamic networks using electrophysiology: The role of non-linear and cross-frequency interactions. *NeuroImage*, 130:273–292, 4 2016.
- Tong, L., Liu, R. W., Soon, V. C., and Huang, Y. F. Indeterminacy and identifiability of blind identification. *IEEE Transactions on Circuits and Systems*, 38(5):499–509, 1991.
- Townsend, T. and Ebersole, J. Source localization of electroencephalography spikes. In Lüders, H. O., editor, *Textbook of Epilepsy Surgery*, chapter 64, page 1616. CRC Press, London, 2008.
- Uijl, S. G., Leijten, F. S. S., Parra, J., Arends, J. B. A. M., van Huffelen, A. C., and Moons, K. G. M. What is the current evidence on decision-making after referral for temporal lobe epilepsy surgery? A review of the literature. *Seizure*, 14(8):534–40, 12 2005.
- Urrestarazu, E., Chander, R., Dubeau, F., and Gotman, J. Interictal high-frequency oscillations (100–500 Hz) in the intracerebral EEG of epileptic patients. *Brain*, 130(9):2354–2366, 9 2007.

- van Klink, N., Hillebrand, A., and Zijlmans, M. Identification of epileptic high frequency oscillations in the time domain by using MEG beamformer-based virtual sensors. *Clinical Neurophysiology*, 127(1):197–208, 6 2016.
- Van Klink, N. E. C., Van’t Klooster, M. A., Zelmann, R., Leijten, F. S. S., Ferrier, C. H., Braun, K. P. J., Van Rijen, P. C., Van Putten, M. J. A. M., Huiskamp, G. J. M., and Zijlmans, M. High frequency oscillations in intra-operative electrocorticography before and after epilepsy surgery. *Clinical Neurophysiology*, 125(11):2212–2219, 2014.
- Van Veen, B. and Buckley, K. Beamforming: a versatile approach to spatial filtering. *IEEE ASSP Magazine*, 5(2):4–24, 4 1988.
- Van Veen, B., Van Drongelen, W., Yuchtman, M., and Suzuki, A. Localization of brain electrical activity via linearly constrained minimum variance spatial filtering. *IEEE Transactions on Biomedical Engineering*, 44(9):867–880, 9 1997.
- Viera, A. J. and Garrett, J. M. Understanding interobserver agreement: the kappa statistic. *Family medicine*, 37(5):360–3, 5 2005.
- von Ellenrieder, N., Andrade-Valença, L. P., Dubeau, F., and Gotman, J. Automatic detection of fast oscillations (40-200 Hz) in scalp EEG recordings. *Clinical neurophysiology : official journal of the International Federation of Clinical Neurophysiology*, 123(4):670–80, 4 2012.
- von Ellenrieder, N., Pellegrino, G., Hedrich, T., Gotman, J., Lina, J.-M., Grova, C., and Kobayashi, E. Detection and Magnetic Source Imaging of Fast Oscillations (40-160 Hz) Recorded with Magnetoencephalography in Focal Epilepsy Patients. *Brain topography*, 29(2):218–31, 3 2016.
- Vrba, J. Magnetoencephalography: the art of finding a needle in a haystack. *Physica C: Superconductivity*, 368(1-4):1–9, 3 2002.
- Wang, Z. I., Alexopoulos, A. V., Nair, D., Krishnan, B., Mosher, J. C., Burgess, R. C., and Kakisaka, Y. Feasibility of magnetoencephalography recording in an epilepsy patient with implanted responsive cortical stimulation device. *Clinical Neurophysiology*, 124(8):1705–1706, 8 2013.
- Wendel, K., Väisänen, O., Malmivuo, J., Gencer, N. G., Vanrumste, B., Durka, P., Magjarević, R., Supek, S., Pascu, M. L., Fontenelle, H., and Grave De Peralta Menendez, R. EEG/MEG source imaging: Methods, challenges, and open issues. *Computational Intelligence and Neuroscience*, 2009.
- Whitham, E. M., Pope, K. J., Fitzgibbon, S. P., Lewis, T., Clark, C. R., Loveless, S., Broberg, M., Wallace, A., DeLosAngeles, D., Lillie, P., Hardy, A., Fronsco, R., Pulbrook, A., and Willoughby, J. O. Scalp electrical recording during paralysis: Quantitative evidence that EEG frequencies above 20Hz are contaminated by EMG. *Clinical Neurophysiology*, 118(8):1877–1888, 8 2007.
- Whitham, E. M., Lewis, T., Pope, K. J., Fitzgibbon, S. P., Clark, C. R., Loveless, S., DeLosAngeles, D., Wallace, A. K., Broberg, M., and Willoughby, J. O. Thinking activates EMG in scalp electrical recordings. *Clinical neurophysiology : official journal of the International Federation of Clinical Neurophysiology*, 119(5):1166–75, 5 2008.
- Worrell, G. a., Jerbi, K., Kobayashi, K., Lina, J. M., Zelmann, R., and Le Van Quyen, M. Recording and analysis techniques for high-frequency oscillations. *Progress in neurobiology*, 98(3):265–278, 3 2012.

- Xu, C., Pham, D. L., Rettmann, M. E., Yu, D. N., and Prince, J. L. Reconstruction of the human cerebral cortex from magnetic resonance images. In *IEEE Trans Med Imaging*, volume 18, pages 467–80, 1999.
- Zelmann, R., Mari, F., Jacobs, J., Zijlmans, M., Dubeau, F., and Gotman, J. A comparison between detectors of high frequency oscillations. *Clinical neurophysiology : official journal of the International Federation of Clinical Neurophysiology*, 123(1):106–16, 1 2012.
- Zelmann, R., Lina, J. M., Schulze-Bonhage, A., Gotman, J., and Jacobs, J. Scalp EEG is not a Blur: It Can See High Frequency Oscillations Although Their Generators are Small. *Brain Topography*, 27(5):683–704, 9 2014.
- Zhang, J. and Liu, C. On Linearly Constrained Minimum Variance Beamforming. *Journal of Machine Learning Research*, 16:2099–2145, 2015.
- Zhang, Z. A fast method to compute surface potentials generated by dipoles within multilayer anisotropic spheres. *Physics in medicine and biology*, 40(3):335–49, 3 1995.
- Zifkin, B. G. and Avanzini, G. Clinical neurophysiology with special reference to the electroencephalogram. *Epilepsia*, 50(s3):30–38, 3 2009.
- Zijlmans, M. and Dubeau, F. High-frequency oscillations mirror disease activity in patients with epilepsy. (92003481):979–986, 2009.
- Zijlmans, M., Huiskamp, G. M., Leijten, F. S. S., Van Der Meij, W. M., Wieneke, G., and Van Huffelen, A. C. Modality-specific spike identification in simultaneous magnetoencephalography/electroencephalography: a methodological approach. *Journal of clinical neurophysiology : official publication of the American Electroencephalographic Society*, 19(3):183–91, 6 2002.
- Zijlmans, M., Jiruska, P., Zelmann, R., Leijten, F. S. S., Jefferys, J. G. R., and Gotman, J. High-frequency oscillations as a new biomarker in epilepsy. *Annals of neurology*, 71(2):169–78, 2 2012.